Technische Universität München
Klinikum rechts der Isar
Fakultät für Medizin
Klinik und Poliklinik für Unfallchirurgie

The assessment of bone quality in osteoporosis and a possible treatment to influence the healing capability of osteoporotic bone

Sandra Schneider

Vollständiger Abdruck der von der Fakultät für Medizin der Technischen Universität München zur Erlangung des akademischen Grades eines

Doktors der Naturwissenschaften (Dr. rer. nat.)

genehmigten Dissertation.

Vorsitzender:		Prof. Dr. Marcus R. Makowski
Prüfer der Dissertation:	1.	Priv.-Doz. Dr. Elizabeth Rosado Balmayor, Ph.D.
	2.	Prof. Dr. Franz Pfeiffer

Die Dissertation wurde am 10.8.2020 bei der Technischen Universität München eingereicht und durch die Fakultät für Medizin am 16.03.2021 angenommen.

Abstract

Patients with osteoporosis suffer from bone loss, which leads to a higher fracture risk. Occurred fractures in turn often lead to pain and to further complications. Nowadays, the standard measurement in osteoporosis diagnosis is DXA. But DXA only analyzes the bone condition locally at the site of measurement and cannot function as an overall early diagnosis tool. Because of the drawbacks of DXA and to investigate new diagnostic techniques, bone characterization within this thesis was performed by means of micro-CT, biomechanical testing and Raman spectroscopy using bone samples harvested from the femoral head of healthy and osteoporotic patients. Subsequently, miRNA levels on osteoblasts were analyzed to find a possible osteoporosis-specific expression pattern. Furthermore, correlations between the various parameters were determined for further diagnosis and prevention abilities. The healing capability of osteoporotic bone is limited and no osteoporosis-specific implants are available yet. Therefore, a silk fibroin-based scaffold was designed and used to inhibit the expression of miR-100 in seeded osteoblasts via transfection.

Zusammenfassung

Patienten mit Osteoporose haben eine geminderte Knochenmasse/-dichte, was zu einem erhöhten Frakturrisiko führt. Die auftretenden Frakturen sind schmerzhaft und können zu Komplikationen im weiteren Verlauf führen. Als Standarddiagnosemethode wird eine DXA-Messung durchgeführt, bei der allerdings nur der aktuelle Knochenzustand ermittelt und keine Vorhersage bezüglich eines eventuellen Auftretens von Osteoporose diagnostiziert werden kann. Deswegen wurde in der vorliegenden Arbeit die Knochenbeschaffenheit im Hüftkopf bei Osteoporotikern weitergehend untersucht. Hierzu wurden Tests direkt am Knochen (mikro-CT, Biomechanik), an isolierten Zellen (miRNA Expression) und auf molekularer Ebene (Raman Mikrospektroskopie) durchgeführt. Darüberhinaus wurden Korrelationen zwischen den einzelnen Methoden ermittelt, um mögliche Parameter zur Diagnose/Früherkennung von Osteoporose ausfindig zu machen. Des Weiteren erfolgt die Knochenheilung bei Osteoporotikern verlangsamt bzw. ist eingeschränkt. Deswegen wurde in einem zweiten Teil der Arbeit ein Therapieansatz basierend auf dem Tissue Engineering-Ansatz konzipiert. Bei diesem Konzept wurde ein Seidenfibroin-basiertes Scaffold entwickelt, das zur Therapie bei Knochenbrüchen eingesetzt werden kann. Zusätzlich eignet sich das Scaffold dazu, die miRNA-Expression bei Osteoblasten bei der Transfektion im 3D-Modell zu inhibieren.

Für meine Mutter...

Contents

List of Figures

List of Tables

List of Abbreviations

°C	Degree centigrade
µA	Microampere
µL	Microliter
µM	Micromolar
µm	Micrometer
AC	Attenuation coefficient
AMSC	Adipose derived mesenchymal stem cells
BD	Bone density
BMD	Bone mineral density
BMI	Body mass index
BMPR2	Bone morphogenic protein receptor type II
BMPs	Bone morphogenic proteins
BS/BV	Bone surface to bone volume ratio
BS/TV	Bone surface density
BV/TV	Relative bone volume
cDNA	Complementary desoxyribonucleinacid
CO_2	Carbon dioxide
Col1	Collagen type I
COPD	Chronic obstructive pulmonary disease
CRP	C-reactive protein
Ct.Th.	Cortical thickness
d	Day
DA	Degree of anisotropy
DMEM	Dulbecco's Modified Eagle Medium
DMSO	Dimethylsulfoxid
DVO	Dachverband der Deutschsprachigen Wissenschatichen Osteologischen Gesellschaft
DXA	Dual-energy X-ray absorptiometry
EDTA	Ethylendiamintetraacetat
ESR	Erythrocyte sedimentation rate
f	Female
F_{max}	Maximal load-to failure
$F_{max,area}$	Maximal load-to failure per area
FCS	Fetal calf serum
FD	Fractal dimension
FITC-BSA	Fluorescein isothiocyanate labeled bovine serum albumin
GGT	Gamma-glutamyltransferase
HA	Hydroxyapatite

HF	High fibroin content
HF+	High fibroin content and modified surface
hsCRP	High-sensitivity C-reactive protein concentration
kV	Kilovolt
LF	Low fibroin content
LiBr	Lithium bromide
m	Male
mg	Milligram
micro-CT	Micro-computed tomography
min	Minute
miRNA	Micro ribonucleic acid
mL	Milliliter
MMI	Polar moment of interia
mRNA	Messenger-RNA
MTT	3-(4,5-dimethylthiazol-2-yl)-2,5-diphenyltetrazolium bromide
N	Newton
ncRNA	Non-coding RNA
ng	Nanogram
nM	Nanomolar
nm	Nanometer
nt	Nucleotides
PBS	Phosphate-buffered saline
PC-1	Principal component 1
PCA	Principal component analysis
PCR	Polymerase chain reaction
pre-miRNA	miRNA precursor
rcf	Relative centrifugal force
RISC	RNA-induced silencing complex
ROI	Region of interest
RT	Room temperature
SDS	Sodium dodecyl sulfate
SEM	Scanning electron microscope
SMI	Structure model index
T+	Transfected with miR-100-5p inhibitor
T2D	Untransfected in 2D
T3D	Untransfected in 3D
Tb.N.	Trabecular number
Tb.Sp.	Trabecular separation
Tb.Th.	Trabecular thickness
TSH	Thyroidea stimulating hormone
VOI	Volume of interest
WHO	World Health Organization

1. Introduction

Bone is modeled and remodeled by three types of cells - osteoblasts, osteoclasts and osteocytes [88]. Osteoblasts are bone modeling cells. Osteocytes are also osteoblasts, but they are incorporated into the matrix. Osteocytes regulate osteoblasts and osteoclasts. Mineral bone is degraded by osteoclasts. An overactivity and formation of osteoclasts leads to pathogenic bone loss as in osteoporosis, rheumatoid arthritis and loosening of joint prostheses may appear [88]. The characterization and possible treatment of osteoporosis will be analyzed in this thesis.

Skeletal function is depending on bone behavior, which includes bone density and bone quality [41]. Due to osteoporosis, the skeleton suffers from bone loss, which leads to a higher risk of fractures. Those fractures lead to pain, deformity and sometimes more complications and can even lead to death [111]. As women have a lower bone mass then men, and as bone geometry and composition naturally changes with age, such changes are more severe for older women [158]. Diseases, which have an impact on bone mass/loss, generally have a faster influence on women than on men [158]. Low bone mass is classified as a diagnostic stadium of osteoporosis and also referred to as osteopenia [178]. Studies about the impact of bone loss on mechanical strength have been conducted quite often [96, 106, 180]. Causes for bone loss have been researched and discussed by various scholars [40, 111, 134, 144]. However, bone behavior is determined by bone mass and bone quality. Bone mass is characterized by bone mineral density (BMD), which is dependent on the concentration of hydroxyapatite, the main component in the bone matrix. Bone quality includes morphology, architecture and composition. Trabecular bone density is among the factors that predict the fracture risk or the pathophysiology of osteoporosis [98]. Because of this, a panel of different methods on the different levels of tissue and cells needs to be established to characterize the progress of osteoporosis.

The aims of this thesis were to assess the bone quality in osteoporosis and test a possible drug delivery system for treatment. In the first part, the better understanding of tissue changes impacted by osteoporosis compared to healthy bone is of interest. Furthermore, possible correlations between the bone parameters obtained by different techniques are investigated. The second part focuses on the development of possible drug delivery systems in 3D for treating osteoporosis-induced fractures. In Chapter 2.1 - 2.3, an overview of osteoporosis definition, clinical diagnostics and common prophylaxis and treatment methods will be provided. Furthermore, current research applications and principles of micro-CT, Raman spectroscopy and biomechanical testing will be given in Chapter 2.4. Additionally, the subsequent tissue engineering approach and microRNA will be explained in Chapter 2.5. Afterwards, the applied methods will be described in detail in Chapter 3. Finally, the results will be presented and discussed in Chapter 4 and Chapter 5, respectively.

Some of the performed methods were established in cooperation with the BIOtech - Center for Biomedical Technologies, Department of Industrial Engineering at the University of Trento,

(scaffold production, Italy), the Schenke-Layland Laboratory (Raman microspectroscopy, Research Institute for Women's Health, Department of Women's Health at Eberhard Karls University Tübingen, Germany) and the biomechanical lab of the department of orthopedics and sports orthopedics at Klinikum rechts der Isar der TUM (biomechanical testing, Germany).

2. Theoretical Background

Considering the challenging goal of this thesis, the latest state of the art regarding osteoporosis diagnosis and treatment are reported in this chapter in great detail (Section 2.1, 2.2 and 2.3). Moreover, background information about the various methods used in this thesis are given in the following chapter for a better understanding and interpretation of the presented results. Application methods and functional principles of micro-CT, Raman spectroscopy and biomechanical testing are explained in Section 2.4. Furthermore, in Section 2.5, a consideration of biomarkers and also biomaterial is provided.

2.1. Osteoporosis

The general definition of osteoporosis is based on a guideline published by the World Health Organization (WHO) [181]. In this guideline, the authors used two different definitions. The first one is adapted from Bonjour et al., where enhanced bone fragilty and increased fracture risk is explained due to a low bone mass and microarchitectural deterioration of the bone tissue, which classify osteoporosis [14]. The second definition is the more commonly used one, where additionally "an estimate of bone mineral density [therefore] provides an effective assessment of fracture risk" and hence of osteoporosis, as noted in [181]. The bone mineral density (BMD) is measured by dual-energy X-ray absorptiometry (DXA) as gold standard, and expressed as T-score. The BMD in young adult women is normally distributed and unaffected by the measuring method. A pool of BMD values of this group are an ideal reference for the standard deviation units method. This method circumvents any difference in calibration between several instruments. The deviation of an individual BMD value to a reference pool of BMD values determined by this method is referred to as T-score. The WHO defines four different diagnostic stadiums of osteoporosis for Caucasian women [178, 181]:

1. Normal: T-score ≥ -1.0
2. Osteopenia (low bone mass): $-1.0 >$ T-score > -2.5
3. Osteoporosis: T-score ≤ -2.5
4. Severe (established) osteoporosis: T-score ≤ -2.5 in presence of one or more fractures

Osteoporosis appears three times more often in women than in men [178]. Reasons for this could be the lower bone mass in women and the estrogen change during the menopause. Additionally, women live longer than men and because of that, the bone mass reduction is greater over the whole lifespan [178].

Besides the WHO guideline, there are also country-specific guidelines and recommendations available [43, 64]. However, all of them use the osteoporosis definition of the WHO guideline.

2.2. Current clinical diagnostics of osteoporosis

All following descriptions in this section are taken from the German society of osteology (German: Dachverband der Deutschsprachigen Wissenschafltichen Osteologischen Gesellschaft e.V. (DVO)) guideline, the gold standard in German osteoporosis diagnostics [43].

2.2.1. Fracture risk factors

The main clinical problem of osteoporosis is not the decreasing bone mass, but the consequently higher fracture risk and the impact of fracture itself. Because of this, most recommendations are for patients with a higher risk for osteoporosis and fracture. A higher risk for osteoporotic fractures depends on several general factors, specific primary diseases and drug therapies (Tab. 2.1).

Table 2.1.: Overview of osteoporotic risk fracture factors adapted from [43]

general risks	**special diseases**	**medicinal therapy**
Age	Endocrinological	Hormonal ablative therapy
Sex	Rheumatological	Aromatase inhibitor
Vertebral body fractures	Gastroenterologic	Glucocorticoid
Non-vertebral fractures	Neurological	Glitazone
Fractures of the parents	Cardiac degeneration	Sedatives
Multiple intrinsic falls	Monoclonal gammopathy	Loop diuretics
Immobility	Alcoholic liver diseases	Neuroleptic agents
Grip intensity		Antidepressants
Smoking and COPD		Opioids
Drop in weight		Proton pump inhibitor
Vitamin D- and calcium-lack		Orthostasis-inducing agents
Lack of homocysteine, folic acid and vitamin B12		Contraceptive agents
C-reactive protein		
Hyponatremia		
Cadmium		

The single factors of the table shown above are explained in the following (Tab. 2.1). Increasing age is one of the main fracture risk factors - independent of sex and bone density. Sex itself is a risk factor, but inconsistent. It looks like the fracture risk for women is higher than for men [43, 181]. In Germany, the risk value for men and women at an age of roughly 60 is almost the same, but with increasing age, the fracture risk for women also increased [67]. However, it depends if the bone density is adjusted to a control value and which control values are used for the determination of the T-score (e. g. sex-specific or only from women) [43]. Multiple vertebral body fractures without trauma increase the risk of osteoporotic fractures [43]. Furthermore, non-vertebral fractures after the age of 50 increase the fracture risk independent of bone density and age [7, 15, 23, 27, 33–35, 37, 44, 69, 74, 85, 124, 125, 138, 140, 152, 162, 163, 167]. The occurrence of a proximal femur fracture in the medical history

of a patient's parents is an independent risk factor from bone density, age and for all fractures, but should be considered as a possible genetic risk [43]. Multiple intrinsic falls are not clearly related to a higher osteoporotic fracture risk [8, 43, 126]. Immobility is a general risk factor for fractures [43]. A diminished grip intensity is also a fracture risk factor, but has not been well-clarified [1, 31, 87]. Moreover, smoking and chronic obstructive pulmonary disease (COPD) are currently not well-investigated risk factors [43]. The relative risk of a fracture in underweight women and men is approximately two times the value for a normal weight person [43]. With dropping weight, the fracture risk is also higher for people, who started weight loss with a BMI larger then 25.9, than for people, who started loosing weight with a BMI below 25.9. A higher fracture risk has been associated with Anorexia nervosa and also leads to a higher risk of osteoporosis [160]. A lack of vitamin D and calcium is a reversible risk factor, in which the study situation is not consistent, and should not be considered as calculation factor for the fracture risk [43]. The study situation is neither clearly defined for a higher homocysteine concentration, folic acid lack and vitamin B12 lack insofar that there is by now no recommendation for a measurement of these factors [43]. Looking at the high-sensitivity C-reactive protein concentration (hsCRP), hyponatremia or cadmium uptake, there has no sufficient number of studies been performed to derive recommendations, even if the few published results show a risk factor [30, 43, 66, 83]. But the interactions with other substances or diseases are not well-investigated.

The risk of osteoporotic fractures also increases with specific primary diseases. In the DVO guideline, several possible relevant endocrinological diseases are listed, such as Cushing syndrome, subclinical hypercortisolism, primary hyperparathyreoidism, hypopituitarism, hypogonadism, diabetes mellitus type I and II [43]. Both diabetes mellitus types are associated with an increased risk for fracture independent of sex, whereby type I has a higher risk for fractures [43]. Nevertheless, it is considered in some fracture prognosis models. For other diseases, the fracture risk is sometimes slightly increased, but mostly independent from bone density and highly treatable. Therefore, these diseases should only be considered, if they are not treated as additive risk factor. As rheumatological diseases, rheumatoid arthritis, ankylosing spondylitis and systemic lupus erythematosus are listed in the DVO guideline [43]. Rheumatoid arthritis is independent from bone density, glucocorticoid therapy and other risk factors, but as the disease is often associated with glucocorticoid therapy, there is a recommendation for patients with this disease and the indication for basic diagnostics [43]. Ankylosing spondylitis is a risk factor for vertebral fractures [43]. Systemic lupus erythematosus is accompanied by a moderate hip fracture risk and osteoporotic fracture risk, too [43]. Gastroenterologic diseases, such as celiac disease, chronic inflammatory bowel disease and B-II-gastric resection or gastrectomy, have no influence on the fracture risk [43]. Looking at neurological diseases, some of them have no direct influence or are not correlated to bone density, e.g. epilepsy or schizophrenia [43, 164]. A study of Alzheimer disease show a two times higher risk for fractures [93]. Older people and women have a higher fracture risk, if they have an apoplectic insult [185]. Considering Morbus Parkinson, the risk for fractures and osteoporosis is increased [168, 179]. Half of all fractures are hip fractures, because of the higher risk of falling [179]. Looking at other diseases, such as cardiac degeneration and alcoholic liver disease, there is no influence on the fracture risk and they should only be considered as additional factors [43]. Monoclonal gammopathy has an increasing risk for all fractures and particularly for vertebral fractures [43]. Moreover, 15 % of those patients have osteoporosis [55].

Furthermore, there are also drug therapies, which influence the fracture risk or the risk for

osteoporosis. During the intake of glucocorticoids, the fracture risk is higher depending on the dose and the duration [43]. Sedatives, orthostasis-inducing agents and neuroleptic agents are all drugs that increase the fracture risk for both sexes [43, 89]. Contraceptive agents, loop diuretics and proton pump inhibitors have no relevance for any fracture risk or osteoporosis [43]. Hormonal-ablative therapy shows an independent increased risk after adjustment of bone mineral density [43]. Aromatase inhibitor and glitazone show a slightly increased risk, but its mostly independent of osteoporosis or from other risk factors [43]. According to the DVO guideline, there is no sufficient number of studies for a valid recommendation [43]. Considering the influence of antidepressants, the risk is still significantly increased after adjustment of bone mineral density [143, 182]. Opioids lead to an increased risk for all fractures because of the cognitive impairment induced by their intake [43].

2.2.2. Basic diagnostics recommended by the DVO

In general, the indication for basic diagnostics is given once the fracture risk increases 20 % in ten years [43]. Additionally, a fracture risk assessment should be conducted if a fragility fracture arises before the age of 50. [43]. The fracture assessment depends on the age, sex and the fracture risk factors mentioned in Section 2.2.1. Only non-traumatic fractures should be considered. For the risk factor calculation, only the specific factor, which has the highest impact, is of interest. However, not more than two factors should be considered for the calculation. The main indication factor is the DXA value [43].

Basic diagnostics include anamnesis, clinical findings, bone mineral density measurement via DXA, basic laboratory parameters and in case of clinical indication, imaging methods for detecting osteoporotic vertebral body fractures [43]. Aim of basic diagnostics is to evaluate the risk for fractures in general and the current medical condition. The aim of the anamnesis is to clarify the diagnosis of osteoporosis - and fracture risk with the inclusion of already occurred vertebral body fractures. After that, the mobility of the whole body, especially of the spine, the body statics and the body height will be checked in the clinical findings [43]. Additionally, neurological tests should be performed to clarify an increased risk of falling. Through osteodensitometry via DXA, the T-score (Chap. 2.1), which is the main criterion for osteoporosis, is determinable. Decreasing bone mineral density is detectable and is used for assessing the fracture risk. The mean T-score of the lumbar spine (of the lumbar vertebrae 1 to 4) or the T-score of the proximal femur or femoral neck are used for classification. Spondylophytes, significant vascular sclerosis, vertebral fractures or degenerative changes ($>$ 2 Kellgren-Lawrence-Score) compromise the measurement. The Kellgren-Lawrence-Score describes five grades (Grade 0 to 4) of degenerative changes in osteoarthrosis based on X-rays [79].

The basic laboratory parameters provide chemical indicators for risk factors and for secondary osteoporosis [43]. Those parameters - as differential diagnostics - exclude other diseases such as osteopathy or osteomalacia. The basic laboratory parameters are serum-calcium, serum-phosphat, alkaline phosphatase, gamma-glutamyltransferase (GGT), creatinine clearance, erythrocyte sedimentation rate (ESR)/C-reactive protein (CRP), hemogram, thyroidea stimulating hormone (TSH) [43]. Serum-sodium, serum protein electrophoresis, testosterone, bone resorption parameter and 25-hydroxycholecalciferol are optional parameters, whose detection depends on the individual case [43].

2.3. DVO guidelines for osteoporosis prophylaxis and clinical treatment

2.3.1. Prophylaxis recommendations

The osteoporosis prophylaxis results in an improvement of bone stability and/or a reduction of fractures [43]. The following mentioned recommendations are taken from the DVO guideline [43]. Muscle power, coordination and equilibrium should be trained by reducing immobilization. Patients over 80 years of age should have a fall anamnesis every year. Underweight and adiposity should be avoided. Calcium and vitamin D should be taken in adequate amounts per day (1000 mg and 800 mg, respectively). A supplementation should only be considered, if the recommended amount cannot be reached by means of the patient's normal diet. Drugs, which increase the risk for falling and/or osteoporosis, should be checked regularly regarding their benefit and risk for the patient. Older patients, who live in institutional care, should have the possibility to use a hip protector to reduce fractures near the hip.

2.3.2. Therapies and limitations

The current clinical therapy for primary osteoporosis is based on drugs recommended in the DVO guideline [43]. Indications for this therapy are low-traumatic vertebral body fractures with T-score < -2, low-traumatic proximal femur fractures with T-score < -2 or high-dose oral glucocorticoid over three months and T-score < -1.5 or the occurrence of multiple low-traumatic fractures [43]. However, the fracture risk in ten years is required to be above 30 % for a drug-treated therapy. For the diagnostic part, the risk in ten years must not exceed 20 %. Besides that, vertebral body fractures and femur fractures are more typical for osteoporosis than "major fractures" [43].

Alendronate, bazedoxifene, denosumab, ibandronate, estrogen, teriparatide, raloxifene, risedronate and zoledronate are all recommended drugs for postmenopausal women [43]. Those drugs have all a proven fracture reduction over 3-5 years [43]. Estrogen is only approved, if there is no possibility for the use of the before-mentioned drugs because of contraindications or intolerance [43]. The DVO recommendation for drugs with high therapeutic efficiency for all types of fractures (vertebral body fracture, proximal femur fractures and peripheral fractures) is applicable for alendronate, denosumab, estrogen, risedronate and zoledronate. For proximal femur fractures, only alendronate, denosumab, risedronate, zoledronate and estrogen are showing a therapeutic efficiency [43]. For men, the approved drugs are alendronate, risedronate, zoledronate, denosumab and teriparatide [28, 43, 49, 76]. The efficiency of those drugs is lower than for women according to the DVO evaluation [43, 153]. For secondary osteoporosis induced by glucocorticoids, alendronate, risedronate, zoledronate and teriparatide are approved for women [43]. For men, only alendronate, teriparatide and zoledronate are approved for treating secondary osteoporosis [43].

Zolendronate should be administered two weeks after the femoral fracture [43, 97]. Atypical femur fractures occur under the treatment with bisphosphonates and denosumab [43]. Auricular fibrillation can be related to bisphosphonates therapy [43]. Denosumab and bisphosphonates can lead to a heavy hypocalcemia in rare cases [43]. Raloxifen and bazedoxifene

show an increased risk for venous thromboembolism [43]. Raloxifene can decrease the risk for breast carcinoma [43].

A reevaluation of the osteoporosis therapy should be performed after three to five years and the risk versus benefit should be recalculated. Teriparatide should not be taken for periods longer than two years [43]. A proven benefit is shown for denosumab if used for three years, for raloxifen for eight years and for bisphosphonates if used for three to five years [43].

2.4. Recent research: Advanced novel diagnostics ex vivo

When analyzing the current research for osteoporosis, it is obvious that the number of non-treated osteoporotic patients is limited. Obtaining human bone tissue for testing the gene expression or doing biomechanical testing *ex vivo* is even more limited. Even statistically analyzing sex dependence or independence is difficult. In the following chapter, established methods such as micro-CT or biomechanical testing will be presented. Also, new approaches such as Raman spectroscopy will be discussed. This technique may lead to meaningful findings by using very small bone specimens. The main focus will thereby be on bone research applications.

2.4.1. Micro-computed tomography (micro-CT)

The main components of micro-computed tomography (micro-CT) machines are a X-ray source, a detector and a sample holder (Fig. 2.1). In *ex vivo* micro-CTs, the sample rotates and the X-ray source and detector remain stationary. In clinical CTs and also in micro-CTs for *in vivo* scanning, the opposite occurs. The patient or sample remains stationary and the X-ray source and detector are moving. The generated pictures are projection images, which are taken in prescribed angle steps up to 360 °. In a second step, those projection images are reconstructed by a Feldkamp algorithm (example for Bruker scanner) to construct a final 3D image dataset, which is used for analysis. CTs nowadays have resolutions in low nanometer levels, which are used in material science and *ex vivo* scans [115]. For *in vivo* scans, resolutions of approximately 20 µm and higher are used because of a faster scanning time, thus resulting in low radiation. The resolution is the only difference between clinical CTs and micro-CTs, the underlying principles are the same [113].

The major benefit of the technique is that it is a non-destructive method, which can be performed *in vivo*, *ex vivo* and with non animal-/human-like materials. The only restriction is that soft tissues, e.g., muscle, blood vessels, lung, heart etc., which are non-mineralized and cannot be detected [113]. Within the BMD measurement, only mineralized matrix is measured and no bone marrow between the trabecula. As for osteoporosis, only the bone structural behavior is of interest, thus this is not a disadvantage.

Because of the low inherent X-ray contrast of soft tissue, a staining is required for CT visualization [113, 135]. There are more and more studies available for possible contrast agents [113, 135, 161]. The most cost-effective and easiest-to-handle staining reagent is Lugol's solution or iodine solution, respectively [65]. Pauwels et al. tested 28 contrast agents on bacon stripes, whereof 26 contrast agents showed an improvement of the contrast between muscle

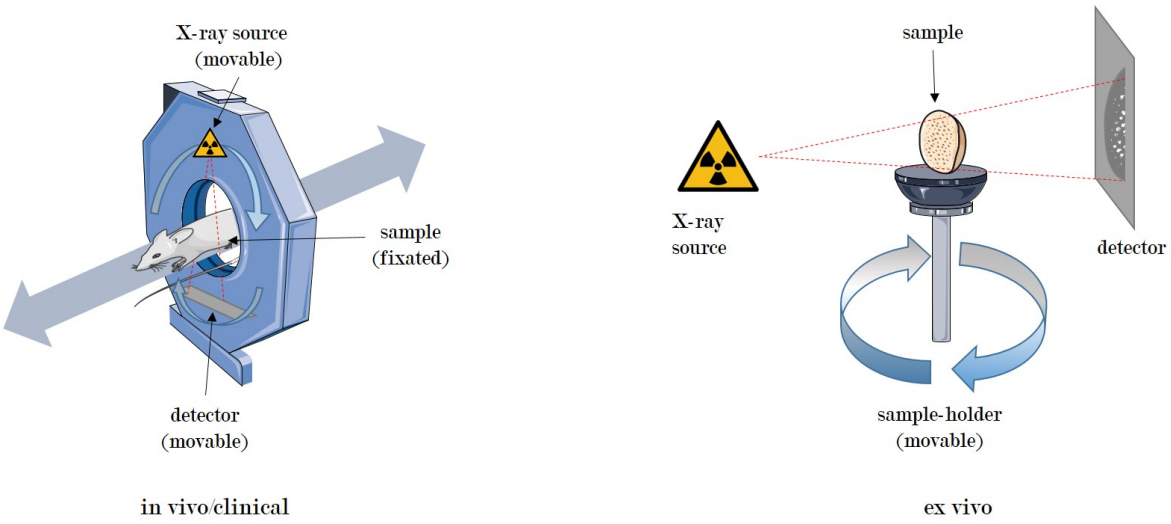

Figure 2.1.: Principle setup of a clinical/*in vivo* CT (left side) and an *ex vivo* CT (right side). Modified from Servier Medical Art by Servier (https://smart.servier.com). Servier Medical Art by Servier is made available under the terms of the Creative Commons Attribution 3.0 license France.

and adipose tissue [135]. The fixation of the sample and also the incubation in the reagent have an influence on the staining result. Therefore, previous optimization steps are necessary to obtain the optimal result [65, 113, 161]. Jeffrey et al. show that the specimen size, time in contrast agent solution and the concentration of iodine solution have an impact on the contrast between muscle and connective tissue [70].

Bone research is the main application for micro-CT, including investigations on bone growth and also bone diseases. The reconstructed 3D image dataset enables the determination of bone density and morphometry. In this thesis, the bone density always indicates the bone mineral density (BMD), which is the amount of hydroxyapatite in the sample volume. This leads to the possibility of using BMD as grouping factor for osteoporotic and healthy bone. Bone morphometry is analyzed by relative bone volume (BV/TV), trabecular/cortical thickness (Tb.Th./Ct.Th.), trabecular separation and number (Tb.Sp.,Tb.N.) and surface to volume ratio (BS/BV), which can be computed from the 3D reconstruction [24, 36, 59, 148]. BV/TV describes the proportion of the analyzed volume of interest (VOI) occupied by trabecula. Trabecular separation is the thickness of the space within the VOI. Trabecular number implies the number of traversals across a trabecular structure on a linear random path through the VOI. BS/BV characterizes the complexity of a structure and is the ratio of solid surface to volume measured in the VOI. Moreover, the degree of anisotropy (DA), the Euler number, the fractal dimension and the structure model index (SMI) are of interest in bone research [24, 26, 36, 59, 72, 99]. In case of bone, the DA describes the orientation of the trabeculae. The Euler number is an indicator of connectivity density, while fractal dimension is an indicator of surface complexity. SMI represents the relative prevalence of rods and plates in a VOI. The degradation of trabecular bone in osteoporosis can be characterized by a transition from plate-like to rod-like architecture. The bone morphometry parameters can lead to more information of osteoporotic bone. Sun and coworkers showed that micro-CT measurements are highly

sensitive, but show no significant differences of trabecular bone parameters *in vivo* compared to *ex vivo* [165]. Besides that, van Schaik et al. used CT scans for detecting lesion burden in skeletons [151]. Panzer et al. used the technique for the evaluation of soft tissue in mummies [132].

2.4.2. Raman spectroscopy

Raman spectroscopy is a non-invasive, label-free method for detecting biochemical fingerprints (organic and mineral phase) in 2D materials, tissues and living cells *in situ* and *in vivo* [25, 71, 142]. The technique can be used with fresh, fixed and embedded samples [101]. The Raman spectrum shows single chemical elements and chemical combinations. Looking at the bone matrix, collagen and hydroxyapatite are significant components [25]. The Raman spectrum of bone provides information on bone mineral crystallinity, orientation of mineral crystallinities, collagen fibril axis, carbonate-to-phosphate ratio and mineral-to-matrix ratio [57, 101, 118].

Raman spectroscopy is by now a key word for over 25 different techniques. Examples are spontaneous Raman, Fourier transform Raman scattering, stimulated Raman scattering and surface-enhanced Raman scattering [71]. The general principle of Raman spectroscopy is that - due to a (monochromatic) light beam - photons excite the molecules, which respond by emission of specific frequencies [25, 71]. Those frequencies depend on masses of atoms and on the strength of molecular bonds [25]. Each bond has a specific frequency, which additionally depends on the position of the atom in the molecule [25]. The vibrational frequency is equal to the energy shift between the peaks [25]. The band form is the fingerprint of the specific molecule [25]. The light beam is often generated by a laser at $\lambda = 785\,\mathrm{nm}$, because the output of Raman signal intensity, fluorescence and cost is more balanced, but visible lasers are used more and more [71]. A typical Raman spectrometer setup is shown in Figure 2.2. A laser beam is guided through a notch filter and a beam splitter into the objective and focused on the sample. The scattered light will be collected by a lens and only light with a Raman shift passes the notch filter and the spectrum is detected by a spectrometer.

Raman spectroscopy is used in various applications. For instance for detecting the osteogenic differentiation of jaw periosteal cells and the resulting mineral matrix [16]. This technique also has the capability for *in situ* quality control as shown in the study of Pudlas et al. [142]. In the study, they showed that a phenotype separation of cells is possible for living primary and immortalized keratinocytes [142]. Benign and malignant breast cancer lesions were also identified by Raman spectroscopy [60]. Furthermore, *in vivo* glucose detection was performed with Raman spectroscopy in rats [110]. Raman spectroscopy was also used for *in vitro* diagnosis of staphylococcal osteomyelitis by the group of Khalid et al. [80]. Raman spectroscopy offers the possibility to determine the single components and molecular deformations of bone and can show differences between healthy tissue and non-healthy tissue on molecular level [60]. Because of this, it could show molecular level differences between osteoporotic tissue and healthy tissue.

2.4.3. Biomechanical testing

Biomechanics mainly tries to analyze the stress and strain relation for materials (organic and/or anorganic). In this case, stress relates to the force per unit area inside of an object

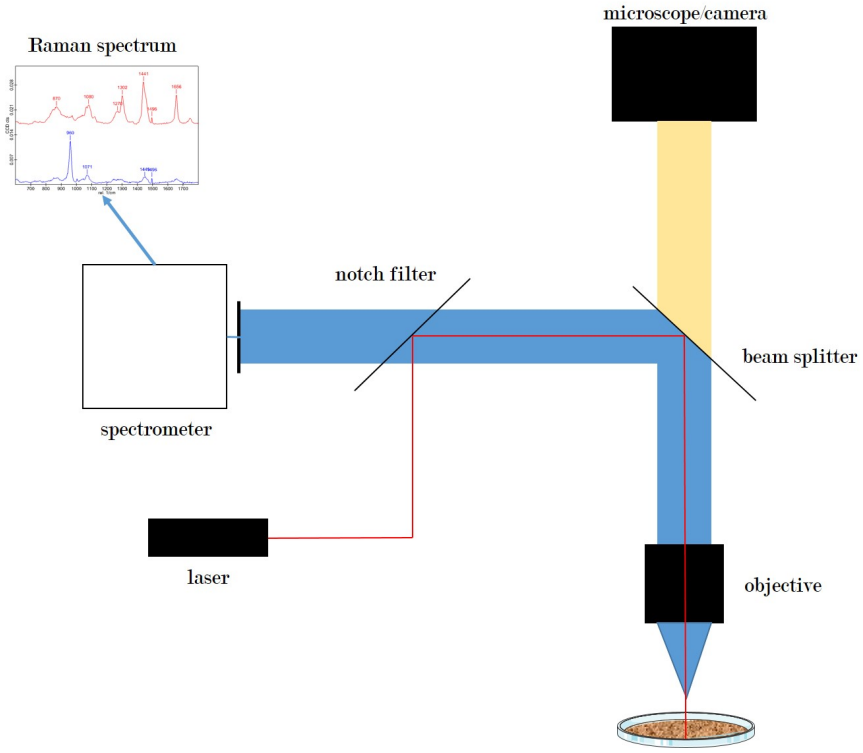

Figure 2.2.: Setup of a Raman spectrometer showing its main components. The laser beam (red) is guided through a notch filter and a beam splitter into the objective and focused on the sample. Because of molecular interactions, the light is scattered, collected by the lens and only light with a Raman shift (wavelength shift, blue) passes the notch filter and is directed into the spectrometer. The beam path of the bright-field of the microscope is shown through the yellow area. Modified from Marzi et al. [108]. Permission request see Figure A.3.

and can be separated into compressive, tensile or shear stress [170]. All three types constantly appear in combination [170]. The relative deformation or percentage change in length is called strain [170], while the Poisson's ratio is defined as the ratio of strain along the width to that along the length [170]. In turn, the relation between stress and strain is given in the stress-strain curve. The curve can be divided into two parts - the elastic and the plastic strain region [170]. In between the two regions, the yield point can be found. Above this point, stress leads to permanent damage (permanent deformation) [170]. The exact position of the yield point is not well-defined [170]. The endpoint of the curve is the point where fractures occur [170]. Within the stress-strain curve, the energy absorption or toughness is quantifiable through the area below the curve of both regions [170]. It corresponds to the energy, which can be absorbed, until a fracture occurs [170]. The higher the value in a bone, the higher the energy, which can be absorbed in case of a fall. The Young's modulus or elastic modulus is the slope of the stress-strain curve of the elastic region and varies with direction and location [170]. As an example, Youngs's modulus of a trabecular bone can vary because of the bone density and trabecular orientation from 0.1 GPa to 4.5 GPa [170]. If a material has different properties in the three different directions, like bone, it is called anisotropic [170]. Especially in the femur head, the orientation of trabeculae at the main load axis is anisotropic. If all properties vary in

the three perpendicular directions, then it is referred to as orthotropic [170]. If the properties of two directions are the same, it is called transversely isotropic [170]. An isotropic material has the same properties in all directions [170]. The Young's modulus expresses the (intrinsic) stiffness of a material [170]. The stiffness of trabecular bone can be divided into two different values - material and structural stiffness. Material stiffness is the stiffness of each trabecula and structural stiffness is the stiffness of the trabecular structure [170].

Examples of the main biomechanical testing methods are tensile test, bending test, compressive test, torsion test and pure shear test [170] (Fig. 2.3). For tensile testing, the sample needs to be fixated on two blocks, which will be pulled in opposite directions (Fig. 2.3 E). One limitation of the method is that a trabecular sample needs to have a width of at least 4 mm to 8 mm and also has to be relatively large in length (e.g., 15 mm to 20 mm) [170]. In contrast, small bones can be used for bending tests, but only if their length is more than 16 times their thickness [170]. The bone will be bent until failure [170] (Fig. 2.3 A). Failure usually occurs on the tensile side [170]. Measurable values during this test are Young's modulus, stress and strain [170]. Compressive testing is more often used with trabecular bone [170] (Fig. 2.3 B). The sample needs to be as large as for the tensile test [170]. The sample areas, which are in contact with the loading plates, need to be planar. Otherwise, end effects will appear with underestimated strength and Young's modulus values [170]. Nevertheless, this method simulates the *in vivo* conditions of bones more closely [170]. The shear force can be measured with a torsion test [170] (Fig. 2.3 C). The ends of the samples are embedded in blocks and then twisted [170]. With the resulting torque-twist curve, the shear modulus of elasticity can be calculated [170]. Also the polar moment of inertia can be determined [170]. Torsion testing creates shear and tensile stress, because of which it is only used as general parameter for bone strength [170] (Fig. 2.3 D). Pure shear verification is very difficult [170]. There are two methods, Iosipescu and Arcan test, which can be conducted with small samples, but the size and the position of the sample needs to be very accurate [170]. A fatigue test can be performed with all kinds of loading types mentioned before (except pure shear force) [170]. For this, a machine needs to apply cyclic loading until failure of the sample occurs [170]. A failure is a decrease of 30 % in the slope of the stress-strain curve (stiffness) [170]. Besides the mechanical test, ultrasonic tests or acoustic microscopy can also be used for measuring Young's modulus [5, 170]. As the risk of fractures increases in osteoporosis, the force at maximal load before failure (F_{max}) is an important parameter.

The main biomedical applications of biomechanical testing are characterizations of tissues and their behavior. With their result in mind, replacement materials, such as scaffolds and implants, are tested and their behavior is compared to the behavior of the original tissue. Several studies characterized bone of various regions within one bone area [38, 78, 90] or different bone areas [106, 166]. As bone consists of two phases, a cortical and a trabecular phase, biomechanical testing is also performed - particularly within those phases [21, 38, 75, 78, 96, 106]. Furthermore, biomechanical testing is also performed on bovine and murine bones for establishing animal models and understanding the bone behavior better [20, 32, 150]. Moreover, testing of bone with skeletal disorders is performed with human bone [90, 96, 166] and even murine bone [32]. Chon et al. measured the elastic modulus of a mouse femur via femoral head compression test [32]. Furthermore, compression testing is performed for generating experimental values for setting up models for simulations of fractures [61].

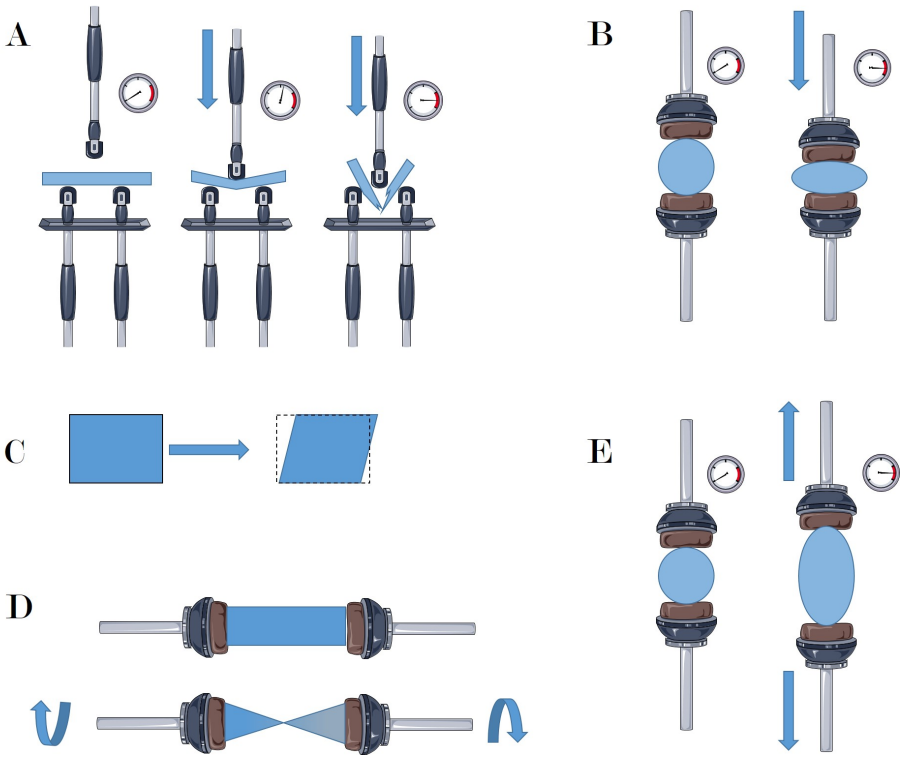

Figure 2.3.: Principle of biomechanical testing methods. A: bending test; B: compression test; C: shear test; D: torsion test; E: tensile test. Modified from Servier Medical Art by Servier (https://smart.servier.com). Servier Medical Art by Servier is made available under the terms of the Creative Commons Attribution 3.0 license France.

2.5. Novel therapeutic possibilities: scaffolds and miRNA

Novel therapeutic attempts are on the one hand based on manipulation of a signal path to inhibit or prevent the disease and, on the other hand, if the disease appears, on the reduction of any further complications. In the case of osteoporosis, drugs are administered to inhibit the further progression of the structural bone changes. The regenerative capacity of bone is consequently compromised [136]. If a fracture appears, an adapted disease-specific implant is currently not available. There is a huge need for disease-specific implants, as most implants are designed for healthy patients without comorbidities. Failure of internal fixation at the femoral neck and intertrochanteric region are caused by a failure of the properties of trabecular bone, which is a limiting factor for the strength of the internal fixation [106]. Implants in patients with low bone density, as in osteoporotic patients, show a considerably decreased performance in the regeneration of bone tissue compared to patients with normal bone density [180]. Besides implants, autografts are often used for repairing bone defects [4]. For autografts, bone tissue from the patient is necessary and needs to be collected from a suitable location, for example at the iliac crest. A suitable location is a region where enough healthy bone material can be harvested for treating the defect [4]. This procedure is painful for the patient, as two surgeries are necessary (one for collecting the bone material and the second one for treating the initial defect) [4, 19].

The regeneration ability of bone is influenced by the defect size and/or by the disease or trauma itself, respectively. Besides implants, another promising option is bone tissue engineering [176]. It is based on the combination of cells, bioactive factors and scaffolds. Scaffolds are used for cell migration, differentiation and proliferation [4] (Fig. 2.4). It can also be a combination of only two factors, where only scaffolds and bioactive factors are used, because the addition of tissue-specific cells is sometimes not feasible or the addition of stem cells not always required. In any case, the concept of tissue engineering is utilized to support the bone's own repair mechanisms [4]. A 3D scaffold should be a supportive material, which can imitate bone structure and supports the cell attachment and growth. While designing scaffolds, the influence of structural parameters should be taken into account, as they influence the nutrient diffusion and cell-cell interaction [128]. Materials used for scaffold fabrication can be metals and their alloys, e.g. titanium, cobalt-chromium and stainless steel [121]. Also synthetic polymers, bioactive glasses and ceramics can be used as materials for this purpose [19, 116, 121, 139]. Additionally, natural polymers can also be used, e.g. collagen, silk fibroin, chitosan [53, 73, 133, 141]. The advantages of using natural polymers compared to synthetic materials are a reduced foreign body reaction, lower infection rates and no degradation byproducts, which are exogenous substances, [157].

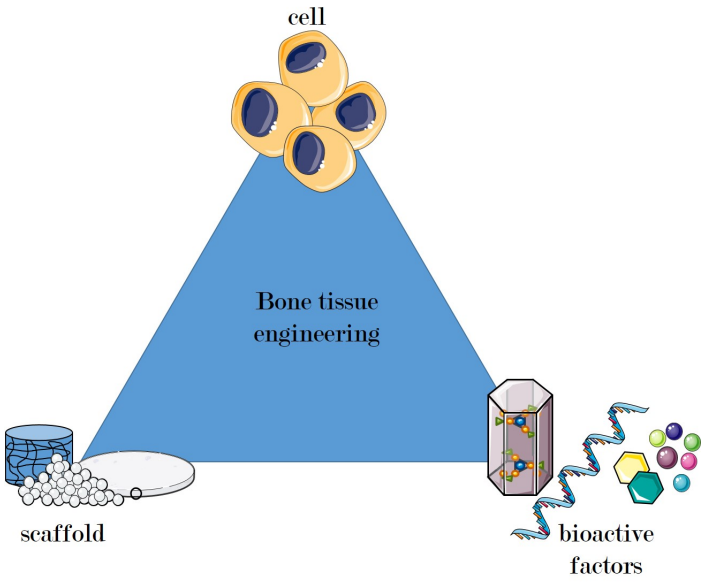

Figure 2.4.: Bone tissue engineering approach. Modified from Servier Medical Art by Servier (https://smart.servier.com). Servier Medical Art by Servier is made available under the terms of the Creative Commons Attribution 3.0 license France.

As a promising biomaterial for tissue engineering, silk fibroin is frequently used [117, 147, 184]. Because of the high flexibility of the material in production, the scaffold can have different mechanical and biological properties, structure, molecular weight and amino-acid composition [120]. Furthermore, biomechanical properties and degradation rates can vary depending on the production method [147]. Silk fibroin can easily be chemically modified [13, 82, 147] and can incorporate growth factors [52, 147]. Silk fibroin can be extracted from spiderweb or from silkworm cocoons [2]. Spider silk is not often used, because insufficient silk amounts [2]. Silk fibroin can be proceeded into many various scaffold shapes [147, 174], such as sponges

[51, 105, 123, 174], fibers [81, 174], films [104, 156, 174, 183], hydrogels [45, 50], particles and tubes [147]. Changing the chemistry or the process of preparation itself can cause a different bioactivity [120]. Silk fibroin-based scaffolds can support the differentiation of stem cells into muscle cells [50] and into chondrocytes [149, 157]. Font et al. designed a scaffold for tendon/ligament-to-bone tissue engineering with two different structures in one scaffold [51, 52]. More often, silk fibroin is also used for bone tissue engineering [19, 47, 56, 117, 131, 145, 175, 177].

A bioactive factor can be a growth factor, such as bone morphogenic proteins (BMPs), or also oligonucleotides, such as miRNA [4]. MicroRNAs (miRNAs) are small, non-coding RNAs (ncRNA) of ~ 22 nucleotides (nt). In general, they regulate the expression of mRNA (messenger-RNA). The posttranslational mechanism for doing so is sequence-specific and either induces mRNA degradation or represses translation [63, 84, 137, 159, 173]. miRNA is transcribed from different genomic locations as primary miRNA by RNA polymerase II [22, 137]. In the nucleus, the pri-miRNA forms a $\sim 60 - 70$ nt stem loop [3, 173] by means of cleavage. This form is called miRNA precursor (pre-miRNA). The cleavage is performed by Drosha RNase III endonuclease with a 3' overhang and a 5' phosphate [3, 173]. Ran-GTP and the export receptor Exportin-5 actively transport the pre-miRNA from the nucleus into the cytoplasm [63, 173]. In the cytoplasm, the enzyme Dicer cuts before the stem loop and a overhanging branch, similar to the one on the other arm, accrues. The double-stranded RNA is composed of the miRNA strand and the miRNA* strand, which degrades in the cytoplasm. A helicase unwinds the miRNA:miRNA* duplex [10]. The exact mechanism of unwinding miRNA is unknown [10, 22]. The freed miRNA directs the RNA-induced silencing complex (RISC) to either mRNA cleavage or translational repression [10, 137].

miRNAs are detectable not only in cells but also in the extracellular milieu, such as blood, saliva, tears, cerebrospinal fluid, amniotic fluid, breast milk and urine [84, 159]. Moreoever, extracellular miRNAs are detected in cell culture medium [159]. Those, who are secreted into peripheral body fluids, are also called circulatory miRNA [84]. Some miRNAs are specific for tissue, such as miR-1, miR-133 and miR-206 for muscle or miR-122 for liver [29, 58]. Many others are ubiquitously expressed at various levels [58]. Other miRNAs show possible potential as bone biomarkers or osteoprotective agents [48, 68].

Over the last years, an increased interest in miRNA as possible biomarkers for various diseases has been described [9, 11, 29, 122]. In preclinical models, some miRNAs are already detected as dysregulated, such as in a failing heart, e.g. miR-15, miR-25, miR-34 miR-652 etc. [12]. miRNA expression also shows a dysregulation in human cancer [46, 91]. Furthermore, also in inflammatory, neurodegenerative or cardiovascular diseases, aberrant miRNA expression patterns are detectable [46]. As examples, miR-21 expression has an impact in cardiac hypertrophy, miR-196 in Crohn's disease and miR-146a expression has an influence in rheumatoid arthritis [46]. In Wnt signaling, specific miRNAs regulate components and inhibitors of the signaling pathway [100]. Mäkitie et al. show that for an autosomally dominant WNT1, osteoporosis-specific miRNA patterns are upregulated (miR-18a-3p and miR-223-3p) and other miRNAs are downregulated (miR-22-3p, miR-31-5p, miR-34a-5p, miR-143-5p, miR-423-5p and miR-423-3p) [100]. miR-22-3p, miR-31-5p and miR-34a-5p are known inhibitors of the Wnt signaling pathway [100]. Seeliger et al. found that nine miRNAs were upregulated in serum of female osteoporotic patients (miR-21, miR-23a, miR-24, miR-93, miR-100, miR-122a, miR-124a, miR-125b and miR-148a) [155]. Additionally, five miRNAs from bone

tissue were also upregulated (miR-21, miR-23a, miR-24, miR-25, miR-100 and miR-125b) [155]. Kelch et al. also show that eight out of the nine detected miRNAs in serum are sex-independent, only miR-93-5p shows no difference [77]. Most miRNAs, which are directly or indirectly associated with osteoporosis, are related to bone formation or osteoclast activity [154].

Backes et al. found that many miRNAs are not specific for a single disease. They recommend considering a combination of various miRNAs for more specificity [6]. Those signatures are more powerful biomarkers than a single miRNA [6]. It had also been suspected that miRNA could be used as early detection of diseases, but studies often showed that only in late-stages of the disease, a dysregulation of miRNA is observed [6]. The expression of miRNAs in blood is also age- and sex-dependent [112]. miRNAs are furthermore regulators of bone formation, e.g. miR-204, miR-433 or miR-133a for RunX2 [122].

As miRNAs have the potential as biomarkers, they also can be used as starting point for bone tissue engineering and drug delivery approaches. If a gene is detected, which is over- or underexpressed in a specific tissue or disease and an influencing miRNA is detected, the inhibitor or mimic of this miRNA sequence can be used to generate a normal expression level. This leads to a gene therapy approach, which is suggested for bone regeneration with the goal of preservation or modulation of therapeutic proteins [176]. By now, there are several studies available, in which *in vivo* scaffolds were implanted already in patients. The used scaffolds were incorporated with transfected or transduced cells with miRNA mimics or antagomirs for better bone healing [4]. However, developing scaffolds, which can deliver miRNAs or anti-miRNAs specific for osteoporosis, is still not available as therapeutic possibility.

3. Material and Methods

A table of all used materials with the detailed information can be found in the Appendix A.1. The cell culture plasticware were ordered from Eppendorf AG (Hamburg, Germany). The 96 well plates for PCR were ordered from BRAND GMBH + CO KG (Wertheim, Germany).

The used equipment is listed in the Table 3.1 and the used software in Table 3.2.

Table 3.1.: Table of used equipment

Device	**Specification**	**Company**
bench	BDK-SB 1800	Weiss Pharmatechnik, Hude (Oldenburg), Germany
centrifuge	5415 R and 5810 R	Eppendorf, Hamburg, Germany
incubator	Hera cell 150	Thermo Fisher Scientific, Waltham, MA, USA
count chamber	Neubauer improved	Carl Roth, Karlsruhe, Germany
microscope	Axiovert 40C	Zeiss, Oberkochen, Germany
digital microscope	VHX-6000	Keyence, Kyoto, Japan
fluorescence microscope	BZ-9000	Keyence, Kyoto, Japan
confocal microscope	Nikon A1	Nikon Instruments, Amsterdam, The Netherlands
PCR cycler	CFX96 Real Time System plus C1000 touch cycler	BioRad Laboratories, Hercules, CA, USA
micro-CT	SkyScan 1176	Bruker, Contich, Belgium
spectrometer	FLUOstar Omega	BMG Labtech, Ortenberg, Germany
spectrophotometer	Nano-Drop ND-1000	Thermo Fisher Scientific, Waltham, MA, USA
biomechanical testing machine	ZwickiLine Z2.5	ZwickRoell GmbH & Co. KG, Ulm, Germany
load cell	KAF-Z2.5, Class 0.05 %	A.S.T. GmbH, Dresden, Germany
SEM	JSM-6390	Jeol Us Inc., Peabody, MA, USA
Raman microscope	Alpha300 R	WITec, Ulm, Germany
Objective for Raman	EC Epilan-Neofluar	Carl Zeiss GmbH, Jena, Germany

Table 3.2.: Table of used software

Name	Company
Graphpad Prism version 7.05	GraphPad Software, Inc.,San Diego, CA, USA
NRecon version 1.7.4.2	Bruker, Contich, Belgium
DataViewer version 1.5.4	Bruker, Contich, Belgium
BatMan (Plug-In in CTAn)	Bruker, Contich, Belgium
CTAn version 1.17.7.2	Bruker, Contich, Belgium
CTVox version 3.3	Bruker, Contich, Belgium
Microsoft Paint version 1803	Microsoft Corporation, Redmond, Washington, USA
MATLAB version 9.5 (R2018b)	The MathWorks Inc., Natick, MA, USA

3.1. Sample preparation for the used methods

Solely femoral heads were used as bone tissue samples in this thesis. All used femoral heads were collected in the years 2016 to 2018 at the Department of Trauma Surgery and the Department of Orthopedics and Sports Orthopedics at the university hospital Klinikum rechts der Isar. Patients provided informed consent. The ethical committee of Klinikum rechts der Isar granted permission to collect the tissue. All procedures were carried out in accordance with the declaration of Helsinki in its latest amendment. All patients had the indication for a total endoprosthesis at the hip because of a fall or because of osteoarthritis of the hip. Exclusion criteria for all patients were the following: Known treatment of Diabetes mellitus type 1 and 2 or additional treatment with vitamin D. Furthermore, treated osteoporosis patients were excluded (see Section 2.3.2 for drugs). Because of those criteria, five patients needed to be excluded. However, those five patients with diagnosed osteoporosis were used as reference group for the micro-CT classification. For the used methods described in the following, the individual femoral heads needed to be divided into several samples, due to different requirements of the used methods. The detailed description of every sample preparation can be read in Section 3.1.1 to 3.1.3. Shortly, for micro-CT, Raman spectroscopy and biomechanical testing, bone slices were required and the rest of the bone sample was used for osteoblast isolation. The complete sample collection needed to be performed under sterile conditions to be able to conduct the osteoblast isolation afterwards. An overview of the sample number for the bone characterization can be found in Tab. 3.3. For the later described *in vitro* evaluation of the fabricated scaffolds (Section 3.4), adipose-derived mesenchymal stem cells (AMSC) were used. The isolation of AMSC is described in Section 3.1.4.

Table 3.3.: Table of all used bone samples (n) and the sample shape per method

Method	Sample number n	Shape
micro-CT	58	slice, cube
Raman spectroscopy	18	slice
Biomechanical testing	29	cube
Osteoblasts isolation	18	-

3.1.1. Sample preparation for micro-CT and Raman microspectroscopy

Due to the size of the femoral head, the micro-CT scanning time is very long. In the process, the sample warms up and consequently, a possible damage of the osteoblasts could not be excluded. The scanning time for the total femoral head could not be reduced without any loss of image quality. Therefore, a representative sample was necessary. In addition, the total femoral head of some samples would not have fitted into the scanning chamber. For this reason, a slice was cut out of the femoral head along the main load axis. The reference point was the *Fovea capitis femoris* (Fig. 3.1). For dividing the femoral head, the first cut was shifted a bit from the middle into the anterior direction. The slice was taken from the middle to the posterior direction. For the second cut, a custom-made sawing aid (Fig. 3.2) was used to get a 3 mm slice. It was difficult to firmly hold some of the bones during the whole cutting process with the sawing aid. Those bones were first scratched at the right thickness and then cut free-handedly. After cutting the bone slices, samples were washed with PBS, fixated with 3.7 % formaldehyde over night and stored at 4 °C in 70 % ethanol. These slices were also used for Raman microspectroscopy.

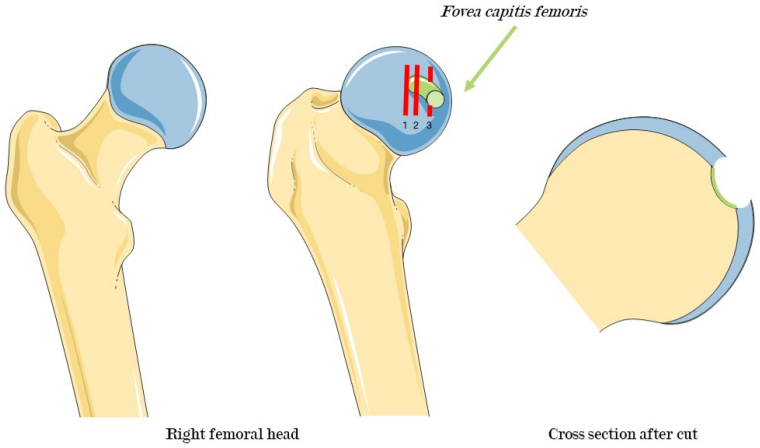

Figure 3.1.: Schematic pictures of the cutting lines. Frontal view of a right femoral head and with position of the *Fovea capitis femoris*. Frontal view of the cross section after cutting. The red lines indicate the three cutting lines and the numbers (1 to 3) represent the order of cutting

3.1.2. Sample preparation for biomechanical testing

For biomechanical testing, a cube with the dimensions $10 \times 5 \times 10$ mm was cut out of a 5 mm thick slice (Fig. 3.3). First, the 5 mm slice was cut in posterior direction using the custom-made sawing aid (Fig. 3.2). Secondly, the center of the slice was defined with three orthogonal cutting lines. The main load axis was determined by either the half angle between the *Fovea capitis femoris* and super-thin cartilage or by a mean angel of 66.7 °. The mean angle was defined by using $n = 9$ samples during a pre-test performed for this purpose. The super-thin cartilage and the *Fovea capitis femoris* were clearly visible in those samples. The result was a mean angle of 66.7 °$\pm$ 6.22 °. The center of the bone slice was chosen as the lower border of the cube. The upper boarder of the cube was chosen 10 mm outwards on the main

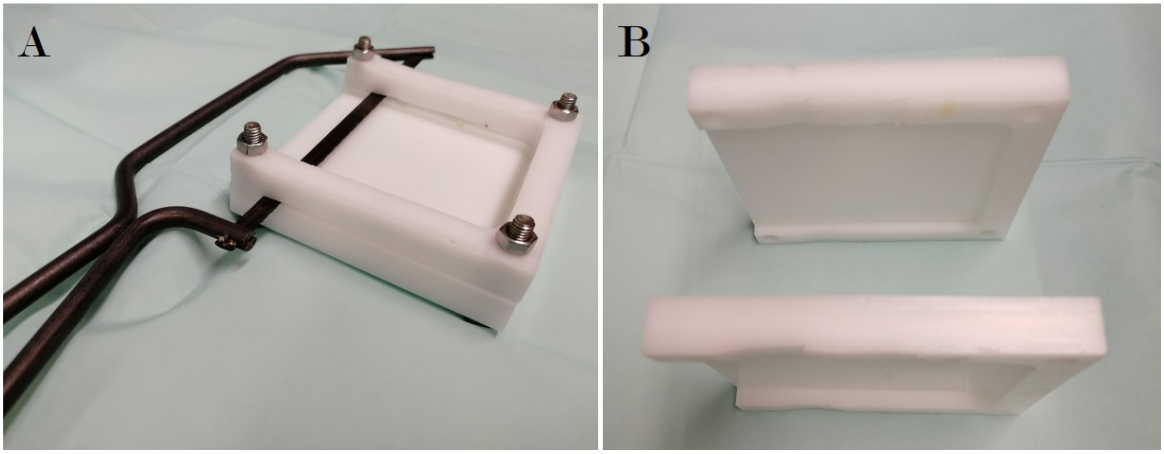

Figure 3.2.: Pictures of the custom-made sawing aid. A: Complete order of the saw and the sawing aid; B: The two different supports with depths for the 3 mm and 5 mm thick slice.

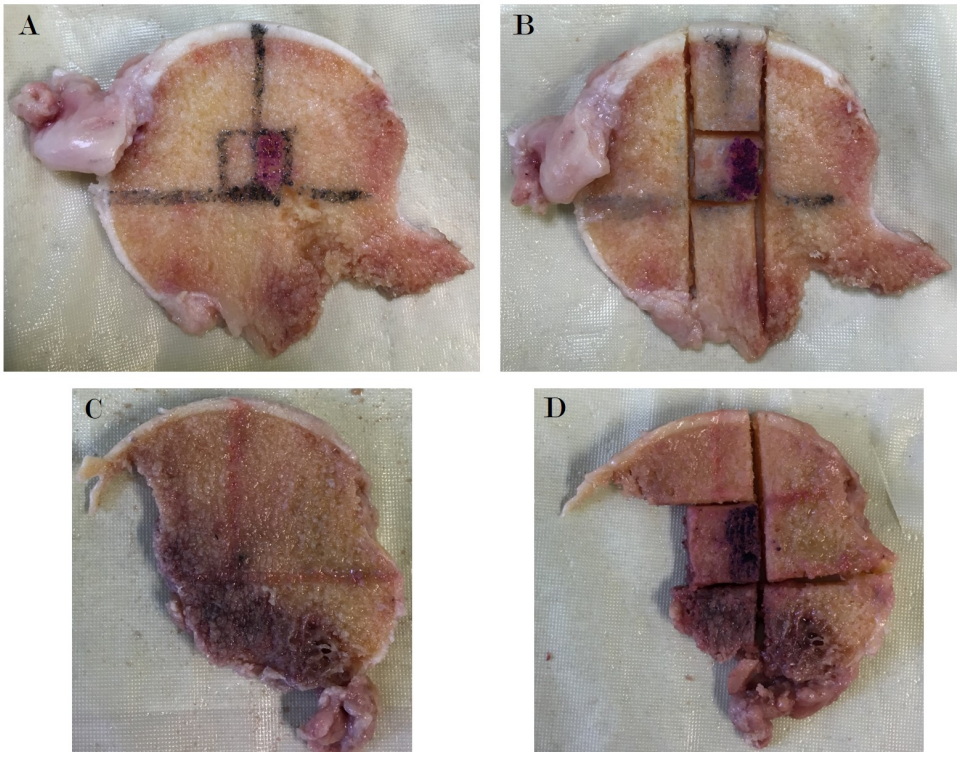

Figure 3.3.: Examples of two bone samples including cutting lines of the cube. Above, a nearly complete femur head (A, B) and below an example of an incomplete femur head, which is still suitable for cutting (C, D); A,C: lines marked; B,D: after cutting the cube.

load axis. The sides were defined by a 5 mm distance from the main load axis on both sides. Representative bone slices with the cutting lines described before are shown in Fig. 3.3. The cube was then stored in PBS and frozen at −20 °C.

3.1.3. Isolation of osteoblasts

For the isolation of osteoblasts, the leftover femoral head fragments were used. First, the cartilage was cut away with a Luer's pliers. Then, the cleared trabecular bone was sterilely cut into smaller pieces and transferred into a 50 mL reaction tube filled with 25 mL PBS. The tube was closed and the bone fragments were washed by gently shaking two to three times vertically. After that, the reaction tube was put back into the rack and after 30 s to 60 s the fat-/bone marrow-containing liquid was floating. The liquid was aspirated subsequently. Depending on how much fat/bone marrow was left, the bone fragments were then washed again. 10 mL to 15 mL bone fragments were put into one 175 cm^2 cell culture flask. The fragments were gently distributed over the complete bottom of the flask and 25 mL culture medium was added. The culture medium was composed of low glucose DMEM with L-Glutamine, 10 % FCS, 5 % penicillin/streptomycin and 0.05 M L-ascorbat-2-phosphate, which was added shortly before using the medium.

The flask with the bone fragments was incubated for 7 d at 37 °C and 5 % CO_2. After that, the first medium change was performed and repeated twice a week. The bone fragments were taken out after 14 d to 21 d, depending on the cell growth. When cell nests were present over the surface of the complete bottom of the flask, the cells were passaged. For this, the cells were washed with 25 mL PBS and detached firstly enzymatically with 2 mL tryspin-EDTA per 175 cm^2 for 5 min to 10 min and secondly mechanically by tapping the flask. The detachment of the cells was checked with the microscope. When all cells were detached, the reaction was stopped by adding 10 mL of supplemented culture medium. The cell solution was transfered into a 50 mL reaction tube and centrifuged at 500 rcf for 10 min with brakes (5/5). The supernatant was aspired and the cell pellet was resuspended in culture medium. Afterwards, it was divided between three to four flasks and cultured under the above-mentioned conditions until the cells were confluent.

As soon as reaching confluence, the cells were frozen to reuse them later. For freezing, the cells were washed with 25 mL PBS and detached enzymatically and mechanically as described earlier. The suspension was centrifuged (500 rcf, with brakes 5/5) and resuspended in 10 mL culture medium. Furthermore, the cells were counted by using the trypan blue exclusion method. The cell density and the required freezing medium were calculated. The freezing medium was composed of 50 % culture medium, 40 % FCS and 10 % DMSO. If the volume of culture medium from resuspending was too high, the suspension was again centrifuged and the pellet was suspended in the necessary amount of medium. The freezing cell density was 1×10^6 to 2×10^6 per mL. To provide a constant freezing rate, (1 °C/min) a freezing container with isopropanol was used at −80 °C for 1 d and then the frozen vials were transferred into the liquid nitrogen tank.

3.1.4. Isolation of AMSC

For the *in vitro* experiments, adipose-derived stem/stromal cells (AMSC) were used. All procedures were carried out in accordance with the declaration of Helsinki in its latest amendment. The AMSCs were isolated according to the methods of Schneider et al. and used with the passage number two to four. Shortly, the fat tissue was cut into smaller pieces, washed up to two times with PBS and centrifuged at 430 rcf for 10 min at room temperature. Collagenase solution was added (0.5 mg/mL solved in DPBS; 355 U/mg) and the solution incubated up to 1 h at 37 °C. After this, the digested fat was centrifuged (600 rcf, 10 min). The cell pellet was transfered into cell culture flasks and cultivated at 37 °C and 5 % CO_2. The AMSC culture medium consisted of high glucose medium supplemented with 10 % FCS and 1 % penicillin/streptomycin (AMSC medium). For the *in vitro* experiments, three donors were pooled together.

3.2. Characterization of bone tissue

The bone tissue was characterized using micro-CT (Section 3.2.1), Raman microspectroscopy (Section 3.2.2) and biomechanical testing (Section 3.2.3) to determine various parameters presented in Section 2.4 describing the bone structure, stress behavior and tissue components for the given bone samples (see Section 3.1).

3.2.1. Micro-CT measurements

For the micro-CT measurements, a Skyscan 1176 *in vivo* micro-CT scanner from Bruker was used. For scanning, the bone slices needed to be wet - otherwise, the slices are dehydrated over the scanning time. Becausse of the dehydration, the bone structure shrinks and moves during scanning and this leads to a blurred scan. Thus, for scanning, each bone slice was put into a plastic container containing cooled PBS and fixated with polystyrene. The scanner configuration was set up with a scan resolution of 18 µm, the filter Cu 0.1 mm with 90 kV and 278 µA, rotation steps of 0.5 °, a frame average of 10 and a camera offset, because of the big size of the samples. To calculate the bone mineral density (BMD), the 32 µm calibration rod pair was scanned under the same conditions as the bone slices. The phantoms were composed of epoxy resin with embedded fine calciumhydroxyapatite at concentrations of 0.25 g cm^{-3} and 0.75 g cm^{-3}.

To reconstruct the cross-section images from tomography projection images, the NRecon software was used. Only the beam-hardening was set on the basis of a straight profile over the phantom cross-section to 40 % correction. For setting up the remaining reconstruction parameters, the first bone slice scans were used as test samples for comparison. In the end, the ring artifact correction was chosen with a value of 15. The smoothing was set up with a smoothing level of 5 and a Gaussian smoothing kernel of 2. The histogram was displayed in logarithm scale from a range of 0 to 0.025. The misalignment compensation was adjusted in try-and-error fashion for every sample individually, as described in the manual provided by Bruker [17]. After the reconstruction, samples were rotated to the xy-plane with the help of the software DataViewer to be analyzed easier at a later stage (Fig. 3.4).

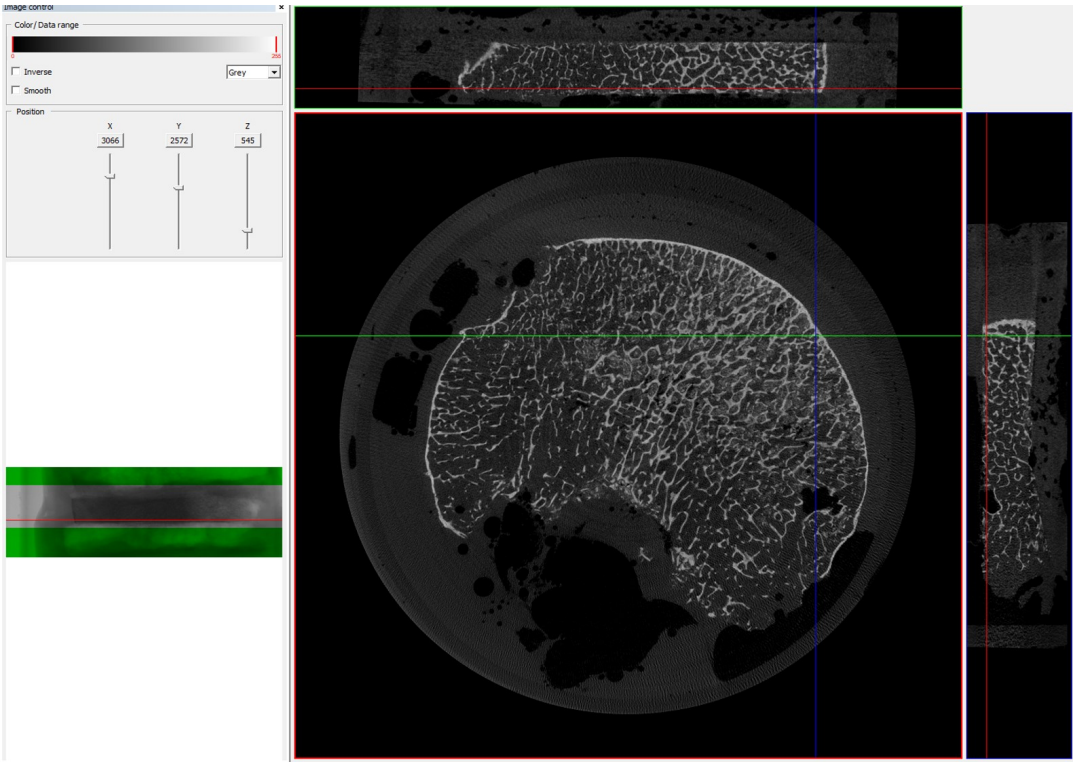

Figure 3.4.: Screenshot of a bone sample, which is processed in the software DataViewer for the optimal xy-orientation.

As the dimension of the used bones was highly irregular, an as large as possible region of interest (ROI) needed to be selected to determine a sample-specific BMD value. The ROI had to cover the trabecular area. A freehandedly drawn shape in the software was difficult to implement, because of the strongly irregular shape of the samples. Externally edited images were used to create the ROI in the dataset. For this, two to four cross-sections per dataset were chosen from the beginning and from the end. If the outer shape of the sample varied strongly, cross-sections of the middle part of the sample were additionally used. The cross-section images were copied and this copy was used for editing. Those images were loaded individually into Microsoft Paint and the ROI outline shape was drawn in white, which corresponded to the maximum gray level of 255 and to the solid part of the sample. The edited image was loaded into CTAn and binarised by applying a threshold of 254 and 255. In custom processing, the global tresholding with gray levels of 254-255 was repeated to binarise the drawn outline. For filling the outlines into a solid object, the plugin “Remove pores” in 2D by image borders was used. Finally, the image was saved as monochromatic 1-bit image. The original dataset was loaded and the edited binary image-ROI was loaded via copy-edited cross-section area as “image” at the corresponding images [18]. Afterwards, the ROI dataset was saved in a subfolder.

Before the analysis of the trabecular structure of the bone could be performed, the BMD needed to be calibrated. The phantoms were scanned and reconstructed following the same protocol described for the samples. Both datasets were opened in CTAn and a circle - smaller than the phantom - was set as ROI over 100 to 200 cross sections. After this, the attenuation

Table 3.4.: List of analysis parameters determined by micro-CT for the bone slices

Percent bone volume (BV/TV)
Bone surface / volume ratio (BS/BV)
Bone surface density
Trabecular pattern factor
Polar moment of inertia
Polar radius of gyration
Total orientation (theta and phi)
Structure model index (SMI)
Trabecular separation and thickness (plus distribution)
Fractal dimension
Open and closed porosity
Total porosity
Euler number
Connectivity
Connectivity density
Degree of anisotropy

Table 3.5.: Task list for bone slice analysis

Reload Image
Reload ROI
Tresholding: Global, grey values: 72-255
Despeckle: Remove white speckles (2D space), less than 10 pixels
Save bitmaps (image inside ROI)
3D analysis

coefficient (AC) of the volume of interest (VOI) was measured by selecting the histogram from dataset and then by using toggle VOI view. The AC for the corresponding phantom was provided by the mean (total) at the attenuation coefficient tab. Those two acquired values were then used to calibrate the BMD in "Preferences" in the CTAn menu.

For simplification of the BMD analysis of the 58 samples, the ROI datasets were loaded into BatMan together with the corresponding ROI. The used task list only consisted of the plug-in "histogramm" with the following settings: BMD in 3D inside VOI and all results were saved in one file. Moreover, additional parameters were analyzed to acquire characteristic values describing the bone morphometry (see Tab. 3.4). For this, the ROI dataset of the bone samples was loaded into BatMan. Again, the corresponding ROI was loaded, but this time with a new task list (see Tab. 3.5). CTVox was used for visualization of representative samples.

3.2.2. Raman microspectroscopy

For analyzing the composition of the bone samples, a Raman microscope was used. The bone slices were stored in PBS overnight to eliminate any ethanol residues. For the Raman measurement, the sample was put in a glass-bottom dish and covered with PBS against

dehydration during the measurement. The Raman microscope was equipped with a 785 nm diodes laser, and an objective with a 10x magnification. The grating conditions was 300 g mm, BLZ = 750 nm. The output laser beam was set on 50 mW. For data acquisition, a cooled CCD camera with a resolution of 1024 × 128 pixel was used. The scanned area was 600 × 600 µm, with 150 points per line and 150 lines per image. The analyzed area was in the center of the slice under the *Fovea capitis femoris*. All Raman spectra were background-subtracted to eliminate background information of the glass-bottom dish and of the PBS.

3.2.3. Biomechanical testing

For biomechanical characterization of the bone cubes, the unconfined compression method was used. All used samples were blind-tested. Therefore, the samples were numbered from 1 to 29 without knowing the classification. The thawed samples were placed 30 mm off the front egde and preloaded with 1 N to 5 N so that the upper panel had full contact to the sample (Fig. 3.5). The compression in the elastic area was between 2 % to 3 % strain for five cycles. Finally, a load-to-failure test with a termination criterion of 40 % force decrease was performed.

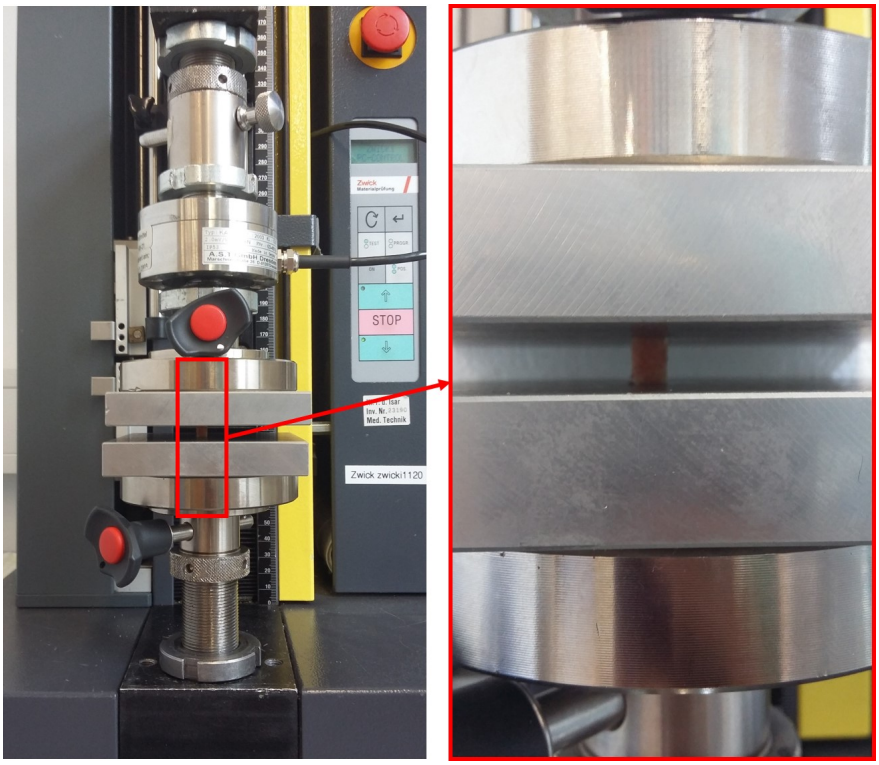

Figure 3.5.: Setup for the biomechanical testing. left side: total view, right side: zoom in on the sample.

The parameters of interest were the maximal force per cube and also per area (F_{max}, $F_{max,area}$), the relative strain, the Young's modulus, the toughness and the Poisson ratio. To determine the Poisson ratio, a picture was taken after preloading, after cycle 5 at maximal strain and after load-to-failure. Additionally, the Young's modulus and the toughness were calculated via

MATLAB script [109]. For calculation of the Young's modulus, the slope of the load-to-failure curve was used. Thereby, the maximal force during cycles 2 to 5 was the end point and the minimal force during those cycles was the starting point of the calculation. For this, only the upper 50 % of data were used for the calculation of the regression line in the linear-elastic part. For calculating the toughness, the definition of Turner and Burr needed to be modified [170]. In this study, the toughness is determined by the distance between the area in the elastic range (minimum of the 5th cycle) and the maximal force at load-to-failure (F_{max}), because the plastic area was not clearly visible. The area was calculated with the help of the function "trapz" in MATLAB.

Additionally, the bone cubes were scanned before and after testing with the micro-CT to compare the samples with the bone slices. The scanning parameters were the same as for the bone slices (Section 3.2.1). The BMD was calibrated with the 16 mm diameter calibration phantoms from Bruker. The reconstruction was conducted in a similar way to the reconstruction of the bone slices.

3.3. Production and characterization of the scaffolds

Micro-CT, Raman spectroscopy and biomechanical testing, as described in the last sections, were used for diagnostics. In the next sections, the production and characterization of scaffolds for a therapeutic approach are described. For this, the scaffolds needed to be produced and characterized. Three scaffold types were produced and tested: one scaffold with a low fibroin content (LF), one with a high fibroin content (HF) and one modified HF scaffold, in which the surface of the extrusion target was modified (HF+). The extrusion target is the surface, where the fibroin solution is extruded under pressure. In the production of the scaffolds, two different extrusion targets are used, an aluminum dish and a plastic dish with a superhydrophobic surface. The exact production steps are described in Section 3.3.1. Low fibroin content was 2 % fibroin and high fibroin content was 4.7 % fibroin. The high fibroin concentration was the maximal fibroin concentration in the solution, which can be generated without any additional and time-consuming concentration steps. The used methods for structural analysis of the scaffolds are described in Section 3.3.2.

3.3.1. Scaffold production

For the scaffold fabrication, a fibroin solution needed to be produced. For this purpose, the protocol of Rockwood et al. was modified [147]. In the following, the procedure will be shortly described. First, the silk cocoons were cut into small pieces and boiled in 1.1 g/L and 0.4 g/L sodium carbonate for 1.5 h. Thereafter, the fibers were rinsed with water several times and then dried overnight. On top of the dried fibers, 9.3 M lithium bromide (LiBr) was added and incubated for 2.5 h at 65 °C. A dialysis cassette (3.5K MWCO) was filled with the dissolved fibers in LiBr and dialyzed against ultra-pure water for three days with several water changes per day. The silk solution was removed from the cassettes and filtrated through a glass filter. The concentration of the silk fibroin was photometrically measured at a wavelength of 280 nm. This solution was directly used for the scaffold foaming. The foaming preparation steps are described in more detail by Maniglio et al. in a patent and a paper [103, 105]. Shortly, the

aqueous solution is foamed with nitrous oxide at 10 bar with a commercial shipper with a needle extruder of 2 mm diameter. The extrusion target was an aluminum dish for the LF and HF scaffolds. A superhydrophobic surface of a plastic dish was the extrusion target for the HF+ scaffolds. The plastic dish was treated with the Neverwet Multi Purpose Kit. All types of scaffolds were frozen in liquid nitrogen and then lyophilized for 1 d. After this, they were bathed in pure methanol for 5 min, 80 % methanol for 5 min and in pure bi-distilled water for 10 min. After the bathing, they were again lyophilized for 24 h. At the end, the fibroin sponge was cut into smaller cubes of $5 \times 5 \times 3$ mm dimensions.

3.3.2. Structural analysis

For characterization of the superficial structure and the pore morphology of the produced scaffolds (Section 3.3.1), images with a digital microscope, a scanning electron microscope (SEM) and images with a micro-CT were taken. For the digital microscope images, the dry scaffold without cells was photographed with the VHX-6000.

Images of the scaffolds's surface at higher magnifications were achieved by using the SEM. For the images, the scaffolds were fixated with an ascending alcohol series (30 %, 50 %, 70 %, 80 %, 90 % and 100 %). The scaffolds were incubated twice in each solution for 15 min. After this alcohol series, the scaffolds were dried under the fume hood at room temperature. The scaffolds were sputtered with gold and images were taken with an accelerating voltage of 5 kV and a magnification of 100x and 2500x.

For analyzing the pore morphology, the scaffolds were scanned with the Skyscan 1176. Because of the low opacity, the scaffolds were put in a 1:5 dilution of Lugol's iodine for 20 min. After this, the scaffolds were shortly dabbed with a piece of paper towel, fixed in polystyrene tubes and scanned with no filter at a 9 µm resolution with 40 kV and 600 µA. The rotation step was 0.3 ° and a frame average of 10 was used. As the scaffolds appeared crushed after scanning and also after the treatment, new scaffolds were stained via iodine evaporation for 21 d. During the evaporation time, the used scaffolds stayed in shape and were scanned as mentioned before. For reconstruction of the scaffolds, the images were loaded into NRecon and the following parameters were adjusted: Smoothing 2 with Gaussian smoothing kernel of 2, beam-hardening of 5 % and a ring artifact correction with a value of 8. The parameters of the task list for the 3D analysis are listed in Tab. 3.6.

Table 3.6.: Task list for structural analysis of the scaffolds

Reload image
Reload ROI
Tresholding: Adaptive, grey values: 30-255
Closing: Round with radius 2 (2D space)
Despeckle: Remove white speckles (2D space), less than 20 pixels
Despeckle: Remove black speckles (2D space), less than 20 pixels
Opening: Round with radius 1 (2D space)
Save bitmaps (image inside ROI)
3D analysis

3.3.3. Load testing with fluorochrome-linked protein

For testing the affinity of the scaffold to bind biomolecules, a fluorescein isothiocyanate-labeled bovine serum albumin (FITC-BSA) was used. FITC-BSA was solved in water to prepare a stock solution with a concentration of 1 ng/mL. For the experiment, this stock solution was diluted 1:10 in low glucose DMEM medium without serum and antibiotics. After this, the scaffold was stored in the solution for 30 min. Afterwards, the scaffold was washed with PBS two times and pictures were taken directly and again after 3 h with the fluorescence microscope (BZ-9000).

3.4. In vitro evaluation of scaffolds

In addition to the structural analysis of the produced scaffolds (Section 4.2.1), the capability for biocompatibility needed to be analyzed (Section 3.4.2 - 3.4.3). The experiments for the cell adhesion were performed with the isolated AMSC, as described in Section 3.1.4, because the number of available osteoblasts was limited.

3.4.1. Cell culture

Before the scaffold could be used for cell culture, they needed to be sterilized with 70 % ethanol by washing several times and subsequently, they were incubated over night with the culture medium at 37 °C. The cell density per scaffold was 0.1×10^6 cells (for their production see Section 3.3.1). The cells were cultured with the AMSC medium described in Section 3.1.4 at 37 °C and 5 % CO_2. Cell culture medium was changed twice a week. The cultivation time for the proliferation and cytotoxicity assay was 3 d, 7 d and 14 d (see Section 3.4.2). For the different imaging methods of the scaffolds, the cultivation time was 7 d and 14 d (see Section 3.4.3 - 3.4.4). Three scaffolds were used per condition, if not indicated otherwise.

3.4.2. Cytotoxicity and proliferation

The proliferation of the cells on the scaffold was quantified with a Quant-iT PicoGreen dsDNA Assay Kit following the manufactures recommendations. The seeded scaffolds were incubated with sterile water and then frozen at −80 °C. Once all samples were collected, they were again thawed and frozen two times so that all cells were dead and bursted due to the temperature shift and the osmotic pressure of the water. The thawed supernatant was used for the assay, which was measured with the spectrometer at an excitation of 480 nm and an emission of 520 nm. A standard curve of known dsNDA content was used for calculating the dsDNA amount of the samples.

To determine a possible effect of the scaffolds on cell viability and mitochondrial activity, a 3-(4,5-dimethylthiazol-2-yl)-2,5-diphenyltetrazolium bromide (MTT) assay was used. The cultivated scaffolds were washed with PBS and thiazolyl blue (1.2 mM) was added for 2 h at 37 °C and 5 % CO_2. The consequently appearing blue precipitates occurred because of the metabolically active cells, which transformed MTT to formazan. The MTT precipitates were dissolved with a solubilisation buffer (10 % SDS/0.6 % acetic acid in DMSO buffer). For the

measurement, 100 µl were transferred to a 96-well plate in biological triplicates. The optical density was measured at 570/690 nm via the photometer.

3.4.3. Cell adhesion as assessed by scanning electron microscopy (SEM)

To evaluate the cell adhesion on the scaffolds after AMSCs cultivation, SEM images similar to the images for the characterization of the scaffold surface were taken (see Section 3.3.2). The cultivation was performed as described in Section 3.4.1 and the cultivation time was 7 d and 14 d. The preparation of the seeded scaffolds was conducted according to the method described in Section 3.3.2. Firstly, overview pictures were taken with a magnification of 33x and 1000x and then, after localization of the cells, pictures of up to 2500x magnification were taken.

3.4.4. Confocal images of cell seeded scaffolds

The cell morphology and distribution in the scaffolds was analyzed by confocal microscopy. The seeded scaffolds, as described in Section 3.4.1, were washed with PBS and incubated with 3.7 % formaldehyde for 1 h at 37 °C. After this, they were again washed with PBS and stored until the staining at 4 °C. For the staining, the cells needed to be permeabilized with 0.2 % Triton X-100 in PBS for 20 min at room temperature. After a washing step with PBS, Oregon Green 488 Phalloidin and DAPI were added according to the manufacturer's instructions. After the incubation time, the scaffolds were washed to remove unbounded reagents and the confocal images were taken.

3.5. Transfection of osteoblasts using scaffolds and miR-100-5p inhibitor

After the evaluation of a potential scaffold for a therapeutic approach (see Section 3.4), the isolated osteoblasts from a total of 18 healthy and osteoporotic donors (see Section 3.1.3) were analyzed with regard to miR-100-5p expression (see Section 3.5.1). As formerly described, Seeliger et al. and Kelch et al. found that the expression level of miR-100-5p is upregulated in osteoporotic patients. Unfortunately, only samples from one single osteoporotic donor with high miR-100-5p expression were among the screened osteoblasts. However, this was sufficient for testing the therapeutic approach of miR-100 inhibition in 3D with the produced HF scaffold for the first time (see Section 3.5.2).

3.5.1. Osteoblasts screening for miR-100-5p expression

The frozen osteoblasts of 18 donors were separately thawed by mixing the cells of each donor with 50 mL warm culture medium, centrifuged at 500 rcf with brakes for 10 min and each pellet was mixed with 1 mL TriReagent and immediately frozen. For the miRNA isolation, each sample was thawed and the method described by Liu et al. in [94] was used. In the following, the steps are described for one sample. The sample was incubated 5 min on ice, then

200 µl chloroform was added and the mixture was shortly vortexed. After 10 min incubation on ice, the reaction tube was centrifuged at 14 000 rcf for 10 min at 4 °C. After centrifugation, the RNA-containing aqueous phase was transferred into a new reaction tube filled with 500 µl isopropanol. Subsequently, the reaction tube was swayed cautiously, incubated on ice for 10 min and centrifuged again. The pellet was washed and centrifuged two times with 70 % ethanol. Afterwards, the supernatant was decanted and the pellet was resuspended with 20 µl ultra-pure water. The quantification of the isolated RNA was carried out on the NanoDrop ND-1000 spectrophotometer. The RNA was measured at 260 nm. The purity of the RNA was quantified by the correlation 260/280 nm and 260/230 nm. A value around 2 indicates a good purity.

For the cDNA transcription, the miScript II RT Kit was used as specified by the manufacturer. As only the mature miRNA was of interest, the HiSpec Buffer was used. Per reaction, 2 µg RNA was used. The cDNA was diluted to a concentration of 3 ng/µl. The miScript Primer Assay and 2x QuantiTect SYBR Green PCR were used for the real-time PCR and the detection of miR-100-5p and SNORD96a as reference gene. The PCR was performed in a 96-well plate as recommended by the manufacturer . The reaction mix per well contained 12.5 µl 2x QuantiTect SYBR Green, 2.5 µl 10x Universal Primer, 2.5 µl 10x Primer, 6.5 µl nuclease-free water and 1 µl template cDNA. Figure 3.6 shows the cycling conditions for the real-time PCR on the BioRad cycler CFX96 in detail. The relative gene expression was calculated by using the $2^{\Delta C_T}$ method with the reference gene (SNORD96a), where $\Delta C_T = C_{T(\text{reference})} - C_{T(\text{sample})}$.

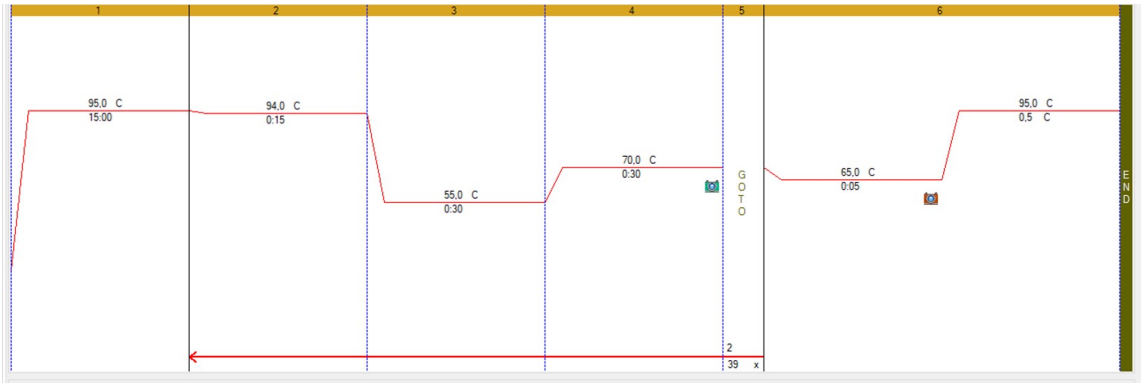

Figure 3.6.: Cycling conditions for the real-time PCR of the miRNA. An initial activation step was performed at 95 °C for 15 min. Next, a short denaturation cycle of 15 s at 94 °C, followed by an annealing cycle (30 s at 55 °C) and an extension cyle (30 s at 70 °C) was performed 40 times in total. After the 40 cycles, an increase in temperature from 65 °C to 95 °C in 5 s was induced to measure melting curves. The fluorescence was measured at the indicated camera points.

3.5.2. Transfection of osteoblasts using miR-100-5p inhibitor loaded scaffolds

For the transfection of the osteoblasts, the scaffolds needed to be loaded with the miR-100-5p inhibitor. The cell seeding and transfection was performed on the same day. The manufacturer's information for "Reverse Transfection of Adherent Cells with miRNA Mimics or

miRNA Inhibitors in 96-Well Plates" was modified, because this protocol was for 2D transfection and only for up to 5×10^4 cells. For the 3D-structured scaffolds, 1×10^5 cells were used per scaffold. For the transfection, only one donor with high miR-100-5p expression was tested. Triplicates were performed per condition. For the transfection, there were three groups:

1. Transfected with miR-100-5p inhibitor in 3D (T+)
2. Untransfected in 3D (T3D)
3. Untransfected cell monolayer (T2D)

The additional controls included a mock transfection control (only transfection reagent without addition of miRNA inhibitor), a positive control with co-transfection of mimic and inhibitor of miR-1 and a negative control with miScript Inhibitor negative control, which had no homology to any known mammalian gene. Additionally, the cells were only transfected with miR-1 mimic. The scaffolds were loaded with 50 nM inhibitor or 5 nM mimic according to the manufacturer's recommendation. For the transfection, 1.5 µl miRNA inhibitor or 0.15 µl miRNA mimic (both stock concentration 20 µM) were mixed per scaffold with 3 µl HiPerFect in 15.5 µl low glucose DMEM without serum. After 20 min of incubation time at room temperature, this 20 µl mixture was pipetted dropwise onto the scaffold. Thereafter, the cells were enzymatically detached by trypsin/EDTA and counted by trypan blue exclusion method. The cells were seeded on the scaffold at a density of 1×10^5 cells (in 580 µl medium). The plate was placed on an orbital shaker in the incubator and the medium was changed two times a week. The collecting time points for real-time PCR are 1 d, 3 d and 7 d. The scaffolds were mixed with 500 µl TriReagent. Because of this, 100 µl chloroform and 250 µl isopropanol were used for the RNA isolation. The miRNA isolation, transcription and real-time PCR were performed following the same protocol as described in Section 3.5.1. Furthermore, the isolated mRNA was transcribed to cDNA with First strand cDNA Synthesis kit and a real-time PCR was conducted with primers for bone morphogenic protein receptor type II (BMPR2), collagen type I (Col1) and β-tubulin as reference gene. The cycling conditions are shown in Figure 3.7 and the primer sequences are listed in Tab. 3.7. The calculation of relative gene expression was performed as described in Section 3.5.1 with the reference gene β-tubulin.

Table 3.7.: Table of primer sequences

Primersequence (Eurofins, Luxemburg)	**Sequence (5´-3´)**
BMPR2 receptor forward	GAGACGAGAGCAACAAGCTG
BMPR2 receptor reverse	TCACCTATCTGTATACTGCTGCC
Collagen type I forward	AGCGGACGCTAACCCCCTCC
Collagen type I reverse	CAGACGGGACAGCACTCGCC
β-tubulin forward	GAGGGCGAGGACGAGGCTTA
β-tubulin reverse	TCTAACAGAGGCAAAACTGAGCACC

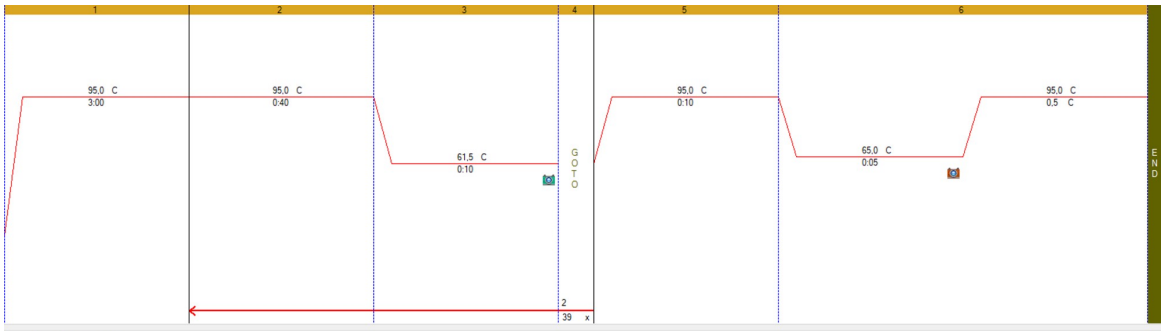

Figure 3.7.: Cycling conditions for the real-time PCR of BMPR2 and Col1. A starting denaturation cycle was performed at 95 °C for 3 min. Next, a short denaturation cycle of 40 s at 94 °C, followed by a hybridization/elongation cyle (10 s at 61.5 °C) was performed 40 times in total. After the 40 cycles, a short denaturation cycle (10 s at 95 °C) followed by an increase in temperature from 65 °C to 95 °C in 5 s was performed to measure melting curves. The fluorescence was measured at the indicated camera points.

3.6. Statistics

Statistical analysis of quantitative data was performed using GraphPad Prism version 7.05 for Windows, GraphPad Software, La Jolla California USA, www.graphpad.com. Statistical significance was considered at $p<0.05$ (Tab. 3.8). Kruskal-Wallis test with Dunn's multiple comparison correction was used for comparing more than two groups of independent samples of a non-Gaussian distribution. Mann-Whitney test was used for comparing two groups of independent samples of a non-Gaussian distribution. For testing the correlation between non-Gaussian distributed parameters, Spearman's rank correlation coefficient was used (section 4.4). Statements on significance or non-significance only apply for the results of the described study and cannot be used for general conclusions.

Table 3.8.: P-values and the corresponding statistical significance indicated by asterisks

	p-value
*	$p < 0.05$
**	$p < 0.01$
***	$p < 0.001$
****	$p < 0.0001$

4. Results

4.1. Bone characterization

As main parameter for grouping the samples into "osteoporotic", "osteopenic" and "healthy", the BMD value was chosen. In total, 58 bone slices were scanned, 29 bone slices were used for biomechanical testing and 18 bone slices were analyzed with Raman spectroscopy. If not declared otherwise, the values of the results presented in the following are the median and the 25 % and 75 % percentile. Significant results are indicated with asterisks as described in Tab. 3.8.

4.1.1. BMD and bone parameters evaluated by the micro-CT

The BMD of each sample was calculated with the maximal number of slides to reach the highest accuracy (see Section 3.2.1). The indication for some of the samples was already declared as osteoporotic based on the medical report. These patients already received medication against osteoporosis. Because of this, those samples were acknowledged as additional comparison group ("treated"). Three samples needed to be excluded, as two samples were humerus samples and one patient was diabetic. The BMD ranges for the three groups (healthy, osteopenic, osteoporotic) were chosen considering all scanned samples, their health condition and the values of the comparison group. The final ranges are:

- Osteoporotic: BMD $\leq 0.13\,\mathrm{g\,cm^{-3}}$
- Osteopenic: $0.13\,\mathrm{g\,cm^{-3}} < \mathrm{BMD} < 0.19\,\mathrm{g\,cm^{-3}}$
- Healthy: BMD $\geq 0.19\,\mathrm{g\,cm^{-3}}$

Table 4.1.: Sex distribution in the single groups of the micro-CT analysis

	osteoporotic	osteopenic	healthy	treated
female	8	9	19	4
male	2	1	11	1
total	10	10	30	5

The BMD values of the treated patients and those who had been diagnosed as osteoporotic are in the same range. Only one treated sample with a higher BMD is in the osteopenic group. The mean age in the osteoporotic group is 87.1 ± 9.6 years, while it is 77.9 ± 11.0 years in the osteopenic group and 71.2 ± 11.0 years in the healthy group. The mean age of the treated group is 79.8 ± 5.0 years. The median BMD of the osteoporotic samples is

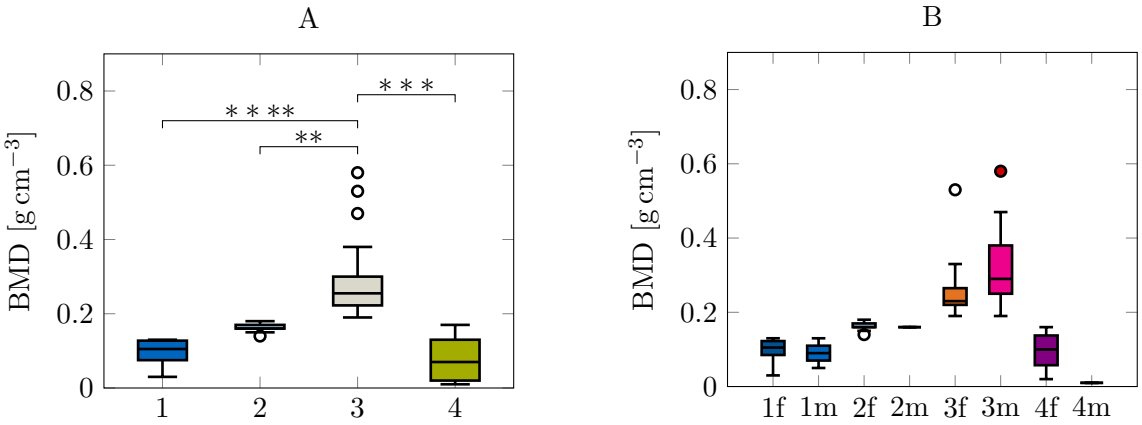

Figure 4.1.: Bone mineral density (BMD) of the various groups (A) and BMD distribution for samples collected from male and female patients (B). Median with 25 % and 75 % percentile plus maximum and minimum values and outliers (circle). Both graphs: 1: osteoporotic, 2: osteopenic, 3: healthy, 4: treated; only B: f: female; m: male. Significant values are marked as described in Tab. 3.8.

0.105 g cm^{-3} (N = 10; 25 % percentile: 0.065; 75 % percentile: 0.13), while the median of the osteopenic samples is 0.16 g cm^{-3} (N = 10; 25 % percentile: 0.1575; 75 % percentile: 0.1725) and for the healthy samples, the values are highest at 0.255 g cm^{-3} (N = 30; 25 % percentile: 0.22; 75 % percentile: 0.3025). The median of the treated samples is 0.07 g cm^{-3} (N = 5; 25 % percentile: 0.015; 75 % percentile: 0.145; Fig. 4.1 A). The BMD of the healthy group is significantly higher as compared to the osteoporotic group ($p < 0.0001$), the osteopenic group (p = 0.0029) and also the treated group (p = 0.0002; Fig. 4.1 A). In contrast, the BMD of the osteoporotic group is similar to the osteopenic group (p = 0.6121) and the treated group (p > 0.9999; Fig. 4.1 A).

Looking at sex distribution, the BMD of all male samples has a median of 0.28 g cm^{-3} (N = 14; 25 % percentile: 0.18; 75 % percentile: 0.38), which is significantly higher than the BMD of all female samples with a median of 0.19 g cm^{-3} (N = 36; 25 % percentile: 0.14; 75 % percentile: 0.23) (p = 0.0281). Contrasting to these results, the BMD of the osteoporotic male samples is significantly lower as compared to the BMD of the healthy male samples (p = 0.02556; Fig. 4.1 B). Looking at the female samples, the BMD of the osteoporotic group is not significantly different to the BMD of the osteopenic group (p = 0.4370), but it is significantly lower as compared to the healthy group ($p < 0.0001$; Fig. 4.1 B). Likewise, the BMD of the osteopenic female group is significantly lower compared to the healthy female group (p = 0.0139). The BMD of the female samples is significantly higher in the healthy group as compared to the treated group (p = 0.0015). In all groups, the number of female samples is higher than the number of male samples (Tab. 4.1). In the osteopenic and osteoporotic groups, only 3 male samples were available. This is the reason why no separation between male and female will be considered in the following analysis. In addition, the BMD of women and men resulted similar in each group (Fig. 4.1 B).

Representative samples were chosen to visualize the reconstruction of the micro-CT scans (Fig. 4.2). Looking at the bone slice photos, no obvious difference between the single groups is visible (Fig. 4.2 A-C). In contrast, the reconstructed bone slices show a particular difference

between the osteoporotic and healthy samples in the outer regions (Fig. 4.2 D, F). The outer region of the osteoporotic sample shows less trabeculae than the healthy sample.

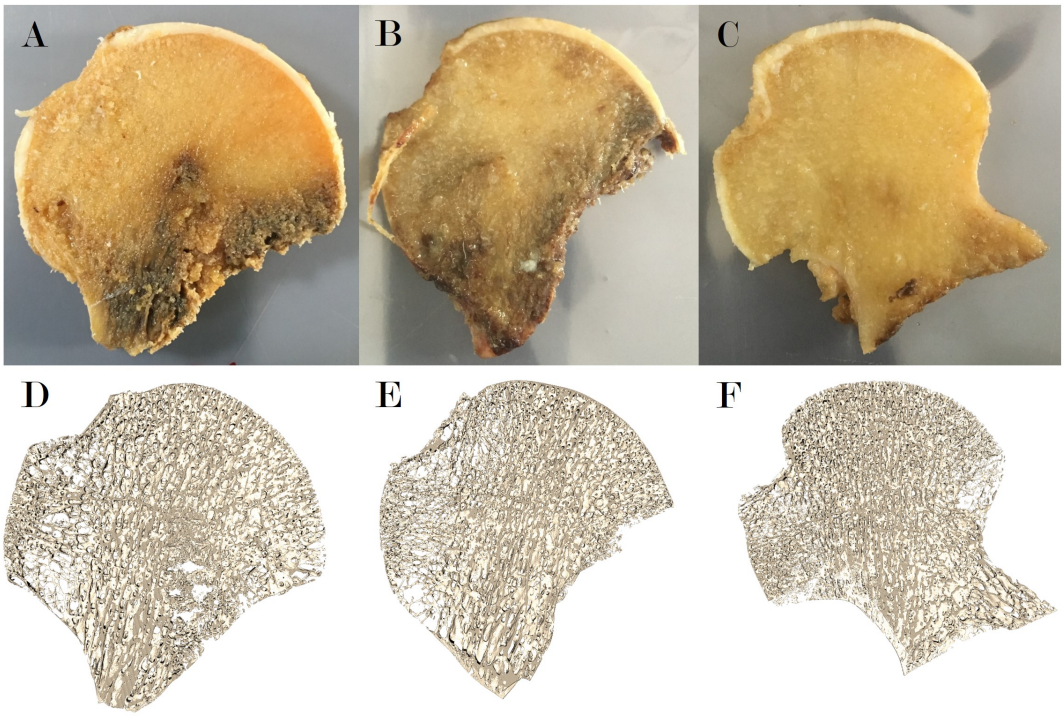

Figure 4.2.: Examples of original bone slices (A-C) and the reconstructed versions (D-F) of an osteoporotic sample (A,D), an osteopenic sample (B,E) and of a healthy sample (C,F).

An overview of mean values of selected parameters calculated by the micro-CT are listed in Table 4.2. Additionally, the percentage of bone volume and the degree of anisotropy and porosity of the bone samples are provided in Figure 4.3. Looking at the percentage of bone volume (BV/TV), there is no significant difference between the osteoporotic group and the osteopenic group ($p > 0.9999$; Fig. 4.3 A, Tab. 4.2). In contrast, the BV/TV of the healthy group is significantly higher as compared to the osteoporotic group ($p = 0.0101$) and the osteopenic group ($p = 0.0008$).

The osteoporotic samples and the osteopenic samples have a similar bone surface to volume ratio (BS/BV) ($p > 0.9999$; Tab. 4.2). In addition, the bone surface density (BS/TV), the trabecular pattern factor, the structure model index (SMI), the total orientation theta, the connectivity, the open and closed porosity values are all similar for both the osteoporotic and osteopenic samples ($p > 0.9999$; Tab. 4.2). Furthermore, there is neither a significant difference between those two groups with regard to the polar moment of inertia (MMI, $p = 0.0784$), the polar radius of gyration ($p = 0.1656$), total orientation phi ($p = 0.1435$), the fractal dimension (FD, $p = 0.4611$), the Euler number ($p = 0.3866$) and the connectivity ($p = 0.2659$; Tab. 4.2).

Comparably, the healthy samples and the osteoporotic samples have similar values regarding the MMI, the polar radius of gyration, the total orientation theta, the fractal dimension, the

Table 4.2.: Overview of micro-CT parameters obtained from the 3D analysis

			osteoporotic		osteopenic		healthy	
Description	Abbreviation	Unit	Mean	St. d.	Mean	St. d.	Mean	St. d.
Percentage of bone volume	BV/TV	%	21.26	3.73	20.56	4.22	28.07	6.14
Bone surface / volume ratio	BS/BV	1/µm	0.01686	0.00231	0.01767	0.00228	0.01488	0.00220
Bone surface density	BS/TV	1/µm	0.00354	0.00053	0.00357	0.00042	0.00410	0.00069
Trabecular pattern factor	Tb.Pf.	1/µm	0.00405	0.00121	0.00463	0.00157	0.00300	0.00124
Polar moment of inertia	MMI(polar)	μm^5	$1.193 \cdot 10^{20}$	$5.832 \cdot 10^{19}$	$6.262 \cdot 10^{19}$	$3.134 \cdot 10^{19}$	$1.483 \cdot 10^{20}$	$1.284 \cdot 10^{20}$
Polar radius of gyration	Gr.R(polar)	µm	13706.96	1029.09	12394.72	1421.87	13547.27	1817.42
Total orientation (theta)	T.Or(theta)	°	89.89	0.09	89.93	0.07	89.79	0.32
Total orientation (phi)	T.Or(phi)	°	262.15	117.87	157.52	126.82	206.70	106.31
Structure model index	SMI	-	1.42	0.27	1.54	0.39	1.17	0.37
Trabecular thickness	Tb.Th.	µm	222.37	29.07	215.67	21.83	251.34	33.35
Trabecular separation	Tb.Sp.	µm	736.01	110.48	705.79	94.50	650.10	108.74
Fractal dimension	FD	-	2.50	0.09	2.43	0.12	2.52	0.10
Closed porosity (percent)	Po(cl)	%	0.01	0.01	0.01	0.01	0.03	0.02
Open porosity (percent)	Po(op)	%	78.74	3.74	79.44	4.22	71.92	6.15
Total porosity (percent)	Po(tot)	%	78.74	3.73	79.44	4.22	71.93	6.14
Euler number	Eu.N	-	-13146.60	7174.18	-9466.80	5515.74	-13129.71	5719.32
Connectivity	Conn	-	16135.20	7604.24	11428.00	5374.12	16054.29	6712.29
Connectivity density	Conn.Dn	$1/\mu m^3$	0.000026	0.000010	0.000027	0.000008	0.000032	0.000014
Degree of anisotropy	DA	-	0.348	0.047	0.433	0.053	0.450	0.072

Euler number and the connectivity ($p > 0.9999$; Tab. 4.2). Moreover, there is no significant difference in BS/TV between the healthy samples and the osteoporotic samples ($p = 0.0851$) or the osteopenic samples ($p = 0.0755$). The same holds true regarding those two groups, as there is neither a significant difference between the BS/BV ratio ($p = 0.0737$), the trabecular pattern factor ($p = 0.0974$), the total orientation phi ($p = 0.4991$), the SMI ($p = 0.1914$) and the connectivity density ($p = 0.5486$). Furthermore, there is no significant difference between the osteopenic samples and the healthy samples with regard to the polar radius of gyration ($p = 0.1684$), the total orientation theta ($p = 0.4934$), the total orientation phi ($p = 0.8957$), the Euler number ($p = 0.0713$), the connectivity ($p = 0.0625$) and the connectivity density ($p = 0.7695$).

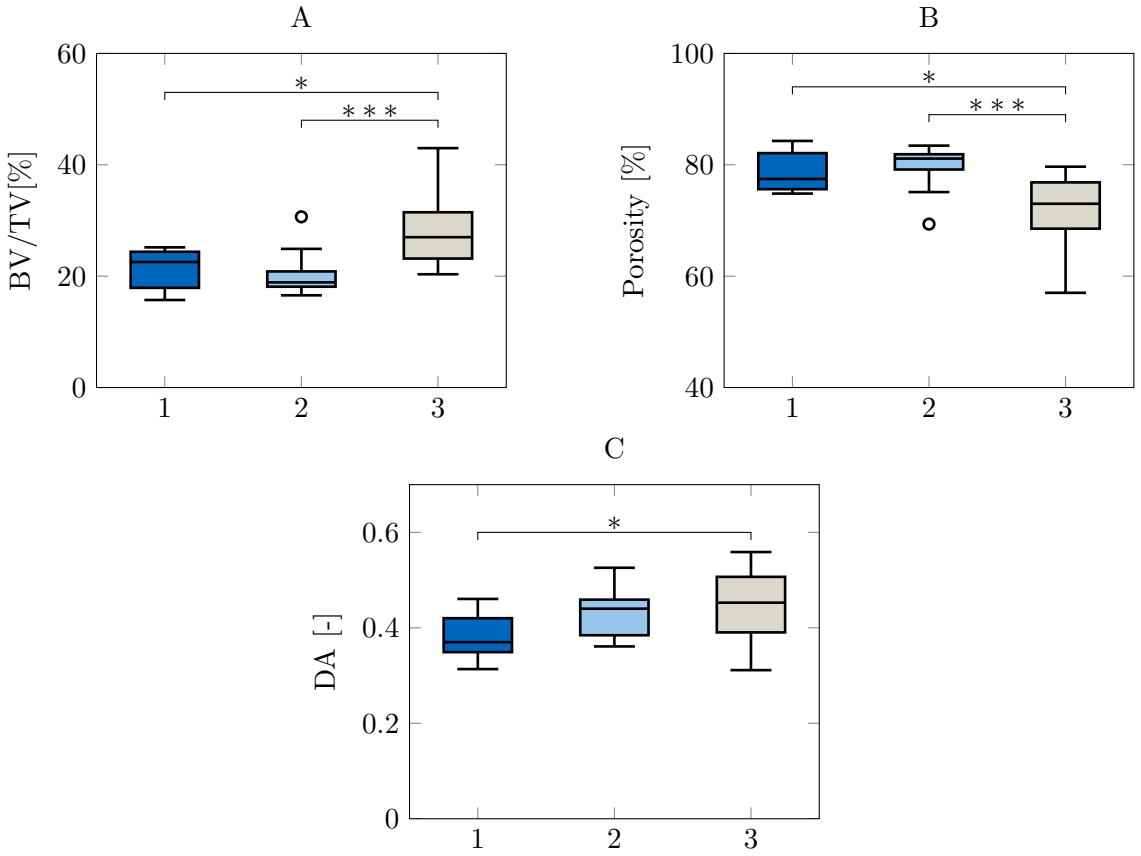

Figure 4.3.: Percent bone volume (BV/TV) (A), porosity (B) and degree of anisotropy (DA) (C) of the osteoporotic samples (1), the osteopenic samples (2) and the healthy samples (3). Median with 25 % and 75 % percentile plus maximum and minimum values and outliers (circle). Significant values are marked as described in Tab. 3.8.

The trabecular pattern factor is significantly higher in the osteopenic samples as compared to the healthy samples ($p = 0.0048$; Tab. 4.2). In contrast, the mean trabecular separation value of the osteoporotic group is similar to the osteopenic group ($p > 0.9999$) and the healthy group ($p = 0.1941$). Moreover, the mean trabecular separation value of the osteopenic group is similar to the healthy group ($p = 0.5977$). Also, the SMI is significantly higher in the osteopenic samples compared to the healthy samples ($p = 0.0110$). The FD and the MMI are significantly higher in the healthy samples as compared to the osteopenic samples ($p = 0.0423$;

$p = 0.0119$).

The closed porosity is significantly higher in the healthy samples as compared to the osteoporotic ($p = 0.0193$) and osteopenic samples ($p = 0.0068$; Tab. 4.2). Furthermore, the open porosity is significantly lower in the healthy samples as compared to the osteoporotic ($p = 0.0101$) and osteopenic samples ($p = 0.0008$). Furthermore, the total porosity is significantly lower in the healthy group as compared to the osteoporotic ($p = 0.0101$) and the osteopenic group ($p = 0.0008$), respectively (Fig. 4.3 B, Tab. 4.2). The total porosity of the osteopenic group is similar to the osteoporotic group ($p > 0.9999$). The degree of anisotropy (DA) is significantly higher in the healthy group as compared to the osteoporotic group ($p = 0.0336$; Fig. 4.3 C, Tab. 4.2). However, there is no significant difference between the DA of the osteopenic group as compared to the osteoporotic group's DA ($p = 0.2332$) and the healthy group's DA ($p > 0.9999$; Fig. 4.3 C).

The most commonly present trabecular thickness of the osteoporotic group is around the mid-range thickness of 165.26 µm with 16.24 % (Fig. 4.4 A). The osteopenic group has roughly the same distribution when it comes to the trabecular thickness with the same mid-range thickness as the osteoporotic group with values of 15.90 % (Fig. 4.4 B). The most commonly present trabecular thickness of the healthy group is with 13.71 % at the mid-range thickness of 231.36 µm (Fig. 4.4 C). Interestingly, the mean trabecular thickness (Tb.Th.) of the osteopenic group is significantly different to the healthy group ($p = 0.0081$), but the Tb.Th. of the osteoporotic group compared to the Tb.Th. of the healthy group is not significantly different ($p = 0.0605$; Tab. 4.2). Moreover, the Tb.Th. of the osteoporotic group is similar to the Tb.Th. of the osteopenic group ($p > 0.9999$). Looking more closely at the distribution of the trabecular thickness, statistical testing was performed in the mid-range thickness of 33 µm to 600 µm (Fig. 4.4). The osteoporotic samples have a significantly higher percentage of trabeculae in the mid-range thickness of 132 µm and 165 µm as compared to the healthy samples ($p = 0.0381$; $p = 0.0157$). At the mid-range thickness of 495 µm, the healthy group has a significantly higher percentage than the osteoporotic samples ($p = 0.0361$). The osteopenic samples have a significantly higher percentage of trabeculae with a mid-range thickness 99 µm ($p = 0.0157$), 132 µm ($p = 0.0104$), 165 µm ($p = 0.0110$) and 198 µm ($p = 0.0381$) as compared to the healthy samples. The percentage of trabeculae of the healthy samples is significantly higher at a mid-range thickness of 330 µm ($p = 0.0129$), 363 µm ($p = 0.0053$), 396 µm ($p = 0.0039$), 429 µm ($p = 0.0119$) and 462 µm ($p = 0.0126$). The thickness of the trabeculae of the osteoporotic samples and the osteopenic samples are similar over the whole range ($p > 0.9999$).

Looking at the representative trabecular thickness distributions of the samples from the different groups, it is visible that the healthy group has a wider range of trabecular thickness and thus lower percent values per thickness (Fig. 4.4 D). The osteoporotic and the osteopenic sample have a smaller range of trabecular thickness as compared to the healthy sample, as no trabeculae with thickness above 700 µm were present (Fig. 4.4 D).

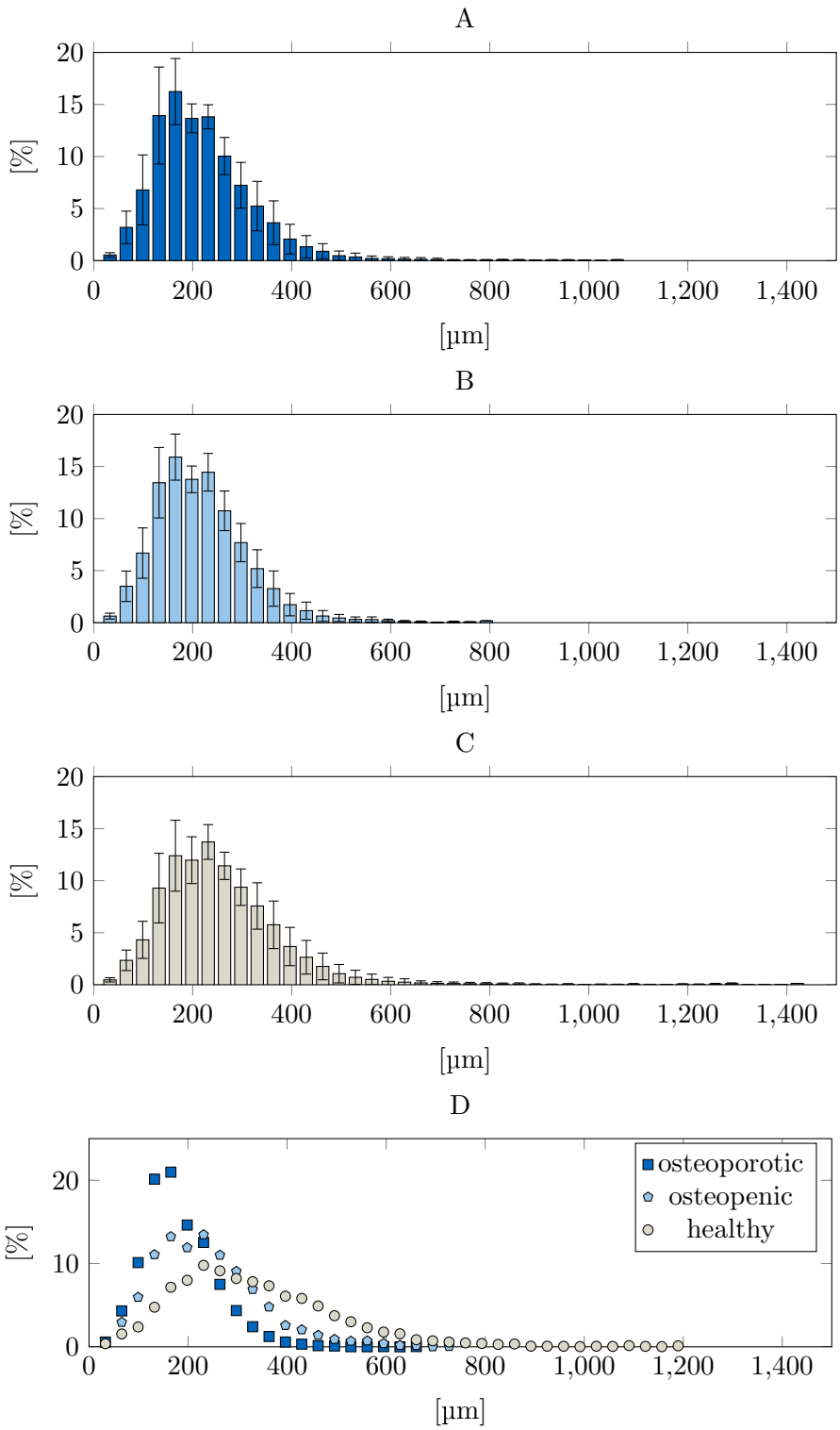

Figure 4.4.: Trabecular thickness distribution of osteoporotic (A), osteopenic (B) and healthy samples (C) as mean±standard deviation. For better comparison, the mean of one representative distribution per group is also shown as overlay (D). Dark blue: osteoporotic, light blue: osteopenic, gray: healthy.

4.1.2. Raman spectroscopy

For the Raman spectroscopy analysis, a total of 18 samples was tested. The sex distribution can be seen in Tab. 4.3. One representative spectrum per group is shown in Fig. 4.5 for hydroxyapatite (HA) and lipid compositions of the bone. Because of the software processing, it was possible to divide the bone spectrum into the mineral spectrum (HA spectrum) and the matrix spectrum (lipid spectrum). The measuring area and the corresponding heat map of the HA spectrum and the lipid spectrum is shown (Fig. 4.5). Looking at the heat map, the blue area indicates a higher amount of HA and the red area indicates more lipids/collagen. The heat map of the healthy sample shows that most of the area is dominated by HA (Fig. 4.5 C).

Table 4.3.: Sex distribution in the single groups of the Raman spectroscopy analysis

	osteoporotic	osteopenic	healthy	treated
female	3	5	3	2
male	2	1	2	0

Typical bone mineral and matrix spectrum bands are the phosphate band at $\approx 960\,\mathrm{cm}^{-1}$, which is characteristic for carbonated apatite, the B-type carbonate band at $\approx 1070\,\mathrm{cm}^{-1}$, the phosphate band at $\approx 1079\,\mathrm{cm}^{-1}$, the CH_2 deformation band at $\approx 1450\,\mathrm{cm}^{-1}$, the proline band at $\approx 868\,\mathrm{cm}^{-1}$, the amide III band at $\approx 1300\,\mathrm{cm}^{-1}$, the CH_2 deformation band of lipids at $\approx 1440\,\mathrm{cm}^{-1}$ and the amide I band at $\approx 1656\,\mathrm{cm}^{-1}$. All typical peaks for bone are present in the samples of the three different groups. However, all osteoporotic samples show no peak at the band at $1495\,\mathrm{cm}^{-1}$ and moreover, some samples of the osteopenic group have no peak at the band at $1495\,\mathrm{cm}^{-1}$ (Fig. 4.5).

Looking at the absolute peak heights of the bands at $868\,\mathrm{cm}^{-1}$, $1079\,\mathrm{cm}^{-1}$, $1300\,\mathrm{cm}^{-1}$, $1440\,\mathrm{cm}^{-1}$ and $1656\,\mathrm{cm}^{-1}$ of the lipid spectrum, there is a tendency to lower values of the osteoporotic group as compared to the healthy and osteopenic group (Fig. 4.6 A-D, F). The exact p-values are listed in Table A.3 (in the Appendix). The absolute peak height of the band at $1495\,\mathrm{cm}^{-1}$ is significantly higher in the healthy group as compared to the osteoporotic group ($p = 0.0348$) and the osteopenic group ($p = 0.0351$; Fig. 4.6 E). The absolute peak height of the osteoporotic group and the osteopenic group is similar ($p > 0.9999$; Fig. 4.6 E). The absolute peak heights of the bands at $960\,\mathrm{cm}^{-1}$, $1070\,\mathrm{cm}^{-1}$ and $1450\,\mathrm{cm}^{-1}$ of the HA spectrum are similar between the different groups, too (Fig. 4.7 A-C, Tab. A.4). In contrast, the osteoporotic group shows significantly lower absolute peak heights of the band at $1495\,\mathrm{cm}^{-1}$ as compared to the healthy group ($p = 0.0194$; Fig. 4.7 D).

The relative peak heights of the lipid spectrum bands to the bone mineral band ($960\,\mathrm{cm}^{-1}$) of the HA spectrum are similar between the three groups (Fig. 4.8, Tab. A.5). The relative peak height of the band at $1495\,\mathrm{cm}^{-1}$ of the lipid spectrum has a tendency to lower values in the osteoporotic group as compared to the healthy group ($p = 0.1887$; Fig. 4.8 E; Tab. A.5). The relative peak height of the band $1450\,\mathrm{cm}^{-1}$ of the HA spectrum to the bone mineral band $960\,\mathrm{cm}^{-1}$ of the HA spectrum is similar between the three group (Fig. 4.9 B; Tab. A.6). There is a tendency to higher values of the osteoporotic group as compared to the healthy group in the relative peak height of the band at $1070\,\mathrm{cm}^{-1}$ to the band at $960\,\mathrm{cm}^{-1}$ of the HA spectrum ($p = 0.1185$; Fig. 4.9 A). Similarly, there is a tendency to lower values of the

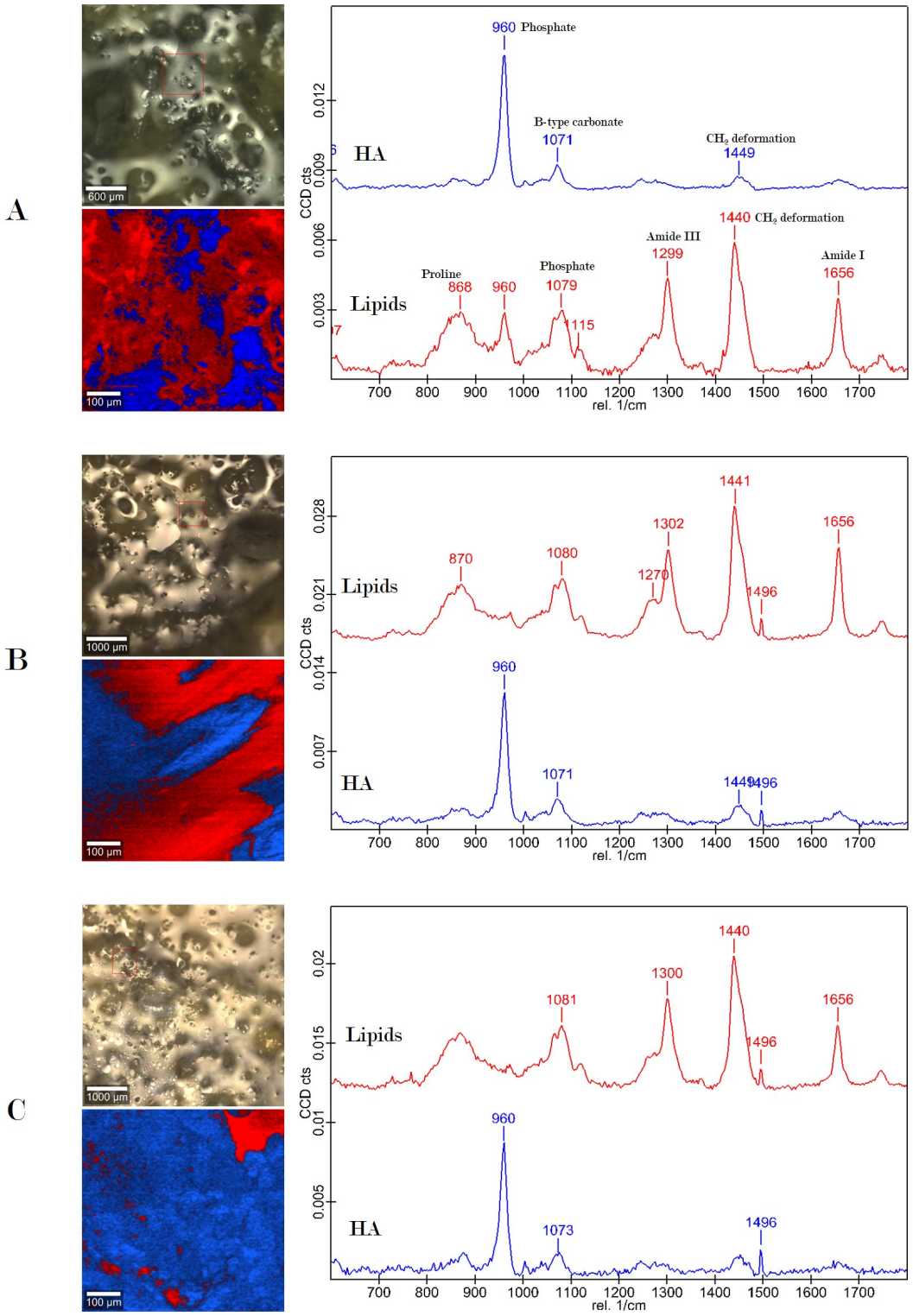

Figure 4.5.: Representative Raman spectra from an osteoporotic sample (A), an osteopenic sample (B) and of a healthy sample (C). Microscopic pictures of the testing area and heat maps of the scanned area with hydroxyapatite (HA) (blue) and collagen type I (red). Depending on which bone matrix component is predominantly present, the heat map either shows red or blue areas. HA spectrum: blue line, lipid spectrum: red line.

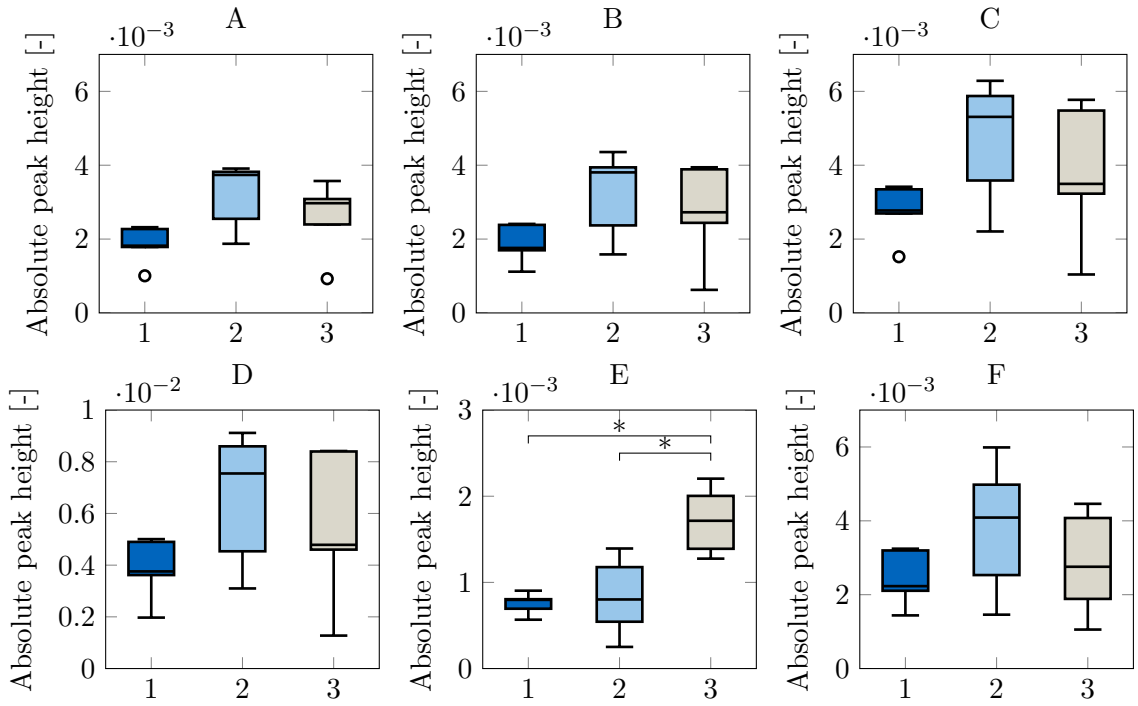

Figure 4.6.: Absolute peak heights of the bands at 868 cm^{-1} (A), 1079 cm^{-1} (B), 1300 cm^{-1} (C), 1440 cm^{-1} (D), 1495 cm^{-1} (E), 1656 cm^{-1} (F) in the lipid spectrum of the osteoporotic (1), osteopenic (2) and healthy group (3). Box plot with 25 % and 75 % percentile with median plus maximum and minimum values. Significant values are marked as described in Tab. 3.8.

osteoporotic group as compared to the healthy group in the relative peak height of the band at 1495 cm^{-1} to the band at 960 cm^{-1} of the HA spectrum ($p = 0.0852$; Fig. 4.9 C).

The relative peak height of the bands at 868 cm^{-1} and 1300 cm^{-1} to the amide I band at 1656 cm^{-1} of the lipid spectrum are similar for all groups (Fig. 4.10 A, C; Tab. A.7). There is a tendency to lower values of the osteoporotic group as compared to the healthy group in the relative peak height of the band at 1079 cm^{-1} and 1440 cm^{-1} to the amide I band at 1655 cm^{-1} of the lipid spectrum ($p = 0.3798$, $p = 0.3327$; Fig. 4.10 B, D). For the relative peak height of the band at 1495 cm^{-1} of the lipid spectrum to the amide I band at 1656 cm^{-1}, the tendency to lower values is also visible in the osteoporotic group as compared to the healthy group ($p = 0.2187$; Fig. 4.10 E). The relative peak height for the before-mentioned bands is significantly higher for the healthy group as compared to the osteopenic group ($p = 0.0470$; Fig. 4.10 E).

The relative peak heights of the bands at 1070 cm^{-1} and 1450 cm^{-1} of the HA spectrum to the amide I band at 1656 cm^{-1} of the lipid spectrum are similar between all three groups (Fig. 4.11 A, B; Tab. A.8). The relative peak height of the band at 1495 cm^{-1} of the HA spectrum to the amide I band of the lipid spectrum is significantly higher for the healthy group as compared to the osteoporotic group ($p = 0.0104$; Fig. 4.11 C).

The principal component analysis (PCA) shows bone mineral apatite with the band at 960 cm^{-1}

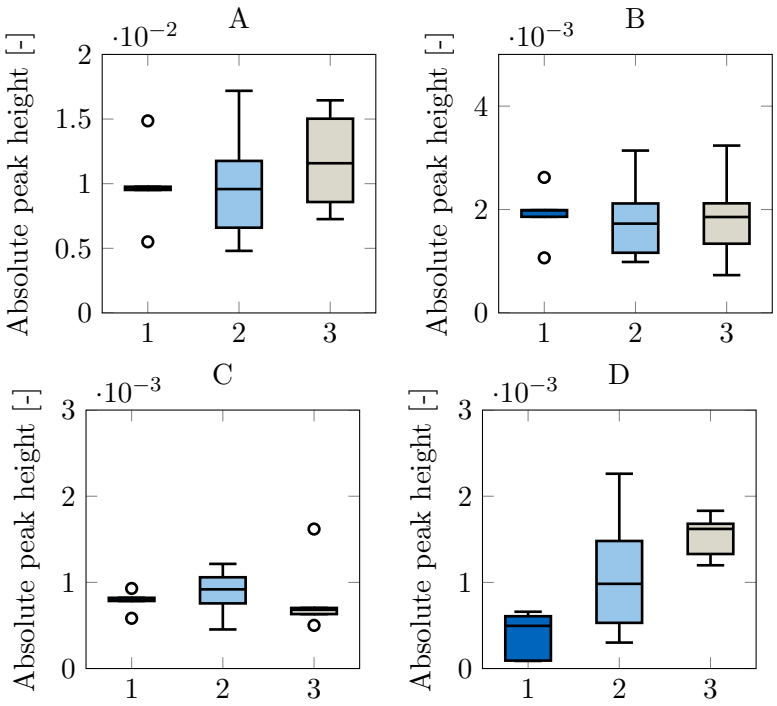

Figure 4.7.: Absolute peak heights of the bands at 960 cm^{-1} (A), 1070 cm^{-1} (B), 1450 cm^{-1} (C), 1495 cm^{-1} (D) in the HA spectrum of the osteoporotic (1), osteopenic (2) and healthy group (3). Box-plot with 25 % and 75 % percentile with median plus maximal and minimal values. Outliers are marked by a circle.

of the HA spectrum (Fig. 4.12) as main component with the highest variability inside the measurement domain of all samples (PC-1). The single patients in the groups show a high variance of the variability of PC-1 (Fig. 4.12 A-C). The three groups in turn show a similar behavior in the variability ($p > 0.9999$; Fig. 4.12). The crystallinity of the bone mineral apatite is calculated with the full width half height method of the bands between 930 cm^{-1} to 980 cm^{-1} (Fig. 4.13). There is a tendency to higher values in the osteoporotic group as compared to the healthy group ($p = 0.6758$; Fig. 4.13).

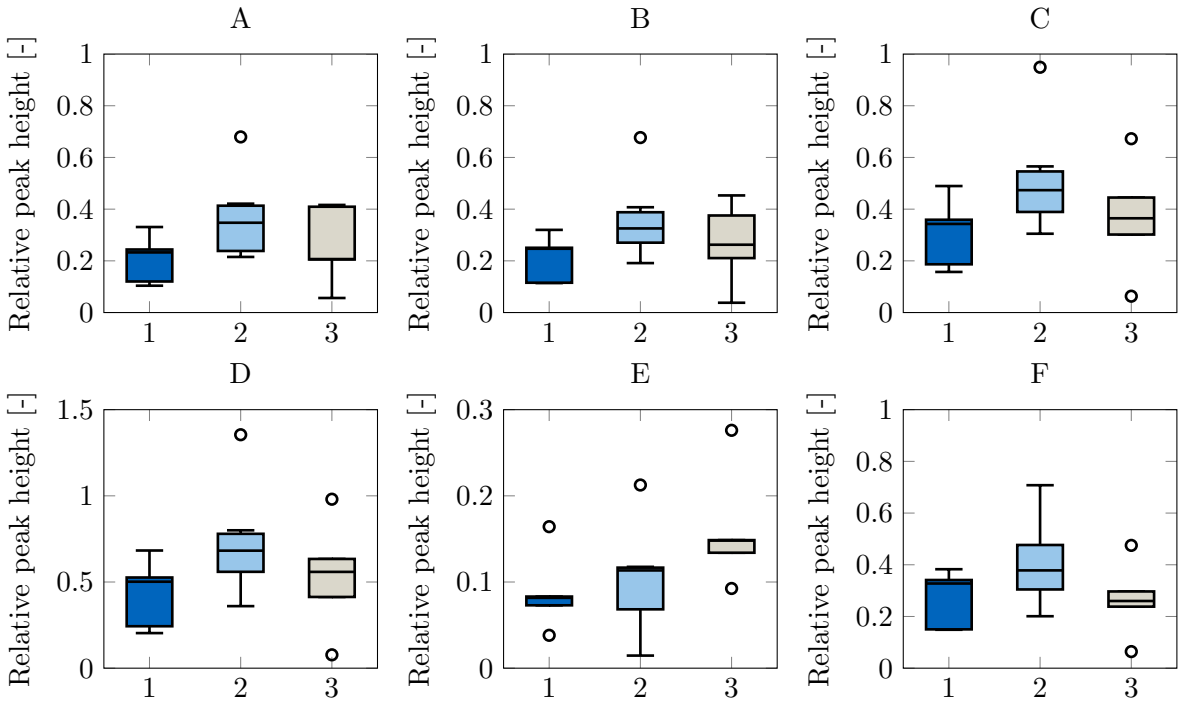

Figure 4.8.: Relative peak heights of the bands at 868 cm^{-1} (A), 1079 cm^{-1} (B), 1300 cm^{-1} (C), 1440 cm^{-1} (D), 1495 cm^{-1} (E), 1656 cm^{-1} (F) in the lipid spectrum to the bone mineral band at 960 cm^{-1} in the HA spectrum of the osteoporotic (1), osteopenic (2) and healthy group (3). Box plot with 25 % and 75 % percentile with median plus maximum and minimum values. Outliers are marked by a circle.

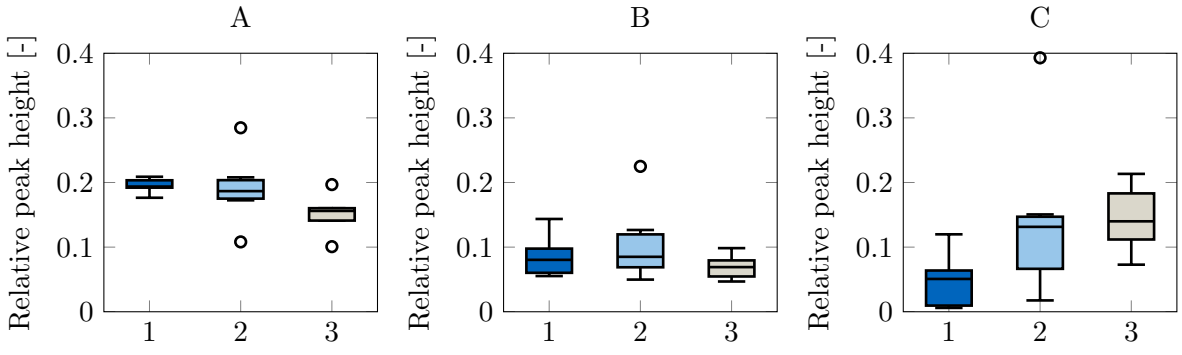

Figure 4.9.: Relative peak heights of the bands at 1070 cm^{-1} (A), 1450 cm^{-1} (B), 1495 cm^{-1} (C) in the HA spectrum to the bone mineral band at 960 cm^{-1}, in the HA spectrum of the osteoporotic (1), osteopenic (2) and healthy group (3). Box plot with 25 % and 75 % percentile with median plus maximum and minimum values. Outliers are marked by a circle.

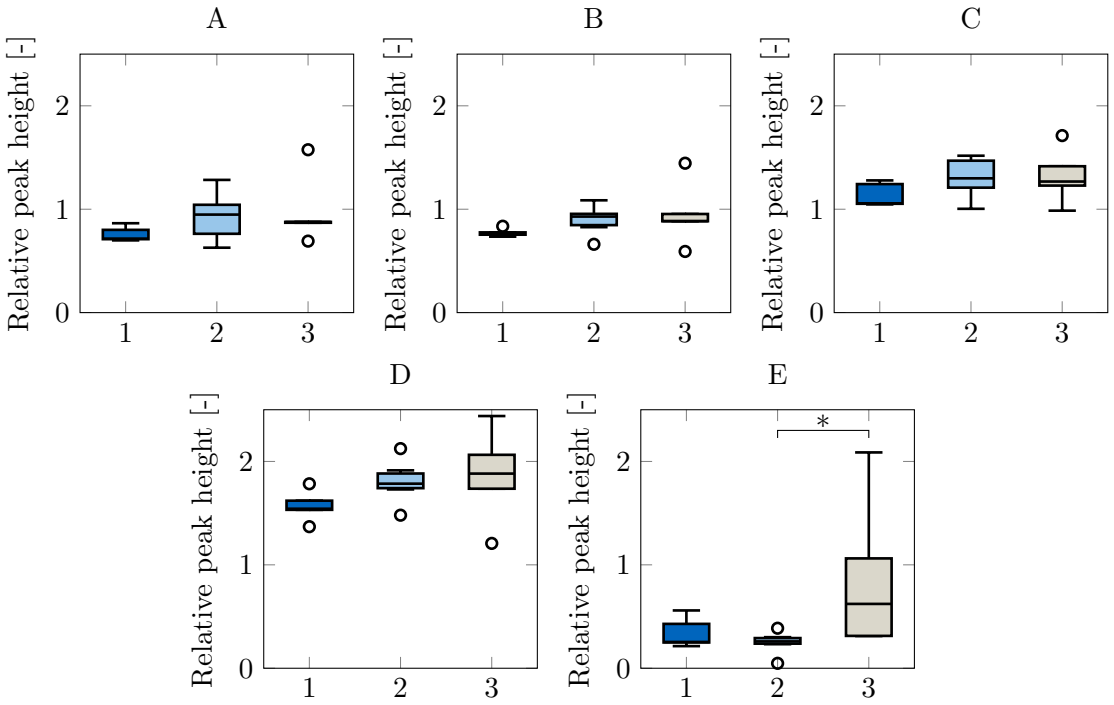

Figure 4.10.: Relative peak heights of the bands at 868 cm^{-1} (A), 1079 cm^{-1} (B), 1300 cm^{-1} (C), 1440 cm^{-1} (D), 1495 cm^{-1} (E) in the lipid spectrum to amide I (1656 cm^{-1}) of the osteoporotic (1), osteopenic (2) and healthy group (3). Box plot with 25 % and 75 % percentile with median plus maximum and minimum values. Significant values are marked as described in Tab. 3.8. Outliers are marked by a circle.

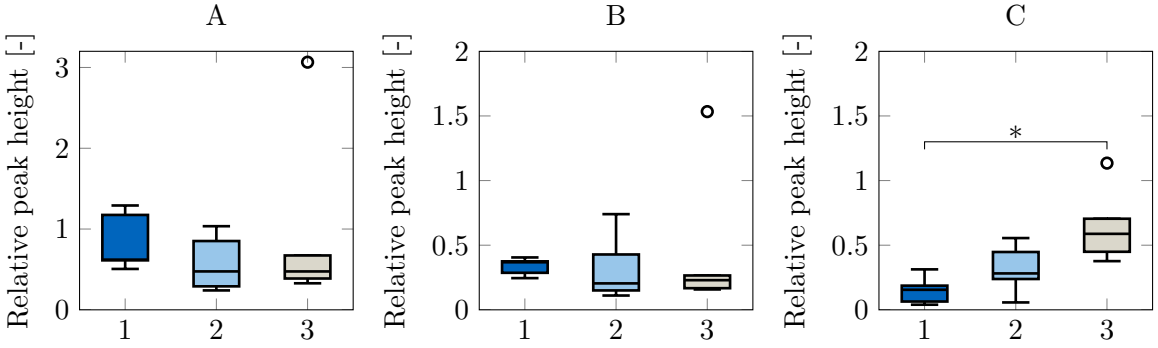

Figure 4.11.: Relative peak heights of the bands at 1070 cm^{-1} (A), 1450 cm^{-1} (B), 1495 cm^{-1} (C) in the HA spectrum to amide I 1656 cm^{-1} of the osteoporotic (1), osteopenic (2) and healthy group (3). Box plot with 25 % and 75 % percentile with median plus maximum and minimum values. Significant values are marked as described in Tab. 3.8. Outliers are marked by a circle.

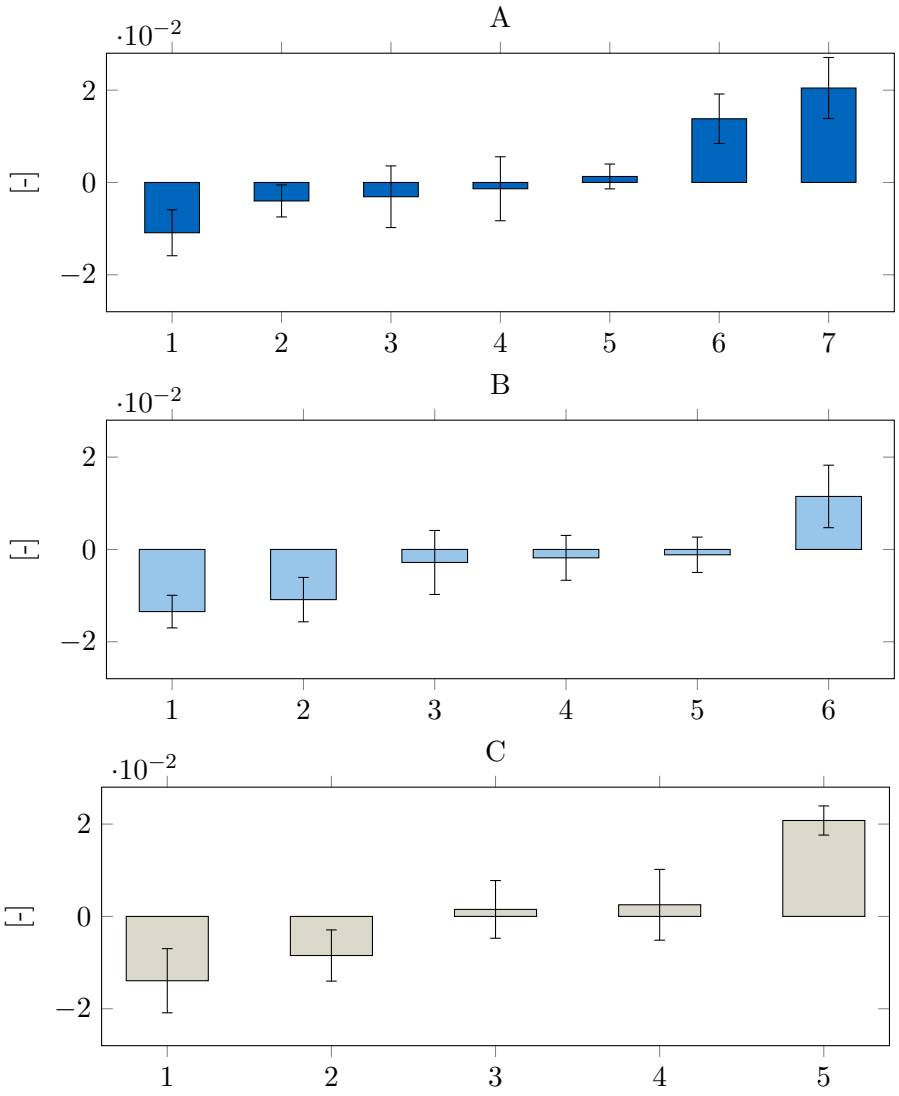

Figure 4.12.: PCA analysis of the bone mineral (PC-1) of the single samples in the osteoporotic (A), the osteopenic (B) and the healthy group (C). Box plot with 25 % and 75 % percentile with median plus maximum and minimum values.

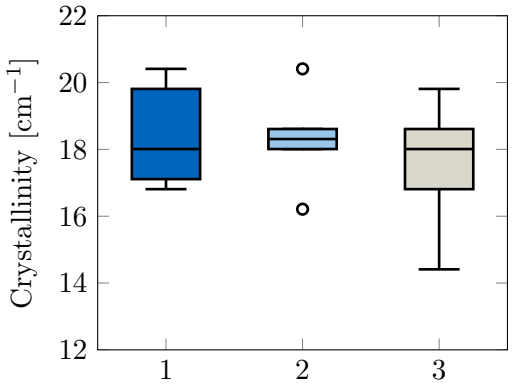

Figure 4.13.: Crystallinity of the bone mineral (960 cm^{-1}) for the three different groups. 1: osteoporotic; 2: osteopenic; 3: healthy. Box plot with 25 % and 75 % percentile with median plus maximum and minimum values.

4.1.3. Biomechanical testing

In this section, the osteoporotic and osteopenic samples were pooled to the new classification "o/o group" (N = 8). Otherwise, there would have been only one osteoporotic sample. Twenty-one healthy samples were used as control group (healthy group).

Table 4.4.: Sex distribution in the single groups of the biomechanical testing analysis

	o/o	healthy
female	7	13
male	1	8

The Young's modulus of the samples in the two groups was found to be similar (p = 0.3932; Fig. 4.14 A). For the healthy group, the median Young's modulus was 541.8 N/mm^2 (25 % percentile: 287.4 N/mm^2; 75 % percentile: 912.4 N/mm^2). For the o/o group, the median Young's modulus was 561.1 N/mm^2 (25 % percentile: 155.1 N/mm^2; 75 % percentile: 631.6 N/mm^2; Fig. 4.14 A). Looking at the healthy group, the absolute maximum force at load-to-failure (F_{max}) was significantly higher as compared to the o/o group (p = 0.0036; Fig. 4.14 C). The median of the healthy group (844.4 N; 25 % percentile: 634.4 N; 75 % percentile: 1195 N) was more than twice as high as the one of the o/o group (409.7 N; 25 % percentile: 347 N; 75 % percentile: 542.2 N) (Fig. 4.14 C).

The geometry of some of the bone slices could not fulfill the required size as described in Chapter 3.2.3. For a more comparable result, F_{max} was calculated per contact face (F_{max} per area). The needed force for the load-to-failure was 7.128 N/mm^2 (25 % percentile: 5.544 N/mm^2; 75 % percentile: 9.341 N/mm^2) for the o/o group and for the healthy group, the value was 12.95 N/mm^2 (25 % percentile: 9.12 N/mm^2; 75 % percentile: 15.32 N/mm^2) (Fig. 4.14 D). The F_{max} per area value of the healthy group was significantly higher as compared to the value of the o/o group (p = 0.0043).

The distribution of the strain at F_{max} in the o/o group was more widespread than in the healthy group. Nevertheless, the strain of the o/o group (0.05919; 25 % percentile: 0.050 66;

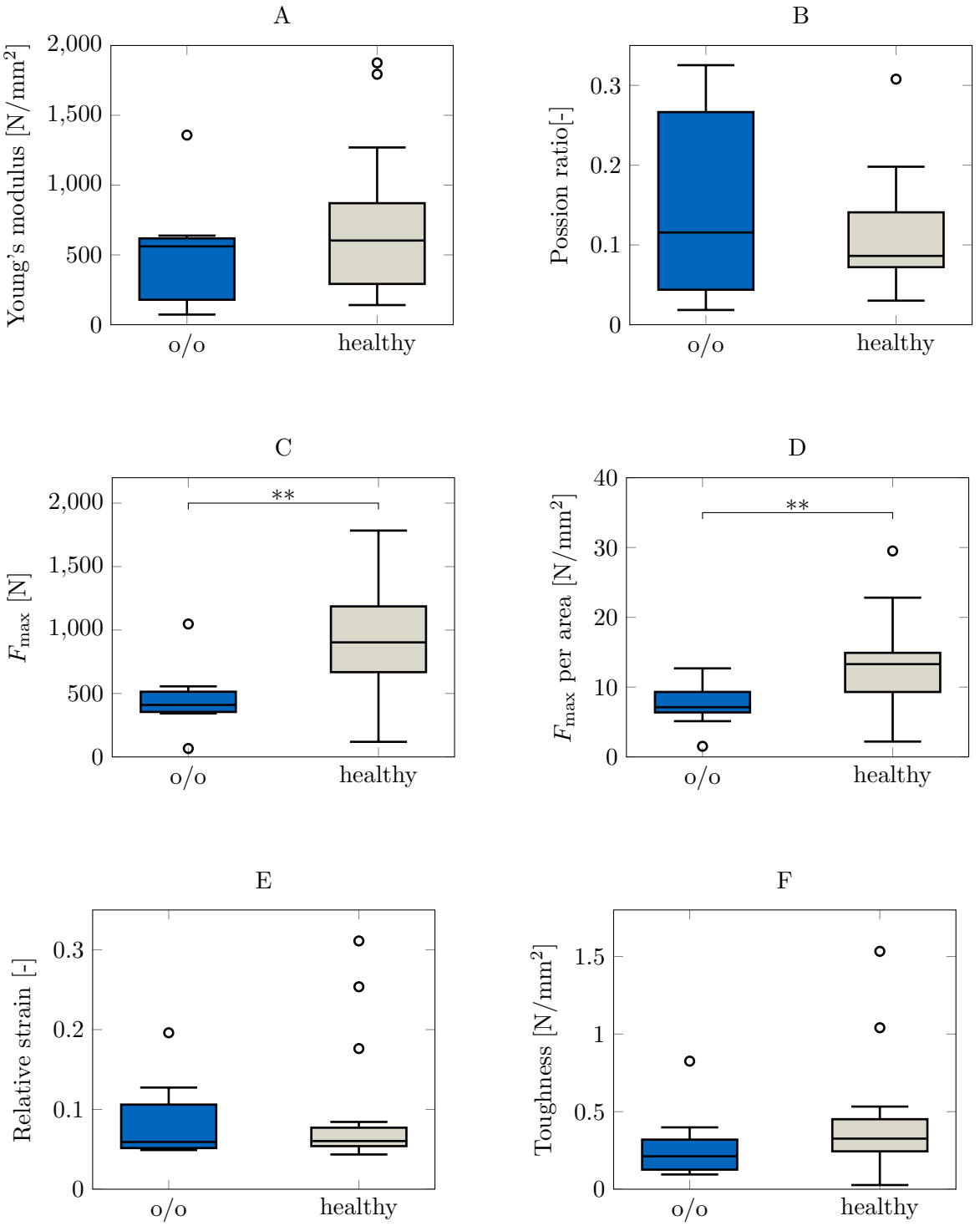

Figure 4.14.: Biomechanical results of Young's modulus (A), Poisson ratio (B), F_{max} (C), F_{max} per area (D), relative strain at F_{max} (E) and toughness (F) of the healthy (gray) and the o/o samples (blue). o/o: mixed samples from the osteoporotic and osteopenic groups. Median with 25 % and 75 % percentile plus maximum and minimum values and outliers (marked by a circle). Significance values are marked as described in Tab. 3.8 .

75 % percentile: 0.1203) was similar to the strain of the healthy group (0.06003; 25 % percentile: 0.053 56; 75 % percentile: 0.078 64) (p = 0.9086; Fig. 4.14 E). In this study, toughness is constituted by the area below the curve in the stress-strain plot starting at the minimum of the 5th cycle until F_{max} is reached (Fig. 4.14 F). The toughness of the healthy group is higher than the toughness of the o/o group (0.3142 N/mm^2 vs. 0.2124 N/mm^2), but not significantly (p = 0.2188; Fig. 4.14 F).

Looking at the Poisson ratio, no difference was found between the two groups (p = 0.9714; Fig. 4.14 B). The interquartile range of the o/o group is so large that it overlaps completely with the healthy group values. Moreover, the medians are similar (healthy group 0.08627 vs. o/o group 0.1156) (Fig. 4.14 B). For the calculation of the Poisson ratio, not all samples could be used so that the number of samples had to be reduced to N = 6 in the o/o group and to N = 16 in the healthy group.

4.2. Scaffold characterization

In the following sections, the results of the structural analysis (Section 4.2.1), the cytotoxicity and proliferation (Section 4.2.2) and the cell adhesion capabilities (Section 4.2.3 - 4.2.4) are described for the scaffolds with low fibroin content (LF), the ones with high fibroin content (HF) and the HF surface-treated (HF+) scaffold.

4.2.1. Structural analysis

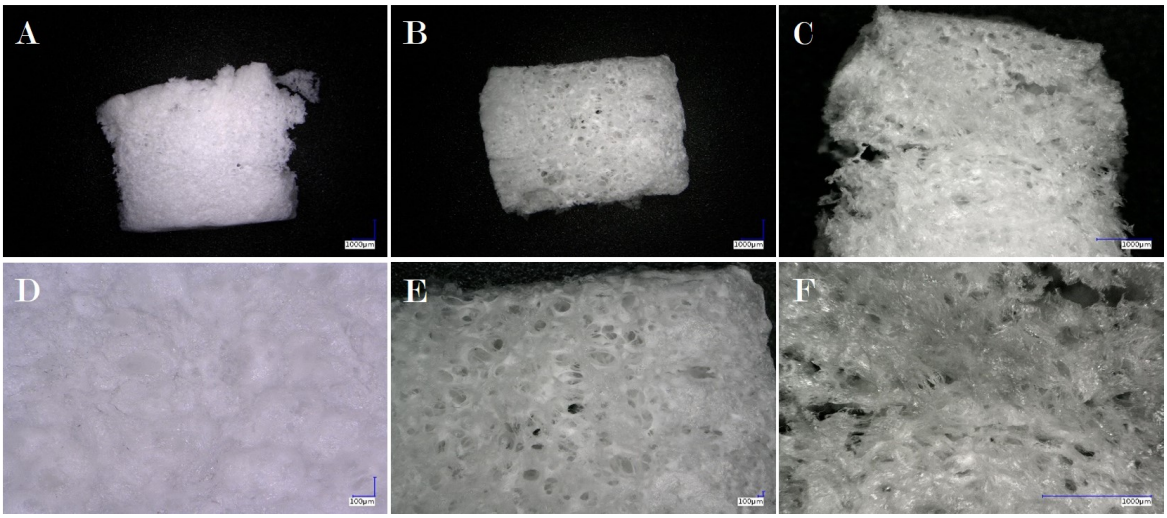

Figure 4.15.: Microscopic pictures of the produced scaffolds LF (A, D), HF+ (B, E) and HF (C, F). The images are shown as overview (A, B, C) and higher magnification pictures (D, E, F).

The structural analysis of the produced scaffolds showed that the LF scaffold was more compact and closed than the HF+ and HF scaffolds (Fig. 4.15). This was also visible in the SEM (Fig. 4.18 A - F). There was no optical difference between the HF+ and HF scaffold (Fig. 4.15).

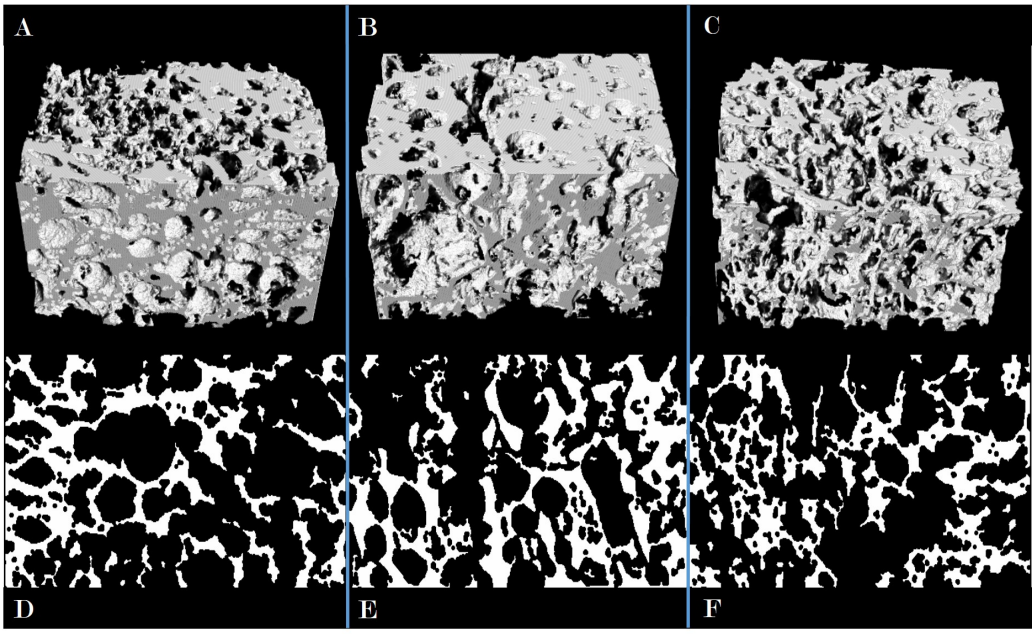

Figure 4.16.: Micro-CT reconstruction of the scaffolds with low fibroin content (LF) (A), with surface-treated high fibroin content (HF+) (B), with high fibroin content (HF) (C) and a representative slide through each scaffold showing the pore distribution of the LF (D), HF+ (E) and HF (F) scaffolds.

All three scaffold groups showed different pore sizes in the macroscopic view (Fig. 4.15 A, B, C) and also in the higher magnification pictures (Fig. 4.15 D, E, F). Looking closer with the micro-CT, the different pore sizes could also be seen inside the scaffolds (Fig. 4.16). In the reconstruction of the HF scaffold, the thickness of the material around the pores looked thinner than of the other scaffolds (Fig. 4.16 D-F).

Table 4.5.: Results micro-CT analysis of the scaffolds

parameter	LF	HF+	HF
Total Porosity [%]	69.01	68.12	73.04
Percent object volume [%]	30.99	31.88	26.96
Fractal dimension (FD)	2.7287	2.7408	2.7261
Structure thickness [µm]	72.51	87.99	58.06
Object surface/volume ratio [1/µm]	0.05	0.05	0.06
Degree of anisotropy (DA)	0.43233	0.45996	0.44729

Looking at the calculated values of the structure thickness, the HF scaffold showed the lowest value (58.06 µm), followed by the LF scaffold with 72.51 µm and the HF+ scaffold had the highest thickness with 87.99 µm (Tab. 4.5). The calculation of the porosity showed that the porosity of the LF scaffold (69.01 %) and HF+ scaffold (68.12 %) were nearly the same, only the HF scaffold porosity was higher (73.04 %) (Tab. 4.5). The percent object volume represents the proportion of the VOI occupied by binarised solid objects. This means that in case of the HF scaffold, about 1/4 of the VOI was solid material, while for the other two scaffolds

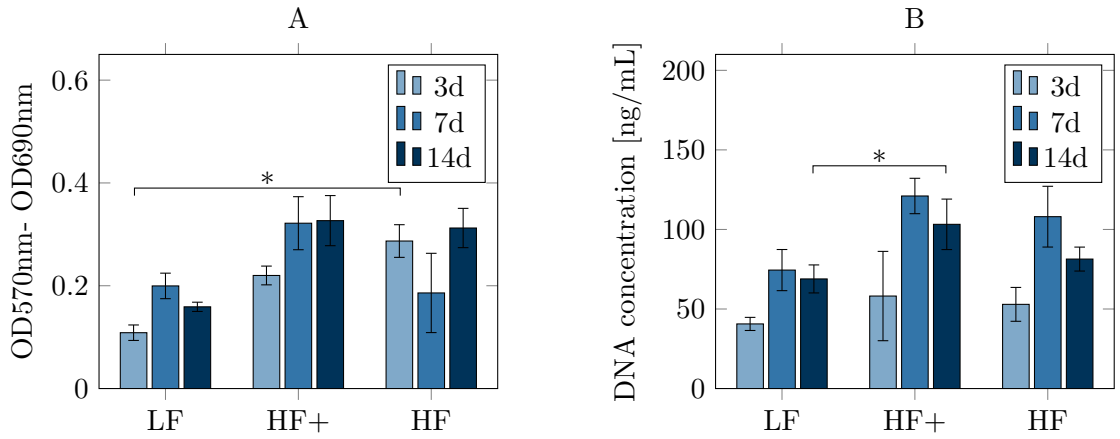

Figure 4.17.: Cytotoxicity (A) and proliferation (B) of the low fibroin (LF), the surface-treated high fibroin (HF+) and the high fibroin (HF) scaffolds after the cultivation time of 3 d, 7 d and 14 d. Mean and standard deviation are shown. Significant values are marked as described in Tab. 3.8.

types, it was roughly 1/3 (Tab. 4.5). The degree of anisotropy was nearly the same for all three groups and the scaffolds were more isotropic than anisotropic. The fractal dimension was similar for all scaffolds. Also, the object surface/volume ratio was very similar for all scaffold types (Tab. 4.5).

4.2.2. Cytotoxicity and proliferation

Cytotoxicity and proliferation were evaluated at 3 d, 7 d and 14 d. With both methods, the LF scaffolds initially showed lower values in comparison to the HF scaffolds during the whole observation time (Fig. 4.17). From 7 d ongoing, the cytotoxicity decreased significantly for the LF scaffold as compared to the cytotoxicity at 3 d ($p = 0.0219$, Fig. 4.17 A). The HF+ and HF scaffolds were not as cytotoxic as the LF scaffolds, but their cytotoxicity also decreased after 7 d (Fig. 4.17 A). The HF scaffold's cytotoxicity was significantly lower as compared to the LF scaffold's at 3 d ($p = 0.0219$, Fig. 4.17 A). The absolute DNA content increased in all scaffold groups (Fig. 4.17 B). The initial DNA concentration was similar for all scaffold types after 3 d. Over the cultivation time, the DNA concentration in both HF type scaffolds was almost twice as high as the DNA concentration at 3 d (Fig. 4.17 B). After 14 d, the DNA content of the HF+ scaffolds was significantly higher as compared to the LF group ($p = 0.0338$; Fig. 4.17 B).

4.2.3. Cell adhesion

The cell adhesion was observed by means of SEM. There was no apparent difference in the cell attachment at any analyzed point in time for the LF, HF and HF+ scaffold (Fig. 4.18 G - I). From day 7 to day 14, the attached cells per scaffold extended to a nearly closed cell layers on all three scaffold types (Fig. 4.18 J - L).

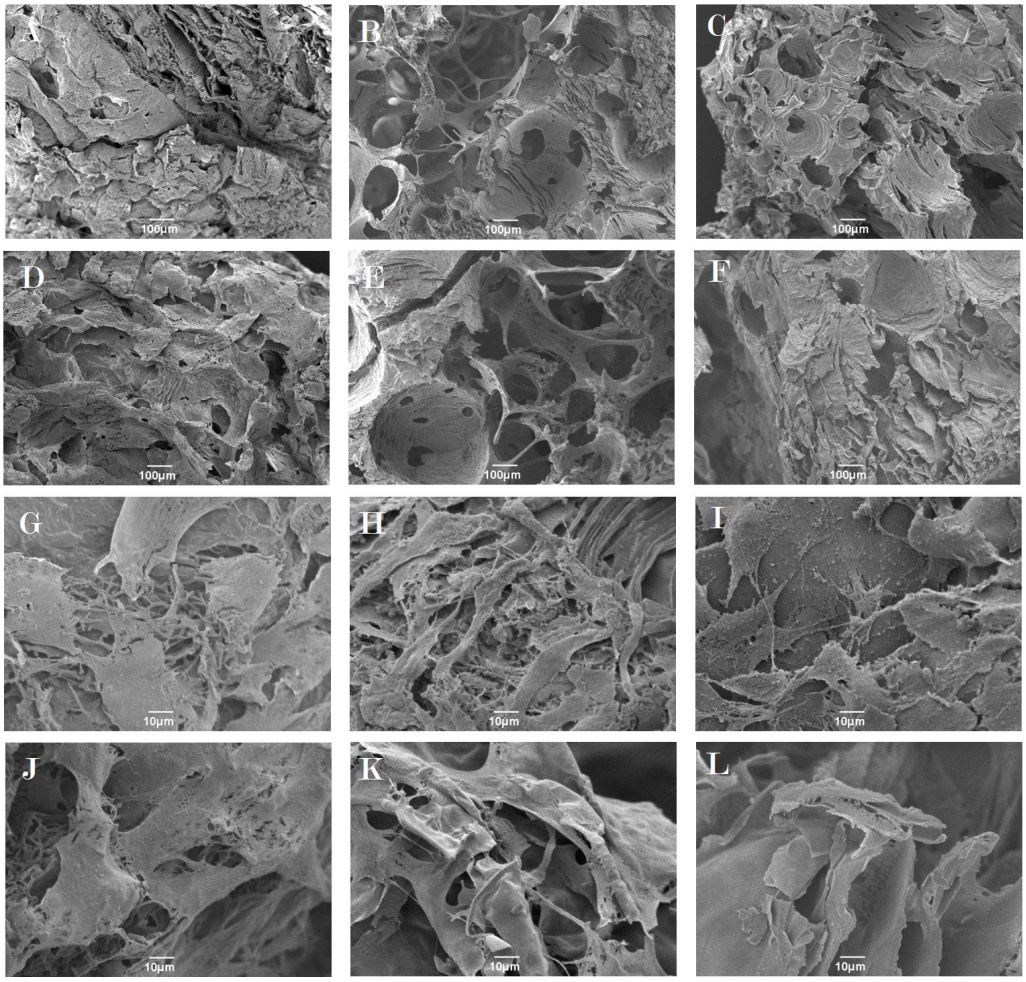

Figure 4.18.: SEM pictures of the low fibroin (LF) (A, D, G, J), the surface-treated high fibroin (HF+) (B, E, H, K) and the high fibroin (HF) (C, F, I, L) scaffolds. Unseeded in medium for 7d (A, B, C) and 14d (D, E; F), seeded after a cultivation time of 7d (G, H, I) and after 14d (J, K, L) with a magnification of 1000x.

4.2.4. Cell morphology and distribution on cell seeded scaffolds

Confocal images were taken to look at the cell morphology and cell distribution on the seeded scaffolds (described in Section 3.4.1). Images for both cultivation times (7d and 14d) showed cells spreading over the complete scaffold (Fig. 4.19). For all types of scaffolds investigated, the cell distribution is similar after 7d of cultivation (Fig. 4.19 A, C, E) and after 14d of cultivation (Fig. 4.19 B, D, F).

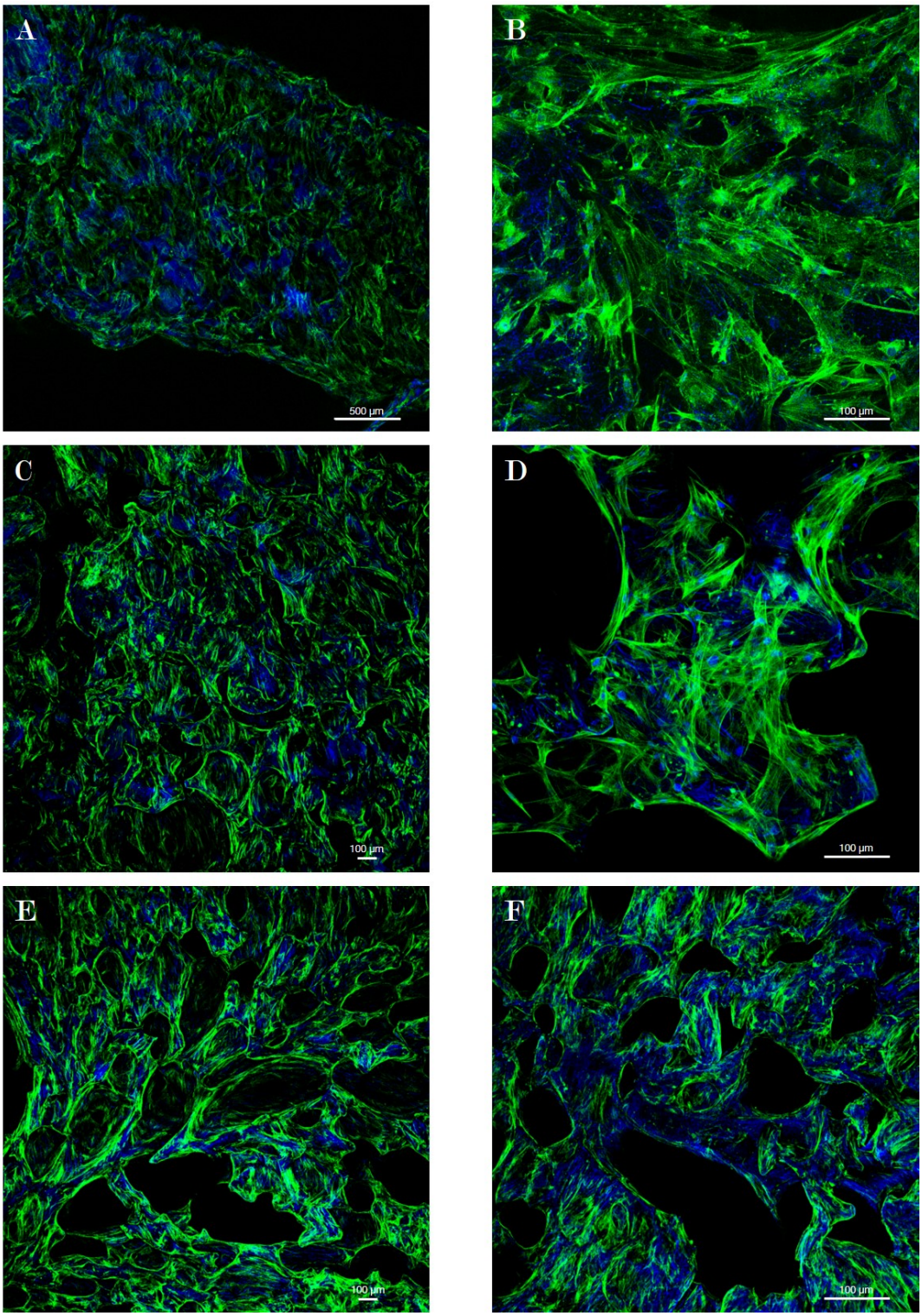

Figure 4.19.: Confocal images of the low fibroin (LF) (A, B), the surface-treated high fibroin (HF+) (C, D) and the high fibroin (HF) (E, F) scaffolds after 7d (A, C, E) and after 14d (B, D, F) of cultivation time. Nucleus: DAPI (blue); cytoskeleton: Oregon Green 488 Phalloidin (green).

4.3. Expression of miR-100-5p

The miR-100-5p expression of isolated osteoblasts was determined as potential drug therapy approach (see Section 4.3.1). Additionally, the results of the transfection on the HF scaffold are shown in Section 4.3.2.

4.3.1. Expression in osteoblasts

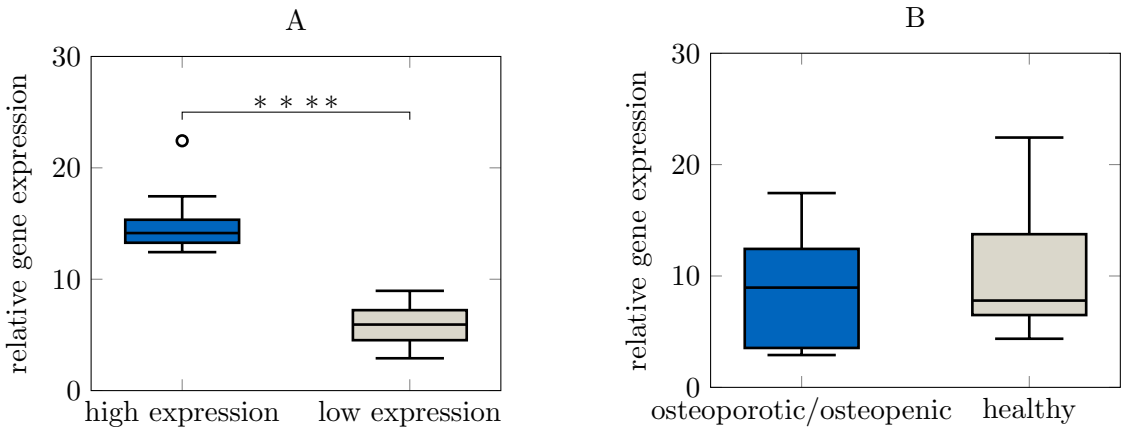

Figure 4.20.: Relative gene expression of miR-100-5p in healthy and osteoporotic osteoblasts. Grouping according to expression level (A) and BMD of the used samples (B). Median with 25 % and 75 % percentile plus minimum and maximum values. Outliers are shown by a circle. Values are normalized to SNORD96a and expressed as $2^{\Delta C_T}$. Significant values are marked as described in Tab. 3.8.

Looking at the gene expression level of miR 100-5p in the osteoblasts, these could be divided into two groups: high level and low level expression. The median of the relative low level expression is 5.93 (25 % percentile: 2.903; 75 % percentile: 8.958) and the median of the relative high level expression is 14.15 (25 % percentile: 12.73; 75 % percentile: 16.74) (Fig. 4.20 A). When grouping according to the calculated BMD of the bone slices (Section 4.1.1), the expression level of the two groups i.e., osteoporotic/osteopenic and healthy were similar ($p = 0.5663$) regarding their relative gene expression (8.958 vs. 7.793; Fig. 4.20 B). The median of the o/o group is 8.958 (25 % percentile: 2.903; 75 % percentile: 14.94). In turn, the median of the relative gene expression of the healthy group is 7.793 (25 % percentile: 4.366; 75 % percentile: 14.15).

4.3.2. Effect of miR-100-5p inhibitor transfection on miR-100-5p expression

The inhibition effect was analyzed 1 d, 3 d and 7 d after transfection. The various transfection controls and the transfection reagent had no influence on the miR-100-5p expression (Fig. A.2, A.1). The negative control showed that the result is specific for the inhibitor, because the transfected cells with the negative control showed a similar expression as the untransfected cells (Fig. A.1). The positive control showed a higher expression level than the mimic alone for

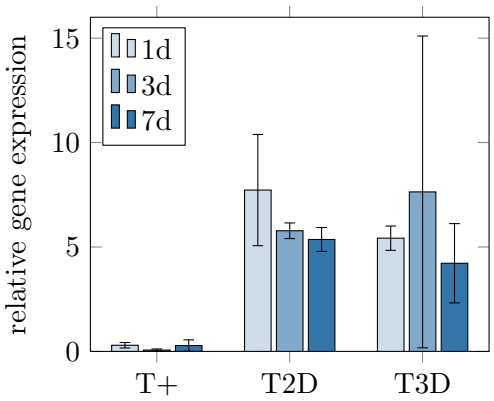

Figure 4.21.: MiR-100-5p expression levels after miR-100-5p inhibition of the transfected cells (T+), untransfected cell monolayer (T2D) and untransfected cells in 3D (T3D) after cultivation of 1d, 3d and 7d. Mean values and standard deviation are shown. Values are normalized to SNORD96a and expressed as $2^{\Delta C_{\mathrm{T}}}$.

all time points. This showed that the transfection procedure had worked. It could also clearly be seen that the miR-1 gene was not expressed in the other groups (Fig. A.2). The miR-100-5p relative gene expression decreased over time for the 2D untransfected cells (Fig. 4.21). The expression level of the 3D untransfected cells had a peak at 3 d and then decreased at 7 d to an even lower than the one on 1 d. In contrast to this, the gene expression of the miR-100-5p transfected cells was lowest at 3 d. After this, the gene expression minimally increased to the same level as on 1 d (Fig. 4.21). The expression of the miR-100-5p was nearly zero over the whole cultivation time.

Besides the miR-100-5p expression, both the expressions of bone morphogenetic protein receptor type 2 (BMPR2) and collagen type I (ColI) are of interest (Fig. 4.22). The BMPR2 expression of the 3D untransfected cells showed a higher expression level at all time points as compared to the miR100-transfected cells (Fig. 4.22 A). The relative gene expression of the 2D untransfected cells was lower than the expression of the 3D untransfected cells. The ColI expression of the miR100-transfected cells at 1 d had the highest values (Fig. 4.22 B). After 3 d, it had the same expression level as the other groups. The transfection and the reagents had no influence on the expression levels of BMPR2 and Col1 (Fig. A.1).

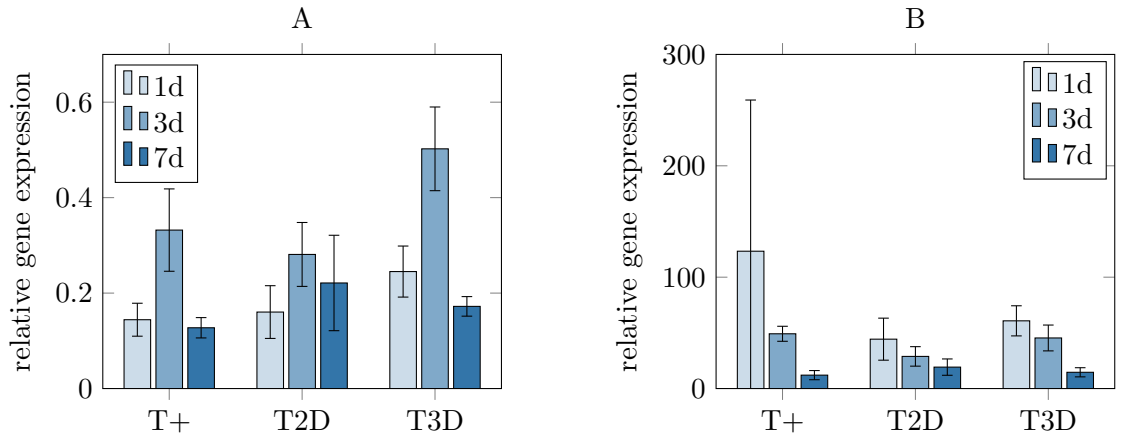

Figure 4.22.: BMPR2 expression (A) and collagen type I expression (B) after miR-100-5p inhibition of the transfected cells (T+), untransfected cell monolayer (T2D) and 3D (T3D) after 1d, 3d and 7d cultivation. Mean values and standard deviation are shown. Values are normalized to SNORD96a and expressed as $2^{\Delta C_T}$.

4.4. Correlations between the analyzed methods

In the previous sections, the data obtained by each method was analyzed independently. But it is also of great importance to look at possible correlations between parameters obtained by the different methods. In the following section, mainly the correlation to the measured BMD value was tested to determine further diagnostic indicators for the different stages of osteoporosis. Interesting parameters were the distribution of BMD over age. Moreover, correlations with the BV/TV, the porosity, the trabecular separation and thickness, and the degree of anisotropy were examined. Due to significantly different values in the healthy group as compared to the o/o group of F_{max} and F_{max} per area, the relation to the BMD was determined over all samples. As the femur head is very heterogeneous, the BMD value varies along the bone slice. Hence, a better correlation between BMD and the biomechanical parameters can be expected, if the BMD value of the cube is used. Furthermore, the correlation of BMD with the detected bone components was determined and also a correlation with the gene expression level was analyzed.

Age and BMD

The relation of BMD and age showed a negative correlation ($r = -0.4331$, $p = 0.0017$; Fig. 4.23). With age, the BMD decreased independently from the classification group (Fig. 4.23). The slice BMD and the cube BMD correlated significantly - independently of the grouping ($r = 0.6157$, $p = 0.0004$; Fig. 4.24 A). Looking at the BMD of the cubes before and after the biomechanical testing, the Spearman correlation showed a significant correlation ($r = 0.8818$, $p < 0.0001$; Fig. 4.24 B).

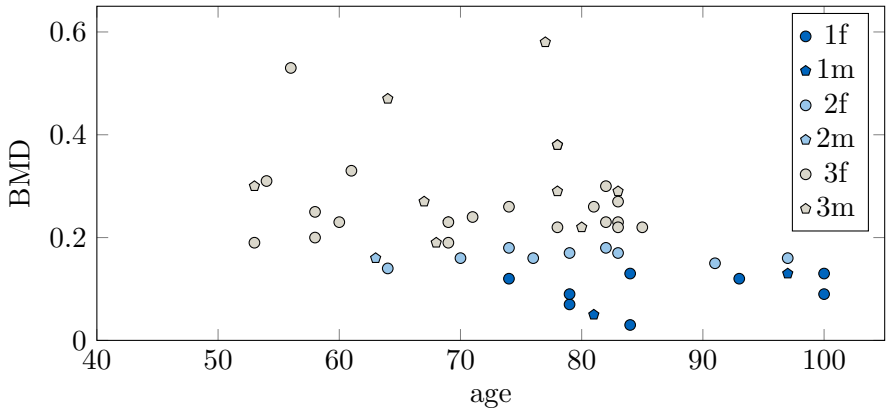

Figure 4.23.: Bone mineral density (BMD) [$g\,cm^{-3}$] distribution correlated to age [years]. Spearman correlation: r = −0.4331 (p = 0.0017). Circle: female (f); Diamond: male (m); 1 (dark blue): osteoporotic; 2 (light blue): osteopenic; 3 (gray): healthy.

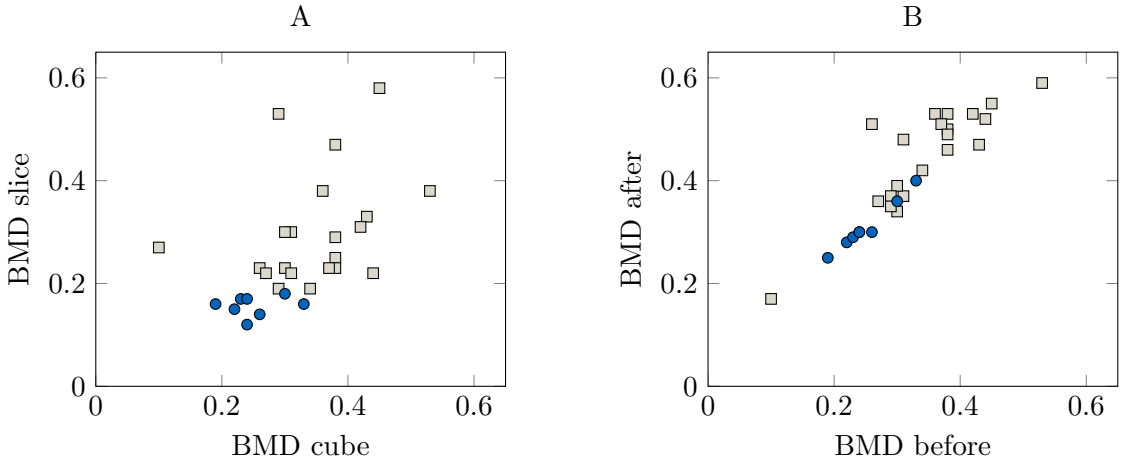

Figure 4.24.: Comparison of BMD [$g\,cm^{-3}$] of the bone slices and the bone cubes (A) and comparison of the BMD [$g\,cm^{-3}$] before and after the biomechanical testing (B). Spearman correlation in A: r = 0.6157, p = 0.0004, Spearman correlation in B: r = 0.8818, p < 0.0001. Healthy samples are marked as gray squares and o/o samples are marked as blue circles.

Micro-CT analysis parameter and BMD

The correlation of BMD with percent bone volume (BV/TV) showed a positive correlation ($r = 0.4592$, $p = 0.0010$; Fig. 4.25 A). An inverse correlation could be seen for the correlation of BMD with porosity ($r = -0.4592$, $p = 0.0010$; Fig. 4.25 B). Comparing the BMD with the mean trabecular separation, a negative correlation was shown ($r = -0.3079$, $p = 0.0333$; Fig. 4.25 C). Besides this, the correlation of BMD with the mean trabecular thickness showed a positive relation ($r = 0.3411$, $p = 0.0177$; Fig. 4.25 D). The correlation of the degree of anisotropy (DA) with the BMD of the slices showed a significant positive correlation ($r = 0.4509$, $p = 0.0010$; Fig. 4.25 E). Comparing the DA of the slices and the cubes of the healthy and o/o group, the DA of the cubes showed higher values for both classifications (healthy and o/o) (Fig. 4.25 F). The DA of the o/o group was significantly higher in the cubes than in the slices ($p = 0.0462$; Fig. 4.25 F).

Correlations with biomechanical parameters

Comparing the BMD of the slice with F_{max} showed no significant correlation ($p = 0.1123$), but a tendency to increase together ($r = 0.3012$; Fig. 4.26 A). The correlation of BMD with F_{max} per area neither showed a significant correlation ($r = 0.3459$, $p = 0.0661$), but the p value indicates that the correlation is not a random result (Fig. 4.26 B). Using the BMD of the cube instead of the BMD of the slices, the same correlation with F_{max} and F_{max} per area showed that there is indeed a correlation (Fig. 4.26 C-D). The Spearman coefficient for the correlation with F_{max} is $r = 0.6406$ ($p = 0.0002$; Fig. 4.26 C). And for the correlation with F_{max} per area, the Spearman coefficient is $r = 0.6468$ ($p = 0.0002$; Fig. 4.26 D).

Looking at the correlation of the cube porosity and F_{max}, the correlation was negative ($r = -0.6719$, $p < 0.0001$; Fig. 4.27 A). The correlation of BMD cube versus porosity showed a nearly perfect inverse correlation ($r = -0.9906$, $p < 0.0001$; Fig. 4.27 B). Looking at other biomechanical parameters, such as Young's modulus and toughness, the cube BMD only showed a correlation with toughness (Fig. 4.27 C). The Spearman coefficient for BMD cube versus toughness was $r = 0.4784$ ($p = 0.0087$; Fig. 4.27 C). For BMD cube versus Young's modulus, no significant correlation was verifiable with the study data ($r = 0.2281$, $p = 0.2340$; Fig. 4.27 D).

Correlating the toughness with F_{max} and with F_{max} per area, respectively, significant correlations were detectable (Fig. 4.28 A - B). The Spearman coefficient of F_{max} versus toughness was $r = 0.5517$ ($p = 0.0019$; Fig. 4.28 A). The Spearman coefficient of F_{max} per area versus toughness was $r = 0.4966$ ($p = 0.0061$; Fig. 4.28 B). F_{max} per area showed no significant correlation with age ($r = -0.1348$, $p = 0.4856$; Fig. 4.28 C).

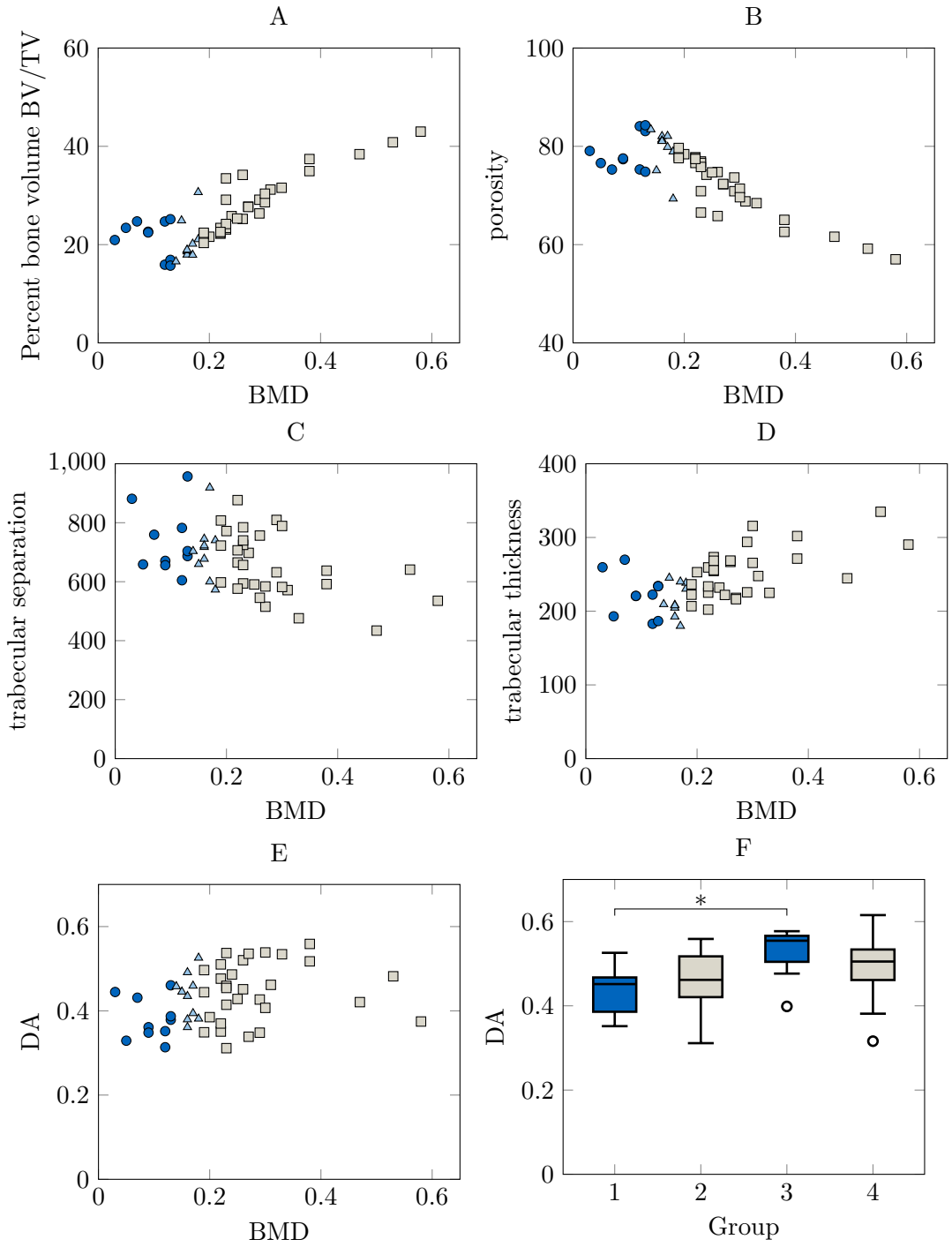

Figure 4.25.: Correlations of BMD with percent bone volume (BV/TV) (A), porosity (B), mean trabecular separation (C), mean trabecular thickness (D) and degree of anisotropy (DA) (E). Additionally, the DA of the bone slices (1, 2) and the bone cubes (3, 4) is shown (F). 1 and 3 indicate the o/o group and 2 and 4 indicate the healthy group (F). The parameters have the following units: BMD [g cm^{-3}], BV/TV [%], porosity [%], DA [-], trabecular separation and thickness [µm]. Dark blue circles: osteoporotic samples, light blue triangles: osteopenic samples, gray square: healthy samples. Outliers are marked as empty circles and significant values are marked as described in Tab. 3.8. (F).

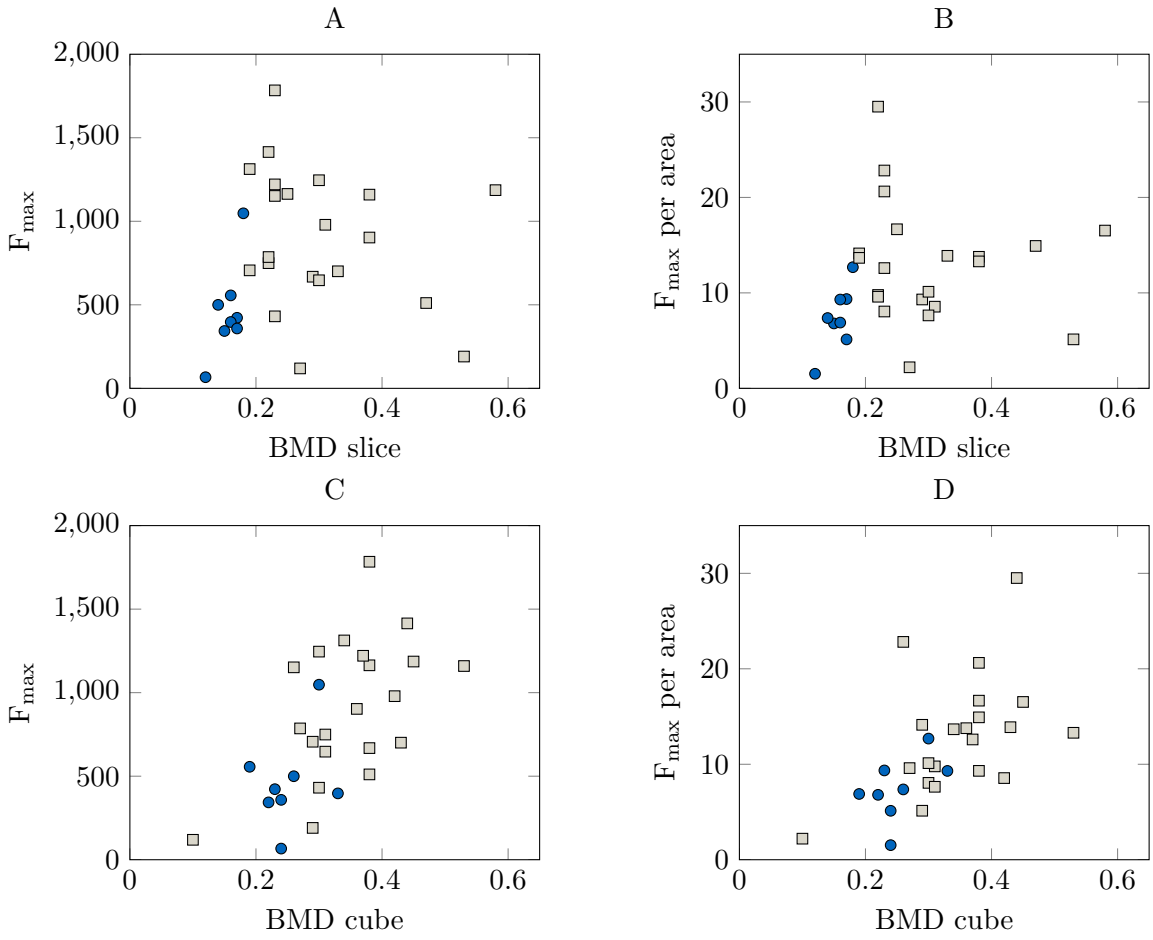

Figure 4.26.: Correlation of BMD to F_{max} (A, C) and to F_{max} per area (B, D) of the bone slices (A, B) and of the cubes (C, D). The parameters have the following units: BMD [$g\,cm^{-3}$], F_{max} [N], F_{max} per area [N/mm^2]. Blue circles: o/o samples; gray squares: healthy samples.

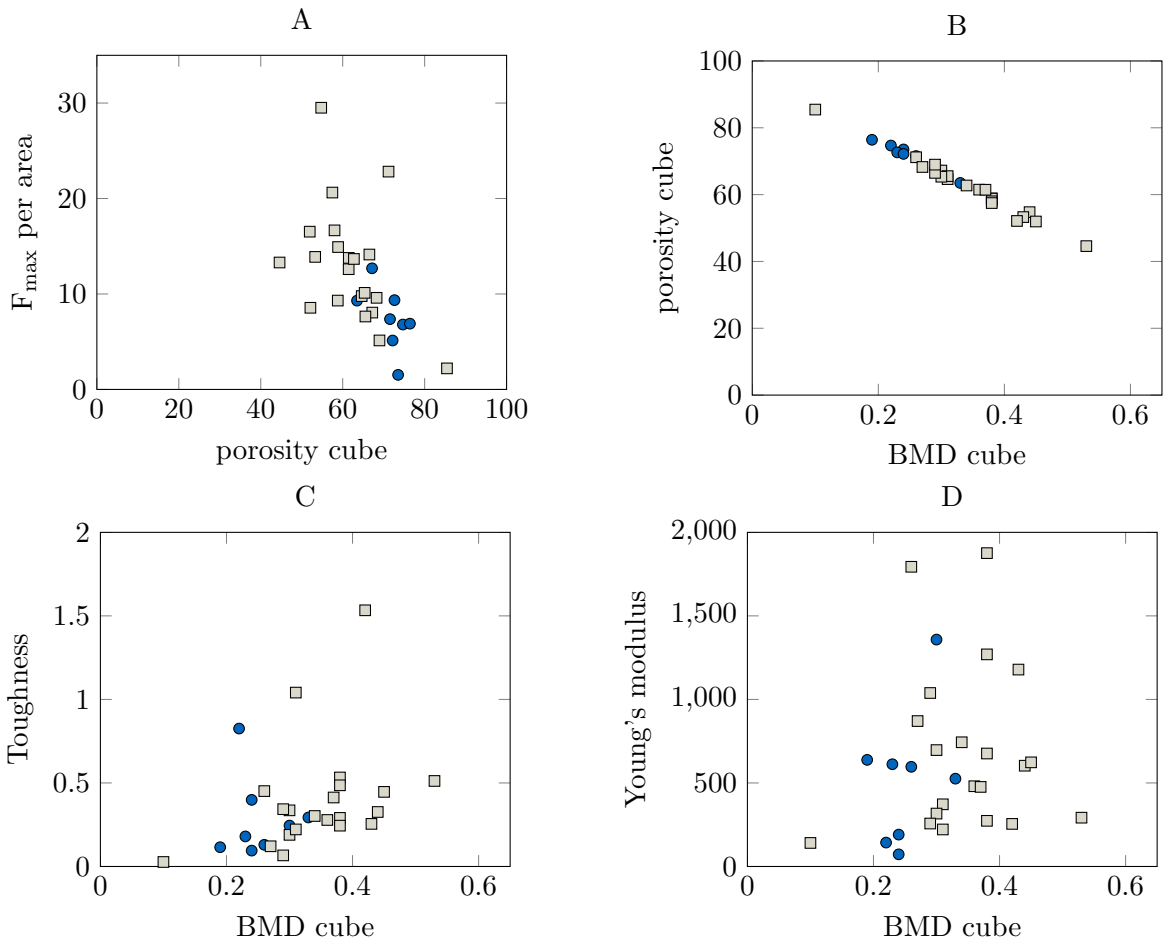

Figure 4.27.: Correlation of cube porosity to F_{max} per area (A). In addition, the cube BMD to porosity (B), to toughness (C) and to Young's Modulus (D) is correlated for the healthy (gray squares) and the o/o samples (blue circles). The parameters have the following units: BMD [$g\,cm^{-3}$], porosity [%], toughness [N/mm^2], Young's Modulus [N/mm^2].

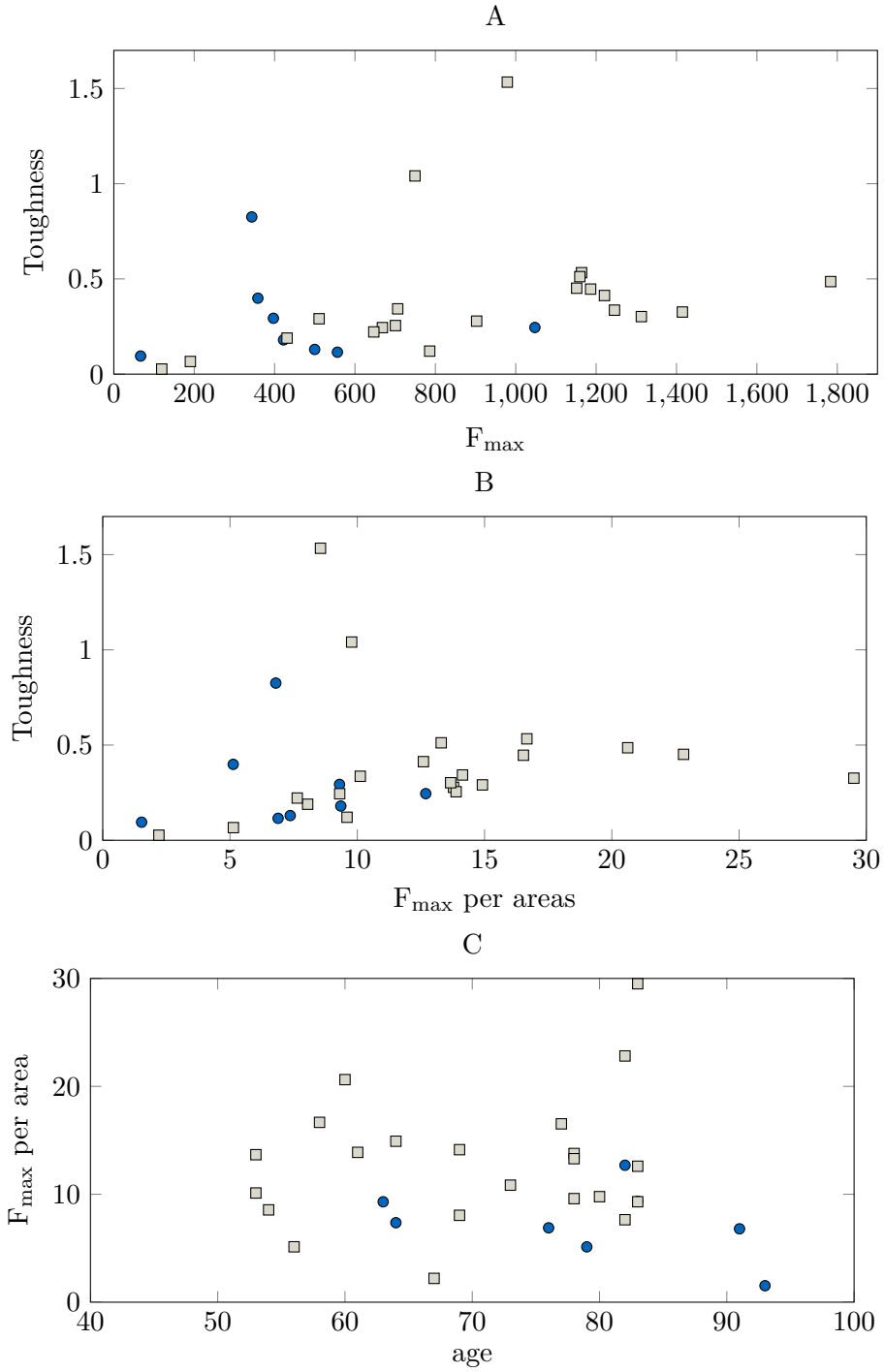

Figure 4.28.: Correlation of F_{max} and F_{max} per area with toughness (A, B) and F_{max} per area with age (C) of the o/o (blue circles) and the healthy samples (gray squares). The parameters have the following units: Toughness [N/mm^2], F_{max} [N], F_{max} per area [N/mm^2].

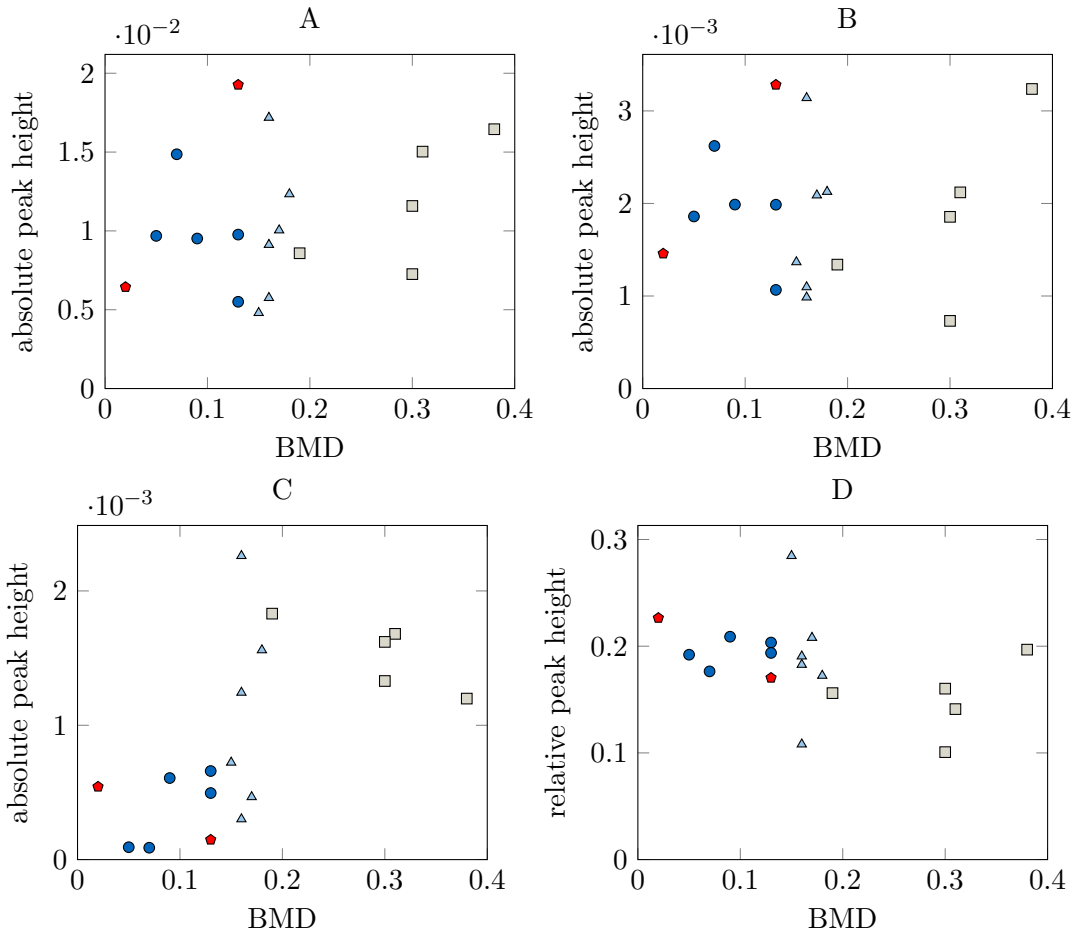

Figure 4.29.: Absolute peak heights of the bands at 960 cm^{-1} (A), 1070 cm^{-1} (B) and 1495 cm^{-1} (C) in the HA spectrum over BMD [g cm^{-3}]. Relative peak height of 1070/960 cm^{-1} of the HA spectrum over BMD [g cm^{-3}] (D). The osteoporotic samples are marked as dark blue circles. The osteopenic samples are marked as light blue triangles and the healthy samples are marked as gray squares. The two treated samples are shown as red diamonds.

Correlation of BMD and bone composition detected via Raman spectroscopy

BMD only showed significant correlations with absolute peak heights of the Raman spectroscopy for the band at 1495 cm^{-1} in the HA spectrum ($r = 0.5926$, $p = 0.0456$; Fig. 4.29 C, Tab. A.10). BMD showed no correlation with the absolute peak height of the phosphate band at 960 cm^{-1} and the B-type carbonate band at 1070 cm^{-1} and the CH_2 deformation band of the HA spectrum at 1450 cm^{-1} (Fig. 4.29 A-B, Tab. A.9).

For the lipid spectrum, only the absolute peak height of the band at 1495 cm^{-1} showed a significant correlation with BMD ($r = 0.7016$, $p = 0.0032$; Fig. 4.30 E, Tab. A.9). Taking only the data with a BMD below 0.2 g cm^{-3} into account, there were region-specific significances visible. BMD showed a significant positive correlation behavior with the absolute peak heights of the bands of proline at 868 cm^{-1} ($r = 0.6737$, $p = 0.0191$), phosphate band at 1079 cm^{-1}

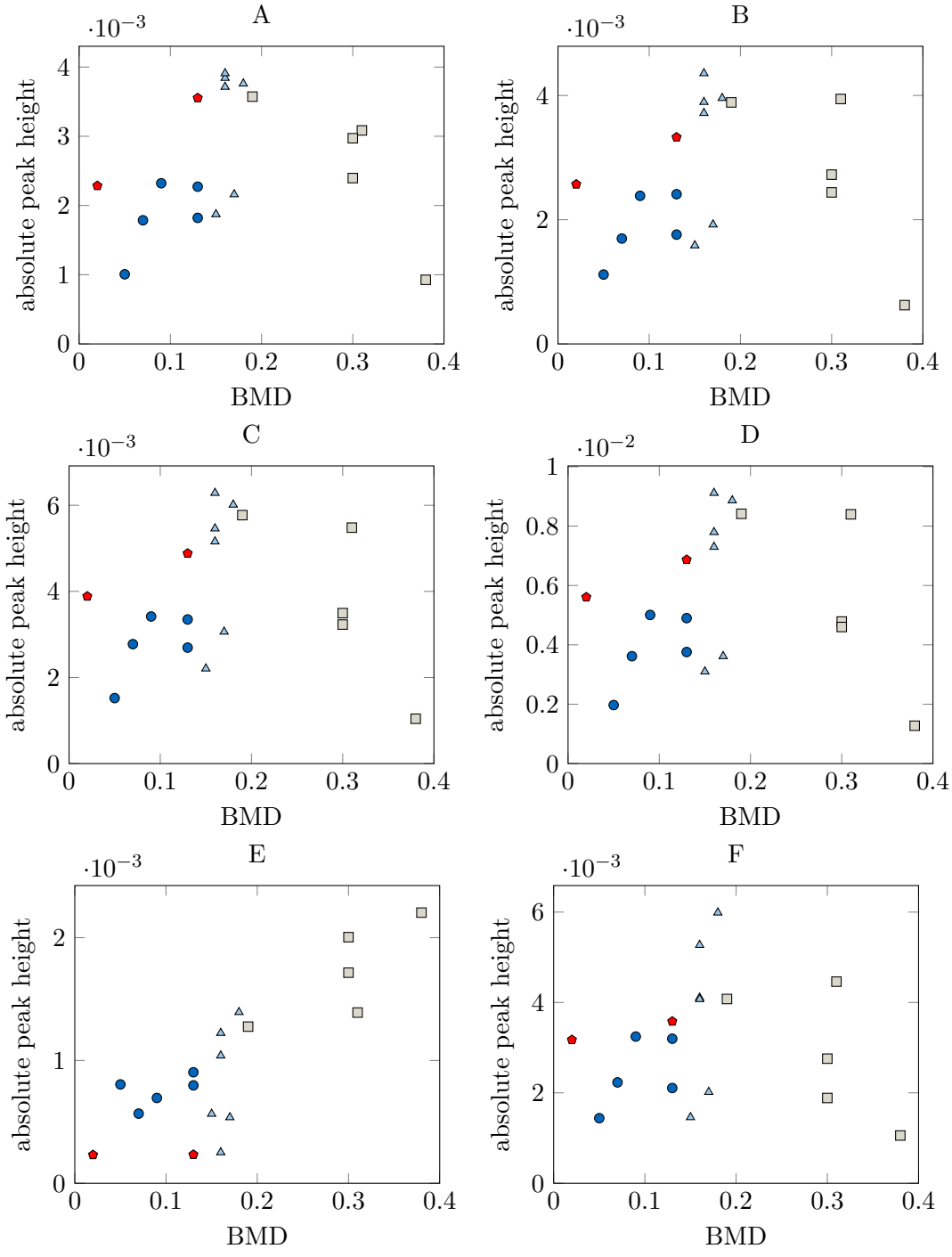

Figure 4.30.: Absolute peak heights of the bands at 868 cm^{-1} (A), 1079 cm^{-1} (B), 1300 cm^{-1} (C), 1440 cm^{-1} (D), 1495 cm^{-1} (E) and 1656 cm^{-1} (F) in the lipid spectrum over BMD [$g\,cm^{-3}$]. The osteoporotic samples are marked as dark blue circles. The osteopenic samples are marked as light blue triangles and the healthy samples are marked as gray squares. The two treated samples are shown as red diamonds.

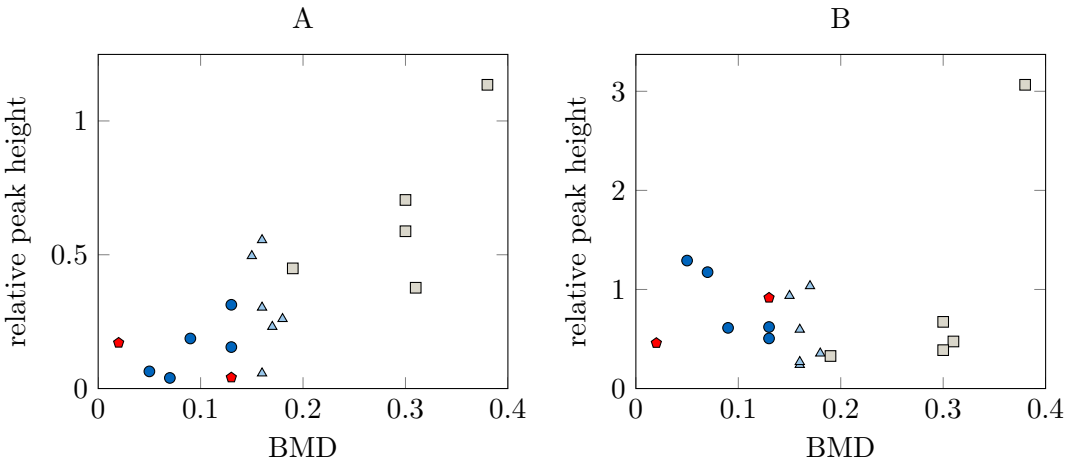

Figure 4.31.: Peak heights relative to amide I ($1656\,cm^{-1}$) of the bands at $1495\,cm^{-1}$ (A) and $1070\,cm^{-1}$ (B) in the HA spectrum over BMD [$g\,cm^{-3}$]. The osteoporotic samples are marked as dark blue circles. The osteopenic samples are marked as light blue triangles and the healthy samples are marked as gray squares. The two treated samples are shown as red diamonds.

(r = 0.6949, p = 0.0146), amide III band at $1300\,cm^{-1}$ (r = 0.6949, p = 0.0146), the CH_2 deformation band of lipids at $1440\,cm^{-1}$ (r = 0.6173, p = 0.0358) and the amide I band at $1656\,cm^{-1}$ (r = 0.5926, p = 0.0456) of the lipid spectrum (Fig. 4.30 A-D,F, Tab. A.10).

Besides the correlation with the absolute peak heights, the correlation with the relative peak heights was also of interest. The BMD only correlated to the ratio of the bands at $1495\,cm^{-1}$ of the HA spectrum to the $1656\,cm^{-1}$ of the lipid spectrum (r = 0.7238, p = 0.0021; Fig. 4.31 A; Tab. A.9). Looking at the relative peak height of the ratio 1070/960 cm^{-1} a tendency of an inverse correlation was determined (r = −0.4697, p = 0.0680; Fig. 4.29 E, Tab. A.9).

Making the correlations with a BMD below $0.2\,g\,cm^{-3}$, there were some region-specific significances visible, again. The relative peak height of the ratio 1070/1656 cm^{-1} showed an inverse correlation with the small BMD (r = −0.6173, p = 0.0358; Fig. 4.31 B, Tab. A.10). The ratio of the peak height of the lipid spectrum to phosphate at $960\,cm^{-1}$ correlated to the region-specific BMD for the lipid spectrum bands at $1079\,cm^{-1}$ (r = 0.6314, p = 0.0309), $1300\,cm^{-1}$ (r = 0.6173, p = 0.0358), $1440\,cm^{-1}$ (r = 0.6632, p = 0.0216) and $1656\,cm^{-1}$ (r = 0.5997, p = 0.0426) (Fig. 4.32; Tab. A.10).

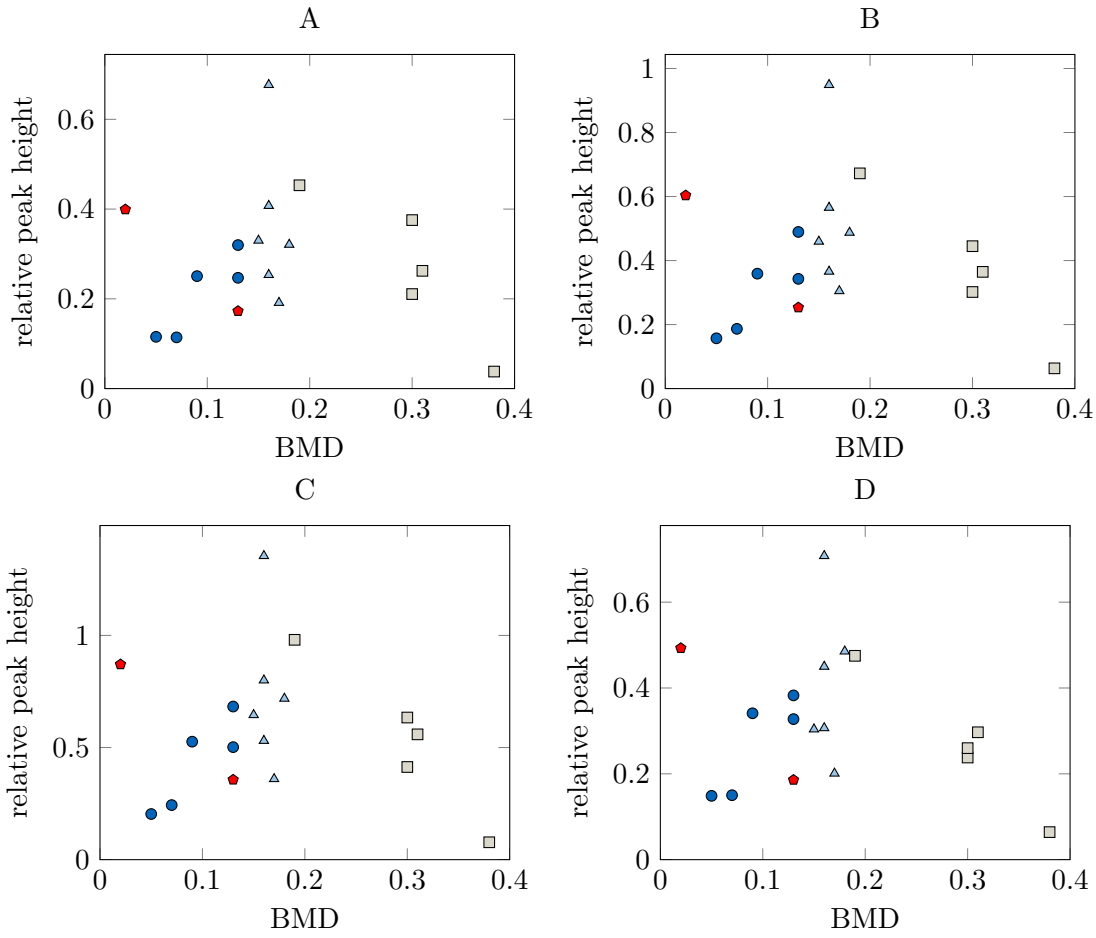

Figure 4.32.: Peak heights of the bands at 1079 cm^{-1} (A), 1300 cm^{-1} (B), 1440 cm^{-1} (C) and 1656 cm^{-1} (D) of the lipid spectrum relative to bone mineral (960 cm^{-1}) over BMD [$g\,cm^{-3}$]. The osteoporotic samples are marked as dark blue circles. The osteopenic samples are marked as light blue triangles and the healthy samples are marked as gray squares. The two treated samples are shown as red diamonds.

Correlation of relative gene expression and BMD

BMD shows no significant correlation with the relative gene expression of miR-100-5p ($r = 0.04661$, $p = 0.8543$; Fig. 4.33).

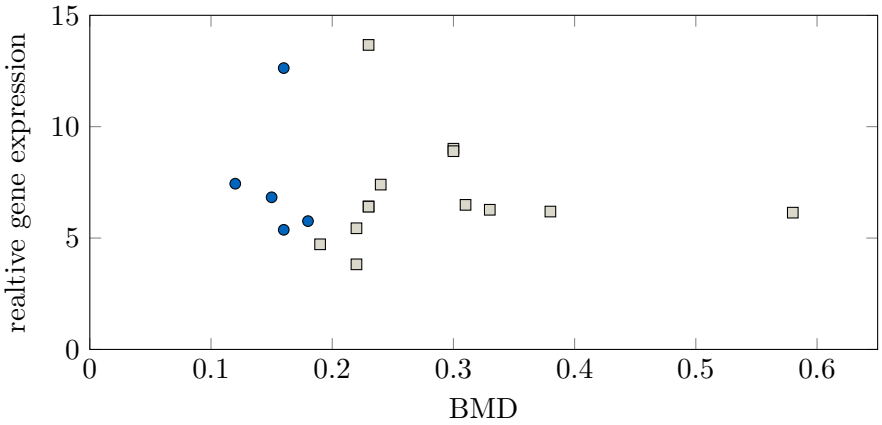

Figure 4.33.: Correlation of the BMD [$g\,cm^{-3}$] to the relative gene expression of miR-100-5p of the healthy samples (gray squares) and the o/o samples (blue circles).

5. Discussion

The importance of bone quality has remarkably increased during the last few years. Bone quality is the symbiosis of bone architecture and chemistry of the bone tissue. This factor cannot be assessed by DXA measurements [59]. These measurements only lead to a density of HA per area value. This value is physically difficult to interpret and cannot be converted into a volumetric density. In contrast, the BMD - which is used in this thesis - is a volumetric density. Additionally, the DXA measurements are affected by bone size and cannot separate cortical and trabecular bone [25]. Furthermore, the indication for a DXA measurement cannot be made directly in a trauma surgery department. In all cases, trauma surgeons can only give some advice in the medical report, if the subjective grading leads to a recommendation for a validation of the bone density. In general, the diagnosis of osteoporosis is made after a fracture already occurred and the pathology of osteoporosis is established. An earlier detectable and simpler method for diagnosis of osteoporosis is necessary, which can be performed routinely by general practitioners or in an orthopedic/trauma surgery department.

Additionally, new drugs to treat osteoporosis need to be developed to reduce side effects, as bisphosphonates for example are related to osteonecrosis [129]. Furthermore, the bone healing ability in osteoporosis is reduced . Therefore, patient-specific implants need to be developed for osteoporotic patients.

The results presented in this thesis show new possible parameters for the diagnosis of osteoporosis in addition to DXA measurements. Moreover, scaffolds were designed, which allow osteoporotic osteoblasts to grow on them. Additionally, it was possible to decrease the miR-100-5p expression of osteoporotic osteoblasts through transfection in 3D. This shows that the concept of transfection is possible in 3D and provides a new drug delivery approach with implants and scaffolds.

5.1. Osteoporosis prognosis and research

By now, there is still a lack in osteoporosis prognosis. For an improvement, osteoporosis needs to be better understood. Because of this, animal models for an enhanced etiology and preclinical evaluation of new therapies to prevent osteoporosis have been established [169, 171]. *In vivo* models presented in the literature are by now mostly with female animals, which underwent an ovariectomy, because the predominant type of osteoporosis is postmenopausal osteoporosis [86, 169, 171]. *In vivo* models with male animals to better understand osteoporosis in men are not performed frequently and osteoporosis is always induced in male rats with an orchiectomy. The bone loss rate is slower in male rats as compared to female rats. This leads to the suggestion that male rats are not as sensitive to sex hormone deficiency as female rats. This could be one of the explanations why women suffer more often from osteoporosis. Concerning the BMD of the collected samples within this thesis, the BMD of the female bone

samples was significantly lower as compared to the BMD of the male bone samples. For the used samples in this thesis, there was no significant difference detectable between the sexes in the healthy group and the osteoporotic group (Fig. 4.1). The sample number of osteoporotic human bone for research applications is highly limited. If there are samples of diagnosed osteoporotic bone, then osteoporosis is usually already established and often already treated. Furthermore, sex-specific observations are difficult to set up because of the lower amount of osteoporotic men. This is also a limitation of this thesis. From the 14 men included into this study, only two osteoporotic men and one osteopenic man were observed. Therefore, no sex-specific observations were made in this thesis.

Aging also is a parameter, which has to be taken into account in osteoporosis research. In general, the age-related decrease of BMD occurs in both men and women [62, 130]. Because of this decrease, the risk for fractures increases. Mostly, women have a higher risk for fractures, because the bone loss starts rapidly after menopause [130]. Cui et al. showed a dependence of age for several microstructural parameters [36]. The measured samples also showed such a correlation between BMD and age (Fig. 4.23). The BMD decreased with age. Moreover, Hannan et al. showed that the BMD declines linearly with age and additionally found that no differences in the slope of the curves of the BMD loss between men and women exist [62].

5.2. Bone characterization

Micro-CT analysis, biomechanical testing and Raman microspectroscopy were performed to analyze the bone samples. The detailed results about bone characterization allow a better understanding of the osteoporotic bone architecture and chemistry.

Micro-CT

A low bone mass and thinner trabeculae are characteristics of osteoporosis. As progressive transition from healthy to osteoporotic, the additional group of osteopenic is defined as bone with reduced bone mass. The areas, in which DXA measurements are performed, are in general the lumbar spine and the femoral neck. Those areas have higher loads and if the bone quality changes in these regions, the risk of a fracture increases dramatically. The femur head has the highest load, which will be transferred on to the neck and the femur. The femur neck is the weakest area in this structure and fractures occur there most often. In this thesis, the femur head is used for all measurements, because the femur neck is destroyed during fractures and the share of the residual parts of the neck is too small to test and the testing region cannot be standardized. The area around the fracture should not be taken into account for measurements, as the bone properties in this area change during fracture.

Comparing results between different osteoporotic studies with the actual results of this thesis can be difficult due to different classification parameters, threshold values and measured areas. Particularly the measured area has a high impact on the BMD value. The BMD of a slice through the femoral head in general has smaller values than the BMD of the cube taken from the central region of the main load axis (Fig. 4.24 A). However, the correlation of both BMDs is significant (Fig. 4.24 A). Hence, conclusions between other parameters and the BMD in the center can also be made for the BMD of the whole slice and vice versa - at least for the

samples used in this thesis. In the area of maximal load, thicker trabeculae are visible and thus a higher BMD is measurable (Fig. 4.2). Furthermore, Cui et al. showed that microstructural properties of proximal femoral trabeculae are depending on the region [36]. In addition, Li et al. showed that the bone density (BD) changes with the measured area [90]. Moreover, the lateral BD is even lower compared to most of the measured sides in the femur head. The inferior area shows similar values to the lateral area. This shows a dependence of BD to loading [90]. Considering this, it is clear that BMD changes with the area where it was measured. Thus, a comparison of the actually measured BMD with the BMD found in the literature is difficult.

Looking at the degree of anisotropy (DA), the bone structure of the healthy group is more anisotropic than the osteoporotic group (Fig. 4.3 C). Cui et al. showed that the used osteoporotic sample is more anisotropic than the healthy samples [36]. However, they only used two samples per group and they measured human vertebrae. The other used osteoporotic sample showed a two times lower DA [36]. Comparing the DA of the bone cubes, it is visible that the DA is higher than the DA of the slices for both groups (Fig. 4.25 F). This is due to the measured area of the cubes. In the area of the main load, the trabeculae are mostly oriented in the direction of the load. The lower anisotropy in the slices of the osteoporotic group hence is caused by bone degradation at the edges of the bone and not due to bone degradation in the center at the maximal load axis. Martens et al. showed that because of the high variation between bone specimens, an effect of anisotropy is difficult to detect [106]. However, a correlation between DA and BMD of the bone slices could be detected with the data of this thesis.

The results of the thesis show that BMD inversely correlates with porosity (Fig. 4.25 B). As porosity and also the BV/TV values depend on the percentage of bone to liquid, it is not surprising that the BV/TV correlates with the BMD value, too (Fig. 4.25 A). According to the grouping criteria, this behavior is also seen in Figure 4.3 A and Figure 4.3 B. However, the BV/TV ratio highly depends on the measured region [172]. Additionally, Ulrich et al. measured the BV/TV in 58 femoral head samples in a range of 8.30 % to 31.68 % with a mean BV/TV of 20.67 % [172]. The mean BV/TV is a similar range as the BV/TV measured in this thesis, however, Ulrich et al. did not group the samples into patients with and without bone disorders [172].

Besides the lower bone mass in osteoporotic patients, also thinner trabeculae are visible. This can be seen in the trabecular thickness distribution of the used samples (Fig. 4.4). Besides that, also the correlation with BMD shows that with increasing BMD, the trabecular thickness increases, too (Fig. 4.25 D). Additionally, an inverse correlation exists for trabecular separation with BMD (Fig. 4.25 C).

Biomechanical testing

In osteoporotic patients, the fracture risk is increased. This leads to the assumption that these patients have a lower F_{max} value and additionally the potential of energy absorption (toughness) in a fall is lower. Martens et al. tested the impact of the trabecular bone at the main load axis by measuring the strength before and after drilling a whole at this side [106]. They showed that with a missing middle bone part, the strength dramatically decreased [106]. This implicated the importance of the trabeculae at the maximal load axis. In the samples

analyzed in this thesis, the measured values of F_{max} and F_{max} per area are significantly higher in the healthy group as compared to the o/o group (Fig. 4.14 C-D). This leads to the conclusion that the grouping via BMD of the bone slice can also be used for analyzing the values of the biomechanical testing and no BMD measurement of the biomechanical sample would be necessary. However, a significant correlation of F_{max} with BMD of the slice could not be observed (Fig. 4.26 A). The same applies for the correlation of F_{max} per area with the BMD of the bone slice (Fig. 4.26 B). A correlation can only be made with the BMD of the bone cube (Fig. 4.26 C-D). With increasing BMD, F_{max} and also F_{max} per area increase. This is surprising, as the BMD of the slice and cube are correlating, but the small fluctuations in the BMD cube seem to be relevant for the correlations with biomechanical parameters. This behavior also occurs in the toughness (Fig. 4.14 F). Thereby, the correlation with the BMD cube shows an increasing correlation (Fig. 4.27 C). With increasing BMD, toughness also increases. Toughness is the parameter for the possible energy absorption, which can be absorbed by the bone until a fracture occurs. As the maximal load-to-failure (F_{max}, F_{max} per area) increases, toughness increases, too (Fig. 4.28 A-B). Li et al. could neither detect a significant difference between normal and osteoporotic bone, but could show that the osteoporotic bone can absorb less energy than normal bone [90]. The before-mentioned parameters are highly influenced by the sample origin. Due to this and the huge variation in the measuring machine setup, it is hard to compare values of different studies.

The Young's modulus did not show a significant difference or correlation - neither in the grouping nor in the correlation with the BMD of the bone cube. Only a tendency to lower values for low BMD values was established (Fig. 4.14 A; Fig. 4.27 D). Li et al. observed Young's modulus values in healthy bone samples in the range of $150\,N/mm^2$ to $450\,N/mm^2$ [90]. They could show a significantly lower mean Young's modulus in the osteoporotic samples as compared to healthy samples [90]. Looking closer at the single measured areas, no significant difference between both groups could be detected, too. However, there were no samples in any of the groups with a Young's modulus higher than $600\,N/mm^2$ as in the bone samples used for this study. Katsamanis et al. tested dried femur shafts with the Hopkinson bar stress technique [75]. They characterized the dynamic and static stress-strain response of the bone and found that the Young's modulus of both methods are similar. They also compared the Young's modulus and Poisson ratio of other groups and found that both are depending on the measuring method and the measuring conditions (wet/dry). Hence, there is considerable uncertainty in the measured values. Comparing biomechanical values with other micro-CT values, a dependence could be observed for example for F_{max} with porosity. Between those two parameters, a significant inverse correlation can be observed (Fig. 4.27 A). The determined biomechanical values are not representative for the complete bone slice. As according to Li et al., Young's modulus, yield strength and toughness vary in the different regions of the femur head [90].

Raman microspectroscopy

Raman spectroscopy is a highly sensitive technique that can detect bands, which only exist in immature tissue or in chemically/mechanically treated tissues/proteins [107, 119]. For example, staphylococcal osteomyelitis was diagnosed via Raman spectroscopy [80]. Differences in the spectra of human and animal bone tissue are reported as function over age, biomechanical status, pathology or other quality parameters [118]. Typically, mineral-to-matrix ratio,

carbonate-to-phosphate ratio or mineral crystallinity are reported as bone quality parameters. However, differences between studies can occur because of the varying usage of band intensities rather than composition differences. Nevertheless, it is a promising approach of a label-free and chemically selective composition evaluation in *ex vivo*. With further development, it can be a possible *in vivo* assessment to determine osteoporosis-specific characteristics in the composition of bone. The possibility of dividing the bone spectrum into mineral spectrum (HA spectrum) and matrix spectrum (lipid spectrum) is a huge advantage of Raman microspectroscopy and can lead to a further improvement of characterization of tissues and diseases. For example, the B-type carbonate band at $\approx 1070\,\mathrm{cm}^{-1}$ for bone mineral and the component of a phosphate band at $\approx 1079\,\mathrm{cm}^{-1}$ can easily be separately analyzed now. The problems in separating two peaks that are close to each other during accurate band fitting of one spectrum with all components (mineral and matrix) can be reduced [101].

Bone consists of two components - a cellular one and a non-cellular one [102]. The cellular component consists of osteoblasts, osteoclasts and osteocytes. The non-cellular component consists of a mixture of water, mineral and organic components. Calcium and hydroxyapatite are the main components of the mineral part of the bone. Collagen is the main organic component. Looking at the results of Raman microspectroscopy in Section 4.1.2, there were no significant differences in the samples between the osteoporotic, osteopenic and healthy group in the absolute amount of each component observable (Fig. 4.6 to 4.11). Also, no correlation of BMD with the absolute amount of each component could be detected (Fig. 4.30 and 4.29). Tendencies were visible for the ratio $1070/960\,\mathrm{cm}^{-1}$ with p=0.1185 and for the correlation with BMD (p = 0.068) (Fig. 4.9 A and 4.29 D). As bone has a highly irregular structure and local variations regarding its components, it may be necessary to measure more areas to get representative bone sample values (for further explanations on limitations see Section 5.5). Only the band at $1495\,\mathrm{cm}^{-1}$ showed a difference in both spectra between the two groups. This band is not a typical band of the bone spectrum. Further experiments need to be performed to analyze this peak, which could not be done within the time frame of this thesis. A first guess for this peak at the band could be a substance of the phenylpropanamide group, such as fentanyl. Fentanyl is used as standard analgesic during total endoprosthetic surgery. But this would not explain why the peak is only detectable in healthy samples and some osteopenic samples.

The peak intensities not only depend on tissue components, but also on laser power and on the optical components in the Raman spectroscopy system. Therefore, peak ratios are more reliable to detect differences in spectra and to compare the values with the literature [127]. Looking at the correlations of the various bands and ratios to BMD, there were no correlations within the typical bone spectrum bands/ratios (Fig. 4.29 to 4.31). If only the samples with a BMD smaller than $0.2\,\mathrm{g\,cm}^{-3}$ are considered, then correlations are existing. With decreasing BMD, the absolute intensities of the proline band ($\approx 868\,\mathrm{cm}^{-1}$), the phosphate band ($\approx 1079\,\mathrm{cm}^{-1}$), the amide III band ($\approx 1300\,\mathrm{cm}^{-1}$), the CH_2 deformation band in lipids ($\approx 1440\,\mathrm{cm}^{-1}$) and the amide I band ($\approx 1656\,\mathrm{cm}^{-1}$) seemed to be decreasing. Looking at the correlations with the smaller BMD to the ratios of phosphate/carbonated apatite (1079/960 cm^{-1}), amide III/carbonated apatite (1300/960 cm^{-1}), CH_2 deformation/carbonated apatite (1440/960 cm^{-1}) and amide I/carbonated apatite (1656/960 cm^{-1}), the ratio seemed to increase with increasing BMD. The B-type carbonate/amide I ratio (1070/1656 cm^{-1}) seemed to decrease with increasing BMD. However, a clear statement cannot be made, because the sample number of the osteoporotic and osteopenic samples

(BMD $< 0.2\,\mathrm{g\,cm^{-3}}$; n = 13) was three times as large as the healthy samples (n = 4). Measurements including more healthy samples need to be made to be able to make a concrete statement about disease-specific variations in ratios (or absolute amounts) of components. Furthermore, Draper et al. showed that a difference in Raman spectra between healthy and osteoporotic bone can be "quite subtle" [42]. As bone modeling is a continuous remodeling process, tissue age is variable within the same sample [54]. Thus, appearance of differences or no differences can depend on the tissue age/stadium. Mirzaali et al. could detect that neither the crystallinity nor the amide I/carbonated apatite (1656/960 $\mathrm{cm^{-1}}$) ratio correlates with age or sex in cortical bone samples [114].

BMD is a function depending on the porosity and the mineralization of bone tissue [146]. If the composition of bone trabeculae does not change, lower bone mass indicates a lower BMD. The ratio of BMD to porosity is equivalent to the density of HA in the trabeculae. As the BMD correlates with porosity, no significant change in the density of HA in every trabecula is present (Fig. 4.25 B). This indicates that the trabecular composition is almost the same for all samples. Especially in the central region, BMD correlated with porosity (p = 0.001). Subsequently, this could lead to the assumption that the changes in the Raman spectrum come from local changes in the trabecula or from changes between neighboring trabeculae and not from changes in the general composition of trabeculae. To get region-specific values, the area of interest for the Raman spectrum has to be increased or at least measurements at several regions have to be performed. Comparing Figure 4.25 B with Figure 4.27 B, it can be observed that with lower BMD values, the correlation differed in Figure 4.25 B, but not in Figure 4.27 B for BMD values from the central region. This could indicate that changes in the HA density of the trabeculae and therefore in the bone composition only appear in the outer regions and not in the region of maximal load. But as only one sample with BMD smaller than $0.13\,\mathrm{g\,cm^{-3}}$ was used in biomechanical testing and hence in Figure 4.27, such a conclusion is not valid yet. If differences between osteoporotic and healthy bone are measurable and correlations between micro-CT analysis and/or biomechanical testings are existing, then it may be feasible to use Raman spectroscopy as diagnostic tool for osteoporosis. Draper et al. showed that it is possible to measure the mineral and the organic phase of bone tissue in healthy and osteogenesis imperfecta mice through healthy skin i.e. transcutaneously [42]. Thus, there is a potential for Raman spectroscopy to be used in osteoporosis diagnostics and further improvements are possible.

5.3. Scaffold characterization

Silk fibroin-based scaffolds deliver the possibility for easy chemical modifications, so the potential for changing the structure architecture and immobilization of growth factors are huge [147]. Overall, the silk fibroin-based scaffolds offer a large potential to be used as biomaterial in bone tissue engineering [47, 51, 104, 117, 131, 145, 177].

All three silk fibroin scaffold types are biocompatible and support cell attachment and viability. There is no strong difference between the three scaffold types regarding those parameters. Comparing the proliferation values with Font et al. showed a similar cell behavior [51]. The absolute amount of dsDNA was not comparable, as Font et al. used a higher initial cell number due to a large scaffold [51]. The high fibroin content scaffolds (HF) showed a more robust

handling during cell culture than the low fibroin content scaffolds (LF). Also, the cytotoxicity was lower in the HF and HF+ scaffolds than in the LF scaffold, which led to a preferred usage of the HF scaffolds for the transfection experiment. The usage of the superhydrophic surface of the plastic dish for the HF+ scaffold production led to no improvement compared to the HF scaffold.

Total porosity and percental object volume of all scaffolds types were similar to the analyzed bone porosity and BV/TV (Tab. 4.5 and Tab. 4.2). The fractal dimension (FD) of the scaffold was similar to the FD measured in bone. In both cases, this indicates a rough surface. Majumdar et al. found that the FD of dried vertebal bodies is around 1.6 for healthy subjects and around 1.18 for osteoporotic subjects [99]. However, they also showed that calculation of FD is depending on the used CT scanner, filter and the calculation algorithm. Moreover, Chappard et al. proved that the FD calculation is depending on the used algorithm [26]. They also found that a high FD is associated with a higher bone volume. As the scaffolds and the bone samples were scanned with the same micro-CT, the parameters are comparable. However, a comparison with the literature is limited.

The degree of anisotropy (DA) of the scaffolds was slightly higher than the DA of the osteoporotic bone samples, but in a similar range as the healthy samples. The object surface to volume ratio of the scaffolds was higher than the bone surface to volume ratio. This indicates that the scaffolds have a more complex structure than bone. This could be the case, because the mid-range structure thickness of the scaffolds was three times lower than the trabecular thickness of the bone. Furthermore, the range in the trabecular thickness of bone was wider than the trabecular thickness of the used scaffolds.

5.4. Expression of miR-100-5p

MiRNA and anti-miRNA have a huge potential to be used in bone tissue engineering. Several miRNAs have already been tested *in vivo* [4]. Examples are miRNA-26a, anti-miRNA-34a miRNA-148b and anti-miRNA-221 [4]. Those miRNAs showed good results with regard to new bone formation and are involved in the BMP signaling pathway. The translation of this potential to osteoporosis-specific therapy is still missing. Seeliger et al. and Kelch et al. could identify miR-100-5p as upregulated in serum and bone tissue of osteoporotic patients [77, 155].

The expression levels of the used osteoblasts showed no significant difference in the expression of miR-100-5p in the healthy samples as compared to the o/o samples (Fig. 4.20 B). Furthermore, a correlation with BMD was not existing and no tendency was observable (Fig. 4.33). This could be due to the used sample numbers. Moreover, the o/o group had more osteopenic samples than osteoporotic samples. As osteopenia is a progressive transition between osteoporosis and healthy tissue, the difference in the expression level of the o/o samples as compared to a healthy sample in combination with natural changes in the expression level could be the reason for the difficulty of a clear separation. A clear segmentation of different stations of osteopenia could not be made. Definitely, further research is necessary to analyze the correlation of miRNA expression to osteoporosis. However, the expression level over all samples showed a difference in low level expression and high level expression (Fig. 4.20 A). Motivated

by the ambiguous results of [155] and [77], the transfection in a 3D experiment was performed with osteoblasts of an osteoporotic sample with a high expression level of miR-100-5p.

A difference in miR-100-5p expression between the transfected cells and the untransfected cells in 2D and 3D was clearly visible. However, due to a too small sample number, this difference was not significant (Fig. 4.21). Also, a statement on the influence on BMPR2 and Col1 expression levels could not be clearly made, because of the limited sample number (Fig. 4.22). However, the transfection in 3D was a great success and a huge step forward on the way to an osteoporosis-specific implant. By now, only transfection of cells in 2D was performed and if a 3D model was used, the cells were transfected before seeding onto the scaffold [4, 92, 95] and not - as it was done in this thesis - by means of a modified scaffold.

Given a miRNA or a miRNA pattern, which is characteristic for osteoporosis, modifications of its expression can be used as treatment of osteoporotic cells. The presented results show in principle that the attaching osteoporotic cells can be directly influenced by adding a miRNA sequence on a scaffold. This provides the possibility to improve the healing capability of osteoporotic-induced fractures.

5.5. Limitations of used methods

Micro-CT is a highly useful method for measuring BMD and other bone parameters. The main restriction - in case of this thesis - was the diameter of the scanning chamber of the used micro-CT equipment. Scans were performed with an *in vivo* micro-CT, which can be used for scanning rodents. The initial concept was to scan the whole femur head, but because of the diameter of the chamber and the total scanning time, the femur head needed to be cut into slices for scanning. Some bones could also not be used because of the fracture grade or additional cuts/holes during the surgery procedure, which were located in the region of interest. For some samples, it was impossible to cut a slice because of this. As human femur heads show irregular structures, the position of the region of interest needed to be selected to fit in all sizes of femur head slices and to be representative for the sample. The sample size is also important for the BMD calculation, particularly when using human bone samples.

Raman microspectroscopy is a highly sensitive method for detecting even the smallest amounts of substances or even chemical compounds. Because of the high sensitivity, the measured area needed to be as large as possible for the bone slices. The final scans with a 600×600 µm area are, compared to normal scanning areas of the Raman microspectrometer, extremely large. However, the measured area was very small when compared to the area of the entire bone slice. Several measurements over the complete slice could be more representative. Also, measurements in the outer regions, where large changes were visible (as in the micro-CT reconstruction), could be useful. But both were not feasible due to time limitations within this thesis.

As the biomechanical properties of bone differs because of the state in which it was measured, a comparison with the literature is rather difficult. Currey also found that the time that goes by until the sample is dried was not well-known in the earlier years of biomechanical testing and was therefore not considered, which led to odd values [39]. An improvement of techniques

led to a more detailed understanding, but bone behavior and also the cracking mechanism are still not completely understood [39].

6. Conclusion and Outlook

Osteoporosis diagnosis is still mostly conducted after the disease has fully developed and one or more non-traumatic fractures already occurred. DXA measurements only show a small piece of the actual situation and cannot provide any prediction. Thus, an early diagnosis tool is needed and is in great demand. In addition, an implant specific for osteoporotic patients to treat fractures is not yet available.

Characterization of osteoporotic bone using different methods and at different levels (tissue, cellular and molecular) leads to a better understanding of disease-specific bone changes and can lead to an earlier diagnosis. This work shows the potential in correlating various methods/parameters. Additionally, the possibilities in bone tissue engineering of foamed silk fibroin scaffolds is shown in this thesis. Furthermore, a successful transfection of osteoblasts with miRNA through the treated scaffold in 3D is shown. These results convey an impression of what is possible using the bone tissue engineering approach.

However, there is still a lot space for improvement in characterization/identification of osteoporotic bone. To get more information about the bone composition in an osteoporotic patient using Raman microspectroscopy, measurements in additional regions are necessary. The outer regions of the bone thereby seem to be the most promising region. During this thesis work, it became clearer that osteoporosis leads to strong regional changes, particularly in the outer regions in femur heads. However, these structural changes are not distributed evenly across the femur head, but only intermittently. This makes it even harder to select one region of interest or a representative area for any kind of measurement. The Raman microspectroscopy measurements show variations in the composition because of individual local variations and not because of disease-specific variations. Screening miRNA expression in bone and blood, as easier accessible sources, could lead to another diagnostic option. Additionally, looking for osteoporosis-specific patterns of miRNA and not only for a single expression level could improve the diagnostics of osteoporosis. Establishing a new therapeutic approach with miRNA is by now still challenging, as it is not clear if different miRNAs with different expression levels are influenced.

Furthermore, the scaffold design shows great improvement potential. It is clear that silk fibroin cannot replace a total endoprosthesis of the hip, but it could be used as filling material for fracture treatment and as alternative to cancellous bone to treat osteoporotic patients. The addition of further bioactive factors is possible and easily feasible because of the high binding potential of silk fibroin. However, more *in vitro* and *in vivo* experiments are necessary to find the optimal scaffold configuration with miRNA and the optimal combination of bioactive factors for obtaining a bone substitute material in the special case of osteoporosis.

Acknowledgment

First of all, I would to thank my family and friends. Especially my mother, who supported me my whole life and believed in me. Also a special thanks to Lukas, who was always there during the last years and motivated me even on the darkest days.

I would like to thank Asst. Prof. Elizabeth Rosado Balmayor for supervising this thesis and giving me the chance to work on this interesting topic. Additionally, I thank Prof. Martijn van Griensven for giving me the opportunity to work in his lab. I also thank Prof. Franz Pfeiffer for mentoring my thesis.

I gratefully acknowledge the funding received from the TUM International Graduate School of Science and Engineering (IGSSE) within the project PreDiQure. I would like to send my special thanks to all collaborators within this project. I am grateful to Prof. Katja Schenke-Layland and especially Eva for showing me Raman microspectroscopy and sharing their knowledge with me. Furthermore, I would like to thank Prof. Rainer Burgkart and his biomechanical labteam, especially Peter, Jan and Fiona, for introducing me into biomechanics and helping me with my small bony tokens. Additionally, I am also very grateful for the possibility to stay abroad in the group of Prof. Antonella Motta. Thank you for very much for letting me be a part of your group. A big grazie mille to Devid and Walter, who showed me how tricky fibroin can be. Thanks for the discussions, explanations and nice talks also besides the work-related stuff. Also, I would like to thank the other lab members - Silvia, Francesca, Sophia, Susan, Rosa and Alessio - for the great time in Italy. Thanks for the chatting and aperitivo after work.

Last but not least, a super big thank you to all the past and present TraumaLab members. Especially, Anna, Fritz, Laura, Marc, Marina, Sònia, Paul and Sonja. Thanks for the great support, discussions and the nice evenings together (#Hashtag).

A. Appendix

A.1. Table of Materials

Table A.1.: Table of used materials part I

Name	Catalogue number	Company
Anti-hsa-miR-100-5p miScript miRNA Inhibitor (1nmol)	219300 MIN0000098	Qiagen, Hilden, Germany
Anti-hsa-miR-1-3p miScript miRNA Inhibitor (1nmol)	219300 MIN0000146	Qiagen, Hilden, Germany
Aqua ad iniectabilia	95284	Sigma-Aldrich, St. Louis, MO, USA
Ascorbic acid	A8960 CAS 113170-55-1	Sigma-Aldrich, St. Louis, MO, USA
Cell culture flask	0030712021	Eppendorf AG, Hamburg, Germany
Chloroform	6340.1 CAS 67-66-3	Carl Roth, Karlsruhe, Germany
DMSO	4720.2 CAS 67-68-5	Carl Roth, Karlsruhe, Germany
Dulbecco's modified Eagle's Medium Low Glucose with L-Glutamine	D6046	Sigma-Aldrich, St. Louis, MO, USA
Dulbecco's Phosphate Buffered saline (PBS)	D8537	Sigma-Aldrich, St. Louis, MO, USA
EDTA	E5134 CAS 6381-92-6	Sigma-Aldrich, St. Louis, MO, USA
First Strand cDNA Synthesis Kit	K1612	Thermo Fisher Scientific, Waltham, Massachusetts, USA
Formaldehyde 37 %	4979.1 CAS 50-00-0	Carl Roth, Karlsruhe, Germany
HiPerFect Transfection Reagent	301705	Qiagen, Hilden, Germany
Hs_miR-100_1 miScript Primer Assay	218300 MS00003388	Qiagen, Hilden, Germany
Hs_SNORD96A_11 miScript Primer Assay	218300 MS00033733	Qiagen, Hilden, Germany
Iodine	207772 CAS 7553-56-2	Sigma-Aldrich, St. Louis, MO, USA

Table A.2.: Table of used materials part II

Name	Catalogue number	Company
Isopropanol	563935 CAS 67-63-0	Sigma-Aldrich, St. Louis, MO, USA
Lugol's iodine	-	prepared by the pharmacy of the university hospital
Methanol	322415 CAS 67-56-1	Sigma-Aldrich, St. Louis, MO, USA
miScript II RT Kit	218161	Qiagen, Hilden, Germany
miScript SYBR Green PCR Kit	218073	Qiagen, Hilden, Germany
miScript inhibitor negative Control (5 nmol)	1027271	Qiagen, Hilden, Germany
Natriumacetat	S8750-250G CAS 127-09-3	Sigma-Aldrich, St. Louis, MO, USA
Natriumazid	S20002 CAS 26628-22-8	Sigma-Aldrich, St. Louis, MO, USA
Natriumhydroxid	K021.1 CAS 1310-73-2	Carl Roth, Karlsruhe, Germany
Natriumphosphat dibasic	S7907-500G CAS 7558-79-4	Sigma-Aldrich, St. Louis, MO, USA
Natriumpyruvat solution	S8636 CAS 113-24-6	Sigma-Aldrich, St. Louis, MO, USA
Neverwet Multi Purpose Kit	74232	Rust Oleum, Vernon Hills, Ill, USA
Plate 48-well	0030712021	Eppendorf AG, Hamburg, Germany
Plate 96-well	781366	BRAND GMBH + CO KG Wertheim, Germany
Penicilin / Streptomycin	P0781	Sigma-Aldrich, St. Louis, MO, USA
Quant-iT PicoGreen dsDNA Assay Kit	P11496	Thermos Fisher Scientific, Waltham, Massachusetts, USA
SsoFast EvaGreen Supermix	172-5202	Bio-Rad Laboratries, California, USA
Syn-hsa-miR-1-3p miScript miRNA Mimic (1nmol)	MSY0000416	Qiagen, Hilden, Germany
Purified water	0082479E	B.Braun, Melsungen, Germany
Tri Reagent	T9424-200ml	Sigma-Aldrich, St. Louis, MO, USA
Triton-X-100	3051.2	Carl Roth, Karlsruhe, Germany
Trypan blue	L6323 CAS 72-57-1	Biochrom, Berlin, Germany
Trypsin-EDTA	T4174-100ml	Sigma-Aldrich, St. Louis, MO, USA

A.2. Statistical analysis performed for Raman spectroscopy

Table A.3.: Values of significance analysis of the absolute peak heights in the lipid Raman spectrum. Significant values are marked as described in Tab. 3.8.

Band [cm^{-1}]	osteoporotic to osteopenic	osteoporotic to healthy	osteopenic to healthy
868	0.0604	0.6208	0.9433
1079	0.1738	>0.9999	0.5521
1300	0.2676	0.7765	>0.9999
1440	0.5741	>0.9999	>0.9999
1495	>0.9999	0.0348 (*)	0.0351 (*)
1656	0.5980	>0.9999	>0.9999

Table A.4.: Values of significance analysis of the absolute peak heights in the HA Raman spectrum. Significant values are marked as described in Tab. 3.8.

Band [cm^{-1}]	osteoporotic to osteopenic	osteoporotic to healthy	osteopenic to healthy
960	>0.9999	>0.9999	>0.9999
1070	>0.9999	>0.9999	>0.9999
1450	>0.9999	>0.9999	0.6481
1495	0.3240	0.0194 (*)	0.6481

Table A.5.: Values of significance analysis of the relative peak heights for the lipid Raman spectrum peaks to the bone mineral peak ($960\,cm^{-1}$). Significant values are marked as described in Tab. 3.8.

Band [cm^{-1}]	osteoporotic to osteopenic	osteoporotic to healthy	osteopenic to healthy
868	0.3808	>0.9999	0.6353
1079	0.2084	0.9573	>0.9999
1300	0.2548	>0.9999	0.6481
1440	0.2486	>0.9999	0.8942
1495	>0.9999	0.1887	0.4545
1656	0.7862	>0.9999	0.4260

Table A.6.: Values of significance analysis of the relative peak heights for the HA Raman spectrum peaks to the bone mineral peak (960 cm^{-1}). Significant values are marked as described in Tab. 3.8.

Band [cm^{-1}]	osteoporotic to osteopenic	osteoporotic to healthy	osteopenic to healthy
1070	>0.9999	0.1185	0.4451
1450	>0.9999	>0.9999	0.7010
1495	0.2675	0.0852	>0.9999

Table A.7.: Values of significance analysis of the relative peak heights in the lipid Raman spectrum to the amide I peak (1655 cm^{-1}). Significant values are marked as described in Tab. 3.8.

Band [cm^{-1}]	osteoporotic to osteopenic	osteoporotic to healthy	osteopenic to healthy
868	0.4854	0.6208	>0.9999
1079	0.2548	0.3798	>0.9999
1300	0.6875	0.8637	>0.9999
1440	0.4165	0.3327	>0.9999
1495	>0.9999	0.2187	0.0470 (*)

Table A.8.: Values of significance analysis of the relative peak heights in the HA Raman spectrum to the amide I peak (1655 cm^{-1}). Significant values are marked as described in Tab. 3.8.

Band [cm^{-1}]	osteoporotic to osteopenic	osteoporotic to healthy	osteopenic to healthy
1070	0.3984	>0.9999	>0.9999
1450	0.6875	0.8637	>0.9999
1495	0.6353	0.0104 (*)	0.2138

Table A.9.: Values of significance analysis of the correlation between absolute and relative peak heights of Raman spectroscopy and BMD. Significant values are marked as described in Tab. 3.8.

Band or ratio of bands [cm^{-1}]	Spearman coefficient r	p-value
868	0.3043	0.2501
1079	0.3634	0.1662
1300	0.2969	0.2622
1440	0.2068	0.4393
1495	0.7016	0.0032 (**)
1656	0.1344	0.6174
960	0.2925	0.2697
1070	0.07386	0.7852
1450	-0.04284	0.8753
1495	0.6795	0.0048 (**)
868/960	-0.007386	0.9802
1079/960	0.1625	0.5451
1300/960	0.06942	0.7979
1440/960	0.1196	0.6570
1495/960	0.4269	0.1001
1656/960	-0.06352	0.8150
1070/960	-0.4697	0.0680
1450/960	-0.1876	0.4837
1495/960	0.4727	0.0661
868/1656	0.2186	0.4131
1079/1656	0.2038	0.4460
1300/1656	0.1182	0.6611
1440/1656	0.2629	0.3227
1495/1656	0.3855	0.1404
1070/1656	-0.229	0.3908
1450/1656	-0.2762	0.2981
1495/1656	0.7238	0.0021 (**)

Table A.10.: Values of significance analysis of the correlation between absolute and relative peak heights of Raman spectroscopy and BMD $<0.2\,\mathrm{g\,cm^{-3}}$. Significant values are marked as described in Tab. 3.8.

Band or ratio of bands [$\mathrm{cm^{-1}}$]	Spearman coefficient r	p-value
868	0.6737	0.0191 (*)
1079	0.6949	0.0146 (*)
1300	0.6949	0.0146 (*)
1440	0.6173	0.0358 (*)
1495	0.3386	0.2797
1656	0.5926	0.0456 (*)
960	-0.007055	0.9863
1070	-0.05997	0.8552
1450	0.08113	0.8034
1495	0.642	0.0274 (*)
868/960	0.5044	0.0971
1079/960	0.6314	0.0309 (*)
1300/960	0.6173	0.0358 (*)
1440/960	0.61632	0.0216 (*)
1495/960	0.254	0.4227
1656/960	0.5997	0.0426 (*)
1070/960	-0.4057	0.1909
1450/960	0.0776	0.8110
1495/960	0.5715	0.0555
868/1656	0.2575	0.4165
1079/1656	0.3527	0.2591
1300/1656	0.3386	0.2797
1440/1656	0.4621	0.1321
1495/1656	-0.187	0.5587
1070/1656	-0.6173	0.0358 (*)
1450/1656	-0.5115	0.0919
1495/1656	0.4974	0.1024

A.3. PCR Results of the samples collected after the transfection experiment (controls)

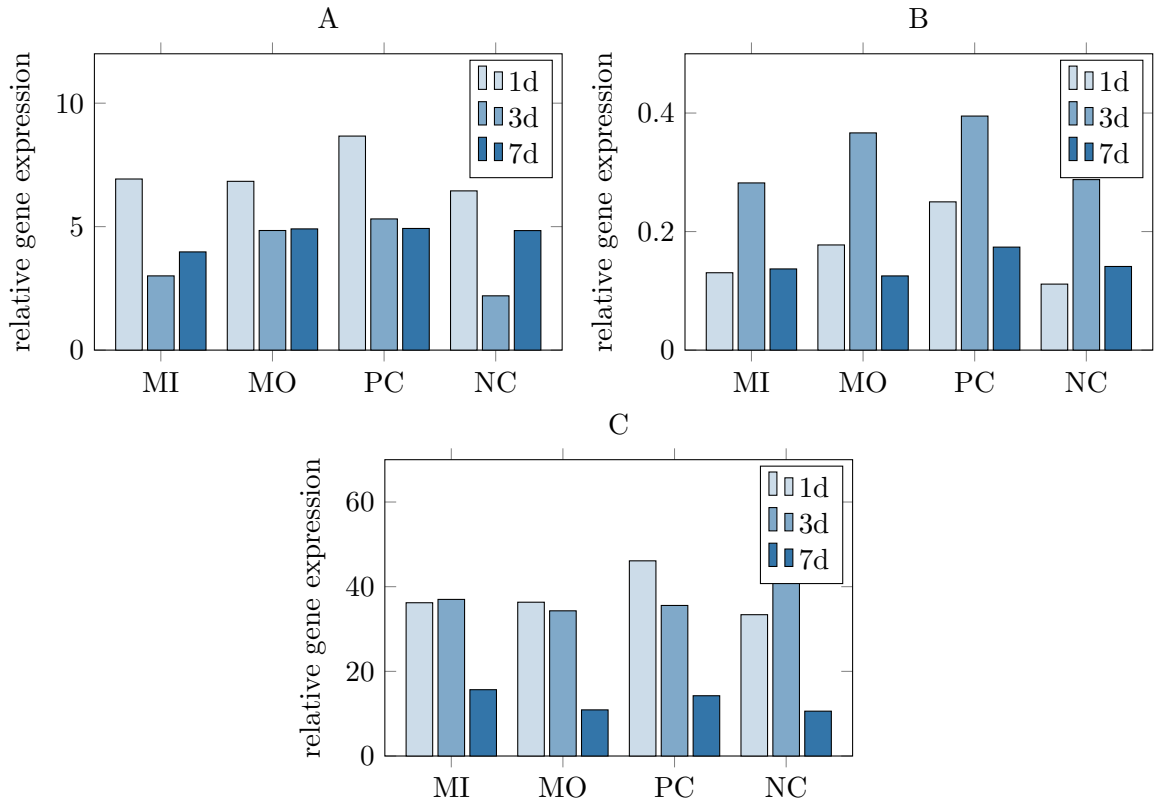

Figure A.1.: Relative expression levels of the controls for miR-100-5-p (A), for BMPR2 (B) and for Collagen Type I (C). Values are normalized to SNORD96a and expressed as $2^{\Delta C_T}$. The used controls are transfected cells with miR-1 mimic (MI), only the transfection reagent (MO), a positive control (PC), which is a co-transfection of mimic and inhibitor of miR-1, and a negative control (NC), which had no homology sequence to any known mammalian gene.

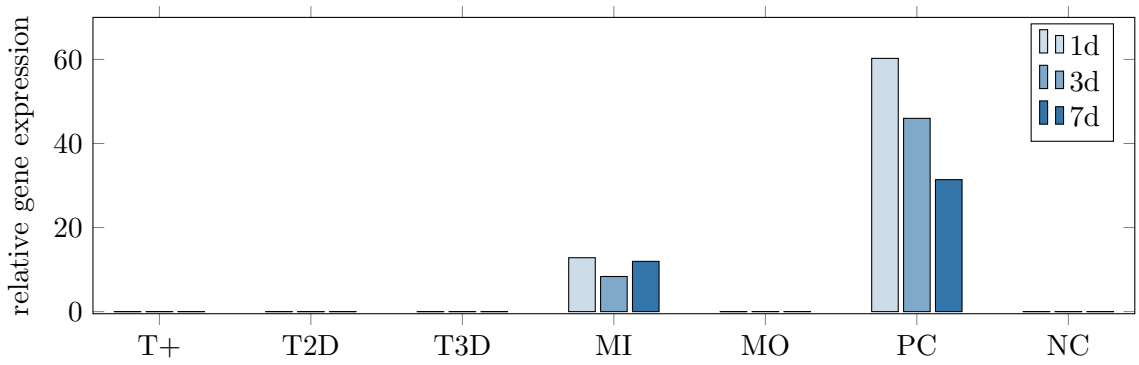

Figure A.2.: Relative expression levels of miR-1 of the miR-100-5p inhibited cells (T+), the untransfected cells in 2d (T2D) and in 3D (T3D). Values are normalized to SNORD96a and expressed as $2^{\Delta C_T}$. The used controls are transfected cells with miR-1 mimic (MI), only the transfection reagent (MO), a positive control (PC), which is a co-transfection of mimic and inhibitor of miR-1, and a negative control (NC), which had no homology sequence to any known mammalian gene.

A.4. Permission request

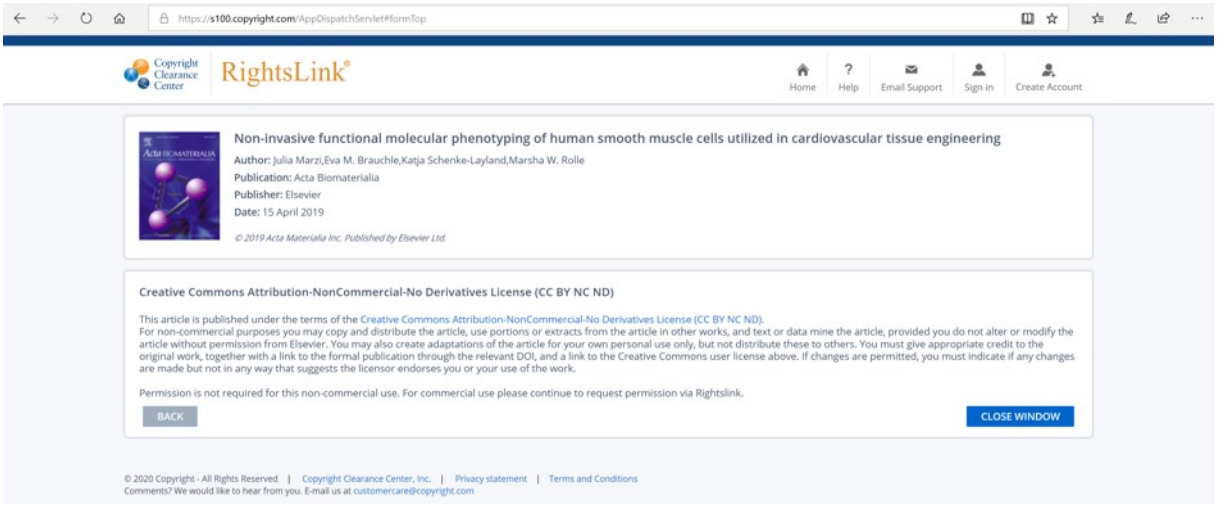

Figure A.3.: Permission request for modified figure by Marzi et al. [108].

Bibliography

[1] G. Albrand, F. Munoz, E. Sornay-Rendu, F. DuBoeuf, and P. D. Delmas. "Independent predictors of all osteoporosis-related fractures in healthy postmenopausal women: The OFELY Study". In: *Bone* 32.1 (2003), pp. 78–85. DOI: 10.1016/S8756-3282(02)00919-5.

[2] G. H. Altman, F. Diaz, C. Jakuba, T. Calabro, R. L. Horan, J. Chen, H. Lu, J. Richmond, and D. L. Kaplan. "Silk-based biomaterials". In: *Biomaterials* 24.3 (2003), pp. 401–16. DOI: 10.1016/s0142-9612(02)00353-8.

[3] I. Alvarez-Garcia and E. A. Miska. "MicroRNA functions in animal development and human disease". In: *Development* 132.21 (2005), pp. 4653–62. DOI: 10.1242/dev.02073.

[4] M. A. Arriaga, M. H. Ding, A. S. Gutierrez, and S. A. Chew. "The Application of microRNAs in Biomaterial Scaffold-Based Therapies for Bone Tissue Engineering". In: *Biotechnology Journal* 14.10 (2019), p. 1900084. DOI: 10.1002/biot.201900084.

[5] R. B. Ashman, J. D. Corin, and C. H. Turner. "Elastic properties of cancellous bone: measurement by an ultrasonic technique". In: *J Biomech* 20.10 (1987), pp. 979–86.

[6] C. Backes, E. Meese, and A. Keller. "Specific miRNA Disease Biomarkers in Blood, Serum and Plasma: Challenges and Prospects". In: *Mol Diagn Ther* 20.6 (2016), pp. 509–518. DOI: 10.1007/s40291-016-0221-4.

[7] Y. Z. Bagger, L. B. Tankó, P. Alexandersen, H. B. Hansen, G. Qin, and C. Christiansen. "The long-term predictive value of bone mineral density measurements for fracture risk is independent of the site of measurement and the age at diagnosis: results from the Prospective Epidemiological Risk Factors study". In: *Osteoporosis International* 17.3 (2006), pp. 471–477. DOI: 10.1007/s00198-005-0009-6.

[8] K. Balzer, M. Bremer, S. Schramm, D. Lühmann, and H. Raspe. "Sturzprophylaxe bei älteren Menschen in ihrer persönlichen Wohnumgebung: Ethisch-soziale Implikationen vor dem Hintergrund klinischer und gesundheitsökonomischer Effektivität". In: *Gesundheitswesen* 72.08/09 (2012), p. V190. DOI: 10.1055/s-0030-1266371.

[9] D. P. Bartel. "Metazoan MicroRNAs". In: *Cell* 173.1 (2018), pp. 20–51. DOI: 10.1016/j.cell.2018.03.006.

[10] D. P. Bartel. "MicroRNAs: genomics, biogenesis, mechanism, and function". In: *Cell* 116.2 (2004), pp. 281–97. DOI: 10.1016/s0092-8674(04)00045-5.

[11] D. Bellavia, F. Salamanna, L. Raimondi, A. De Luca, V. Carina, V. Costa, R. Alessandro, M. Fini, and G. Giavaresi. "Deregulated miRNAs in osteoporosis: effects in bone metastasis". In: *Cell Mol Life Sci* (2019). DOI: 10.1007/s00018-019-03162-w.

[12] B. C. Bernardo, J. Y. Ooi, R. C. Lin, and J. R. McMullen. "miRNA therapeutics: a new class of drugs with potential therapeutic applications in the heart". In: *Future Med Chem* 7.13 (2015), pp. 1771–92. DOI: 10.4155/fmc.15.107.

[13] I. V. Bessonov et al. "Fabrication of hydrogel scaffolds via photocrosslinking of methacrylated silk fibroin". In: *Biomed Mater* 14.3 (2019), p. 034102. DOI: 10.1088/1748-605X/ab04e0.

[14] J. P. Bonjour, P. Ammann, and R. Rizzoli. "Importance of preclinical studies in the development of drugs for treatment of osteoporosis: a review related to the 1998 WHO guidelines". In: *Osteoporos Int* 9.5 (1999), pp. 379–93. DOI: 10.1007/s001980050161.

[15] C. H. Bow, S. W. Y. Tsang, C. H. N. Loong, C. S. S. Soong, S. C. Yeung, and A. W. C. Kung. "Bone mineral density enhances use of clinical risk factors in predicting ten-year risk of osteoporotic fractures in Chinese men: the Hong Kong Osteoporosis Study". In: *Osteoporosis International* 22.11 (2011), pp. 2799–2807. DOI: 10.1007/s00198-010-1490-0.

[16] E. Brauchle, D. Carvajal Berrio, M. Rieger, K. Schenke-Layland, S. Reinert, and D. Alexander. "Raman Spectroscopic Analyses of Jaw Periosteal Cell Mineralization". In: *Stem Cells Int* 2017 (2017), p. 1651376. DOI: 10.1155/2017/1651376.

[17] Brucker. "An overview of NRecon: reconstructing the best images from your microCT scan (MN062)". In: *Bruker microCT method note* (2014).

[18] Brucker. "CTAn: The externally edited image from ROI (allows multiple ROI shapes)". In: *Bruker microCT method note* (2005).

[19] G. B. Cardoso, D. Maniglio, F. Z. Volpato, A. Tondon, C. Migliaresi, R. R. Kaunas, and C. A. Zavaglia. "Oleic acid surfactant in polycaprolactone/hydroxyapatite-composites for bone tissue engineering". In: *J Biomed Mater Res B Appl Biomater* 104.6 (2016), pp. 1076–82. DOI: 10.1002/jbm.b.33457.

[20] D. R. Carter and W. C. Hayes. "Compact bone fatigue damage: a microscopic examination". In: *Clin Orthop Relat Res* 127 (1977), pp. 265–74.

[21] D. R. Carter and W. C. Hayes. "The compressive behavior of bone as a two-phase porous structure". In: *J Bone Joint Surg Am* 59.7 (1977), pp. 954–62.

[22] R. W. Carthew and E. J. Sontheimer. "Origins and Mechanisms of miRNAs and siRNAs". In: *Cell* 136.4 (2009), pp. 642–55. DOI: 10.1016/j.cell.2009.01.035.

[23] J. R. Center, D. Bliuc, T. V. Nguyen, and J. A. Eisman. "Risk of Subsequent Fracture After Low-Trauma Fracture in Men and Women". In: *JAMA* 297.4 (2007), pp. 387–394. DOI: 10.1001/jama.297.4.387.

[24] R. Cesar, R. S. Boffa, L. T Fachine, T. P. Leivas, A. M. H. Silva, C. A. M. Pereira, R. B. M. Reiff, and J. M. D. A. Rollo. "Evaluation of trabecular microarchitecture of normal osteoporotic and osteopenic human vertebrae". In: *Procedia Engineering* 59 (2013), pp. 6–15. DOI: 10.1016/j.proeng.2013.05.087.

[25] D. Chappard, M. F. Basle, E. Legrand, and M. Audran. "New laboratory tools in the assessment of bone quality". In: *Osteoporos Int* 22.8 (2011), pp. 2225–40. DOI: 10.1007/s00198-011-1573-6.

[26] D. Chappard, E. Legrand, B. Haettich, G. Chales, B. Auvinet, J. P. Eschard, J. P. Hamelin, M. F. Basle, and M. Audran. "Fractal dimension of trabecular bone: comparison of three histomorphometric computed techniques for measuring the architectural two-dimensional complexity". In: *J Pathol* 195.4 (2001), pp. 515–21. DOI: 10.1002/path.970.

[27] R. D. Chapurlat, D. C. Bauer, M. Nevitt, K. Stone, and S. R. Cummings. "Incidence and risk factors for a second hip fracture in elderly women. The Study of Osteoporotic Fractures". In: *Osteoporosis International* 14.2 (2003), pp. 130–136. DOI: 10.1007/s00198-002-1327-6.

[28] L. X. Chen, Z. R. Zhou, Y. L. Li, G. Z. Ning, T. S. Zhang, D. Zhang, and S. Q. Feng. "Comparison of Bone Mineral Density in Lumbar Spine and Fracture Rate among Eight Drugs in Treatments of Osteoporosis in Men: A Network Meta-Analysis". In: *PLoS One* 10.5 (2015), e0128032. DOI: 10.1371/journal.pone.0128032.

[29] Z. Chen, M. G. Bemben, and D. A. Bemben. "Bone and muscle specific circulating microRNAs in postmenopausal women based on osteoporosis and sarcopenia status". In: *Bone* 120 (2019), pp. 271–278. DOI: 10.1016/j.bone.2018.11.001.

[30] X. Cheng, Y. Niu, Q. Ding, X. Yin, G. Huang, J. Peng, and J. Song. "Cadmium Exposure and Risk of Any Fracture: A PRISMA-Compliant Systematic Review and Meta-Analysis". In: *Medicine* 95.10 (2016), e2932–e2932. DOI: 10.1097/MD.0000000000002932.

[31] C.-L. Cheung, K. C. B. Tan, C. H. Bow, C. S. S. Soong, C. H. N. Loong, and A. W.-C. Kung. "Low handgrip strength is a predictor of osteoporotic fractures: cross-sectional and prospective evidence from the Hong Kong Osteoporosis Study". In: *AGE* 34.5 (2012), pp. 1239–1248. DOI: 10.1007/s11357-011-9297-2.

[32] C. S. Chon, H. S. Yun, H. S. Kim, and C. Ko. "Elastic Modulus of Osteoporotic Mouse Femur Based on Femoral Head Compression Test". In: *Appl Bionics Biomech* 2017 (2017), p. 7201769. DOI: 10.1155/2017/7201769.

[33] S. P. Chu, J. L. Kelsey, T. H. M. Keegan, B. Sternfeld, M. Prill, C. P. Quesenberry, and S. Sidney. "Risk Factors for Proximal Humerus Fracture". In: *American Journal of Epidemiology* 160.4 (2004), pp. 360–367. DOI: 10.1093/aje/kwh224.

[34] C. Colón-Emeric, M. Kuchibhatla, C. Pieper, W. Hawkes, L. Fredman, J. Magaziner, S. Zimmerman, and K. W. Lyles. "The contribution of hip fracture to risk of subsequent fractures: data from two longitudinal studies". In: *Osteoporosis International* 14.11 (2003), pp. 879–883. DOI: 10.1007/s00198-003-1460-x.

[35] M. T. Cuddihy, S. E. Gabriel, C. S. Crowson, W. M. O'Fallon, and L. J. Melton Iii. "Forearm Fractures as Predictors of Subsequent Osteoporotic Fractures". In: *Osteoporosis International* 9.6 (1999), pp. 469–475. DOI: 10.1007/s001980050172.

[36] W. Q. Cui, Y. Y. Won, M. H. Baek, D. H. Lee, Y. S. Chung, J. H. Hur, and Y. Z. Ma. "Age-and region-dependent changes in three-dimensional microstructural properties of proximal femoral trabeculae". In: *Osteoporos Int* 19.11 (2008), pp. 1579–87. DOI: 10.1007/s00198-008-0601-7.

[37] S. R. Cummings, M. C. Nevitt, W. S. Browner, K. Stone, K. M. Fox, K. E. Ensrud, J. Cauley, D. Black, and T. M. Vogt. "Risk Factors for Hip Fracture in White Women". In: *New England Journal of Medicine* 332.12 (1995), pp. 767–773. DOI: 10.1056/nejm199503233321202.

[38] M. Cuppone, B. B. Seedhom, E. Berry, and A. E. Ostell. "The longitudinal Young's modulus of cortical bone in the midshaft of human femur and its correlation with CT scanning data". In: *Calcified tissue international* 74.3 (2004), pp. 302–309. DOI: 10.1007/s00223-002-2123-1.

[39] J. Currey. "Measurement of the mechanical properties of bone: a recent history". In: *Clin Orthop Relat Res* 467.8 (2009), pp. 1948–54. DOI: 10.1007/s11999-009-0784-z.

[40] E. Curtis, A. Litwic, C. Cooper, and E. Dennison. "Determinants of Muscle and Bone Aging". In: *J Cell Physiol* 230.11 (2015), pp. 2618–25. DOI: 10.1002/jcp.25001.

[41] E. Donnelly, S. P. Baker, A. L. Boskey, and M. C. van der Meulen. "Effects of surface roughness and maximum load on the mechanical properties of cancellous bone measured by nanoindentation". In: *J Biomed Mater Res A* 77.2 (2006), pp. 426–35. DOI: 10.1002/jbm.a.30633.

[42] E. R. Draper, M. D. Morris, N. P. Camacho, P. Matousek, M. Towrie, A. W. Parker, and A. E. Goodship. "Novel assessment of bone using time-resolved transcutaneous Raman spectroscopy". In: *J Bone Miner Res* 20.11 (2005), pp. 1968–72. DOI: 10.1359/jbmr.050710.

[43] DVO. *Prophylaxe, Diagnostik und Therapie der Osteoporose bei postmenopausalen Frauen und bei Männern: Leitlinie.* Dachverband der Deutschsprachigen Wissenschaftlichen Osteologischen Gesellschaft e.V., 2017.

[44] F. Eklund, A. Nordström, U. Björnstig, and P. Nordström. "Bone mass, size and previous fractures as predictors of prospective fractures in an osteoporotic referral population". In: *Bone* 45.4 (2009), pp. 808–813. DOI: 10.1016/j.bone.2009.06.024.

[45] W. H. Elliott, W. Bonani, D. Maniglio, A. Motta, W. Tan, and C. Migliaresi. "Silk Hydrogels of Tunable Structure and Viscoelastic Properties Using Different Chronological Orders of Genipin and Physical Cross-Linking". In: *ACS Appl Mater Interfaces* 7.22 (2015), pp. 12099–108. DOI: 10.1021/acsami.5b02308.

[46] M. Esteller. "Non-coding RNAs in human disease". In: *Nat Rev Genet* 12.12 (2011), pp. 861–74. DOI: 10.1038/nrg3074.

[47] M. Farokhi, F. Mottaghitalab, S. Samani, M. A. Shokrgozar, S. C. Kundu, R. L. Reis, Y. Fatahi, and D. L. Kaplan. "Silk fibroin/hydroxyapatite composites for bone tissue engineering". In: *Biotechnology Advances* 36.1 (2018), pp. 68–91. DOI: 10.1016/j.biotechadv.2017.10.001.

[48] X. Feichtinger et al. "Bone-related Circulating MicroRNAs miR-29b-3p, miR-550a-3p, and miR-324-3p and their Association to Bone Microstructure and Histomorphometry". In: *Sci Rep* 8.1 (2018), p. 4867. DOI: 10.1038/s41598-018-22844-2.

[49] J. S. Finkelstein, A. Hayes, J. L. Hunzelman, J. J. Wyland, H. Lee, and R. M. Neer. "The Effects of Parathyroid Hormone, Alendronate, or Both in Men with Osteoporosis". In: *New England Journal of Medicine* 349.13 (2003), pp. 1216–1226. DOI: 10.1056/NEJMoa035725.

[50] M. Floren, W. Bonani, A. Dharmarajan, A. Motta, C. Migliaresi, and W. Tan. "Human mesenchymal stem cells cultured on silk hydrogels with variable stiffness and growth factor differentiate into mature smooth muscle cell phenotype". In: *Acta Biomater* 31 (2016), pp. 156–166. DOI: 10.1016/j.actbio.2015.11.051.

[51] S. Font Tellado, W. Bonani, E. R. Balmayor, P. Foehr, A. Motta, C. Migliaresi, and M. van Griensven. "(*) Fabrication and Characterization of Biphasic Silk Fibroin Scaffolds for Tendon/Ligament-to-Bone Tissue Engineering". In: *Tissue Eng Part A* 23.15-16 (2017), pp. 859–872. DOI: 10.1089/ten.TEA.2016.0460.

[52] S. Font Tellado, S. Chiera, W. Bonani, P. S. P. Poh, C. Migliaresi, A. Motta, E. R. Balmayor, and M. van Griensven. "Heparin functionalization increases retention of TGF-beta2 and GDF5 on biphasic silk fibroin scaffolds for tendon/ligament-to-bone tissue engineering". In: *Acta Biomater* 72 (2018), pp. 150–166. DOI: 10.1016/j.actbio.2018.03.017.

[53] C. Foss, E. Merzari, C. Migliaresi, and A. Motta. "Silk fibroin/hyaluronic acid 3D matrices for cartilage tissue engineering". In: *Biomacromolecules* 14.1 (2013), pp. 38–47. DOI: 10.1021/bm301174x.

[54] S. Gamsjaeger, B. Hofstetter, E. Zwettler, R. Recker, J. A. Gasser, E. F. Eriksen, K. Klaushofer, and E. P. Paschalis. "Effects of 3 years treatment with once-yearly zoledronic acid on the kinetics of bone matrix maturation in osteoporotic patients". In: *Osteoporos Int* 24.1 (2013), pp. 339–47. DOI: 10.1007/s00198-012-2202-8.

[55] T. Golombick and T. Diamond. "Prevalence of monoclonal gammopathy of undetermined significance/myeloma in patients with acute osteoporotic vertebral fractures". In: *Acta Haematol* 120.2 (2008), pp. 87–90. DOI: 10.1159/000162282.

[56] A. V. Goncharenko, N. V. Malyuchenko, A. M. Moisenovich, M. S. Kotlyarova, A. Y. Arkhipova, A. S. Kon'kov, II Agapov, A. V. Molochkov, M. M. Moisenovich, and M. P. Kirpichnikov. "Changes in morphology of actin filaments and expression of alkaline phosphatase at 3D cultivation of MG-63 osteoblast-like cells on mineralized fibroin scaffolds". In: *Dokl Biochem Biophys* 470.1 (2016), pp. 368–370. DOI: 10.1134/S1607672916050197.

[57] B. Gong, G. S. Mandair, F. W. Wehrli, and M. D. Morris. "Novel assessment tools for osteoporosis diagnosis and treatment". In: *Curr Osteoporos Rep* 12.3 (2014), pp. 357–65. DOI: 10.1007/s11914-014-0215-2.

[58] P. Graves and Y. Zeng. "Biogenesis of mammalian microRNAs: a global view". In: *Genomics Proteomics Bioinformatics* 10.5 (2012), pp. 239–45. DOI: 10.1016/j.gpb.2012.06.004.

[59] C. Greenwood, J. G. Clement, A. J. Dicken, J. P. Evans, I. D. Lyburn, R. M. Martin, K. D. Rogers, N. Stone, G. Adams, and P. Zioupos. "The micro-architecture of human cancellous bone from fracture neck of femur patients in relation to the structural integrity and fracture toughness of the tissue". In: *Bone Rep* 3 (2015), pp. 67–75. DOI: 10.1016/j.bonr.2015.10.001.

[60] A. S. Haka, K. E. Shafer-Peltier, M. Fitzmaurice, J. Crowe, R. R. Dasari, and M. S. Feld. "Identifying microcalcifications in benign and malignant breast lesions by probing differences in their chemical composition using Raman spectroscopy". In: *Cancer Res* 62.18 (2002), pp. 5375–80.

[61] R. Hambli. "Micro-CT finite element model and experimental validation of trabecular bone damage and fracture". In: *Bone* 56.2 (2013), pp. 363–74. DOI: 10.1016/j.bone.2013.06.028.

[62] M. T. Hannan, D. T. Felson, and J. J. Anderson. "Bone mineral density in elderly men and women: results from the Framingham osteoporosis study". In: *J Bone Miner Res* 7.5 (1992), pp. 547–53. DOI: 10.1002/jbmr.5650070511.

[63] L. He and G. J. Hannon. "MicroRNAs: small RNAs with a big role in gene regulation". In: *Nat Rev Genet* 5.7 (2004), pp. 522–31. DOI: 10.1038/nrg1379.

[64] National institute of health. "Osteoporosis prevention, diagnosis, and therapy". In: *NIH Consens Statement* 17.1 (2000), pp. 1–45.

[65] P. Heimel, N. V. Swiadek, P. Slezak, M. Kerbl, C. Schneider, S. Nurnberger, H. Redl, A. H. Teuschl, and D. Hercher. "Iodine-Enhanced Micro-CT Imaging of Soft Tissue on the Example of Peripheral Nerve Regeneration". In: *Contrast Media Mol Imaging* 2019 (2019), p. 7483745. DOI: 10.1155/2019/7483745.

[66] E. J. Hoorn, F. Rivadeneira, J. BJ van Meurs, G. Ziere, B. H. Stricker, A. Hofman, H. A. Pols, R. Zietse, A. G Uitterlinden, and M. C. Zillikens. "Mild hyponatremia as a risk factor for fractures: The rotterdam study". In: *Journal of Bone and Mineral Research* 26.8 (2011), pp. 1822–1828. DOI: 10.1002/jbmr.380.

[67] A. Icks, B. Haastert, M. Wildner, C. Becker, and G. Meyer. "Trend of hip fracture incidence in Germany 1995–2004: a population-based study". In: *Osteoporosis international* 19.8 (2008), pp. 1139–1145.

[68] K. Inoue et al. "Bone protection by inhibition of microRNA-182". In: *Nat Commun* 9.1 (2018), p. 4108. DOI: 10.1038/s41467-018-06446-0.

[69] A. A. Ismail, A. J. Silman, J. Reeve, S. Kaptoge, and T. W. O'Neill. "Rib fractures predict incident limb fractures: results from the European prospective osteoporosis study". In: *Osteoporosis International* 17.1 (2006), pp. 41–45. DOI: 10.1007/s00198-005-1887-3.

[70] N. S. Jeffery, R. S. Stephenson, J. A. Gallagher, J. C. Jarvis, and P. G. Cox. "Micro-computed tomography with iodine staining resolves the arrangement of muscle fibres". In: *J Biomech* 44.1 (2011), pp. 189–92. DOI: 10.1016/j.jbiomech.2010.08.027.

[71] R. R. Jones, D. C. Hooper, L. Zhang, D. Wolverson, and V. K. Valev. "Raman Techniques: Fundamentals and Frontiers". In: *Nanoscale Res Lett* 14.1 (2019), p. 231. DOI: 10.1186/s11671-019-3039-2.

[72] C. Jud et al. "Trabecular bone anisotropy imaging with a compact laser-undulator synchrotron x-ray source". In: *Sci Rep* 7.1 (2017), p. 14477. DOI: 10.1038/s41598-017-14830-x.

[73] R. J. Kane, H. E. Weiss-Bilka, M. J. Meagher, Y. Liu, J. A. Gargac, G. L. Niebur, D. R. Wagner, and R. K. Roeder. "Hydroxyapatite reinforced collagen scaffolds with improved architecture and mechanical properties". In: *Acta Biomater* 17 (2015), pp. 16–25. DOI: 10.1016/j.actbio.2015.01.031.

[74] J. A. Kanis et al. "A meta-analysis of previous fracture and subsequent fracture risk". In: *Bone* 35.2 (2004), pp. 375–382. DOI: 10.1016/j.bone.2004.03.024.

[75] F. Katsamanis and D. D. Raftopoulos. "Determination of mechanical properties of human femoral cortical bone by the Hopkinson bar stress technique". In: *J Biomech* 23.11 (1990), pp. 1173–84. DOI: 10.1016/0021-9290(90)90010-Z.

[76] J. M. Kaufman, E. Orwoll, S. Goemaere, J. San Martin, A. Hossain, G. P. Dalsky, R. Lindsay, and B. H. Mitlak. "Teriparatide effects on vertebral fractures and bone mineral density in men with osteoporosis: treatment and discontinuation of therapy". In: *Osteoporosis International* 16.5 (2005), pp. 510–516. DOI: 10.1007/s00198-004-1713-3.

[77] S. Kelch, E. R. Balmayor, C. Seeliger, H. Vester, J. S. Kirschke, and M. van Griensven. "miRNAs in bone tissue correlate to bone mineral density and circulating miRNAs are gender independent in osteoporotic patients". In: *Sci Rep* 7.1 (2017), p. 15861. DOI: 10.1038/s41598-017-16113-x.

[78] T. S. Keller, Z. Mao, and D. M. Spengler. "Young's modulus, bending strength, and tissue physical properties of human compact bone". In: *J Orthop Res* 8.4 (1990), pp. 592–603. DOI: 10.1002/jor.1100080416.

[79] J. H. Kellgren and J. S. Lawrence. "Radiological Assessment of Osteo-Arthrosis". In: *Annals of the Rheumatic Diseases* 16.4 (1957), pp. 494–502. DOI: 10.1136/ard.16.4.494.

[80] M. Khalid, T. Bora, A. A. Ghaithi, S. Thukral, and J. Dutta. "Raman Spectroscopy detects changes in Bone Mineral Quality and Collagen Cross-linkage in Staphylococcus Infected Human Bone". In: *Scientific Reports* 8.1 (2018), p. 9417. DOI: 10.1038/s41598-018-27752-z.

[81] B. S. Kim, K. E. Park, M. H. Kim, H. K. You, J. Lee, and W. H. Park. "Effect of nanofiber content on bone regeneration of silk fibroin/poly(epsilon-caprolactone) nano/microfibrous composite scaffolds". In: *Int J Nanomedicine* 10 (2015), pp. 485–502. DOI: 10.2147/ijn.s72730.

[82] M. H. Kim and W. H. Park. "Chemically cross-linked silk fibroin hydrogel with enhanced elastic properties, biodegradability, and biocompatibility". In: *Int J Nanomedicine* 11 (2016), pp. 2967–78. DOI: 10.2147/ijn.s106467.

[83] S. Kinsella, S. Moran, M. O. Sullivan, M. G.M. Molloy, and J. A. Eustace. "Hyponatremia Independent of Osteoporosis is Associated with Fracture Occurrence". In: *Clinical Journal of the American Society of Nephrology* 5.2 (2010), pp. 275–280. DOI: 10.2215/cjn.06120809.

[84] H. E. Kinser and Z. Pincus. "MicroRNAs as modulators of longevity and the aging process". In: *Hum Genet* (2019). DOI: 10.1007/s00439-019-02046-0.

[85] M. van der Klift, C. E. de Laet, E. V. McCloskey, O. Johnell, J. A. Kanis, A. Hofman, and H. A. Pols. "Risk Factors for Incident Vertebral Fractures in Men and Women: The Rotterdam Study". In: *Journal of Bone and Mineral Research* 19.7 (2004), pp. 1172–1180. DOI: 10.1359/jbmr.040215.

[86] T. Komori. "Animal models for osteoporosis". In: *Eur J Pharmacol* 759 (2015), pp. 287–94. DOI: 10.1016/j.ejphar.2015.03.028.

[87] M. Kärkkäinen, T. Rikkonen, H. Kröger, J. Sirola, M. Tuppurainen, K. Salovaara, J. Arokoski, J. Jurvelin, R. Honkanen, and E. Alhava. "Association between functional capacity tests and fractures: An eight-year prospective population-based cohort study". In: *Osteoporosis International* 19.8 (2008), pp. 1203–1210. DOI: 10.1007/s00198-008-0561-y.

[88] U. H. Lerner. "Osteoblasts, osteoclasts, and osteocytes: unveiling their intimate-associated responses to applied orthodontic forces". In: *Seminars in Orthodontics*. Vol. 18. Elsevier, 2012, pp. 237–248. DOI: 10.1053/j.sodo.2012.06.0020.

[89] C. E. Lewis, S. K. Ewing, B. C. Taylor, J. M. Shikany, H. A. Fink, K. E. Ensrud, E. Barrett-Connor, S. R. Cummings, and E. Orwoll. "Predictors of Non-Spine Fracture in Elderly Men: The MrOS Study". In: *Journal of Bone and Mineral Research* 22.2 (2007), pp. 211–219. DOI: 10.1359/jbmr.061017.

[90] B. Li and R. M. Aspden. "Composition and mechanical properties of cancellous bone from the femoral head of patients with osteoporosis or osteoarthritis". In: *J Bone Miner Res* 12.4 (1997), pp. 641–51. DOI: 10.1359/jbmr.1997.12.4.641.

[91] Y. Li and K. V. Kowdley. "MicroRNAs in common human diseases". In: *Genomics Proteomics Bioinformatics* 10.5 (2012), pp. 246–53. DOI: 10.1016/j.gpb.2012.07.005.

[92] Y. Li et al. "The promotion of bone regeneration through positive regulation of angiogenic-osteogenic coupling using microRNA-26a". In: *Biomaterials* 34.21 (2013), pp. 5048–58. DOI: 10.1016/j.biomaterials.2013.03.052.

[93] Y. Liang and L. Wang. "Alzheimer's Disease is an Important Risk Factor of Fractures: a Meta-analysis of Cohort Studies". In: *Molecular Neurobiology* 54.5 (2017), pp. 3230–3235. DOI: 10.1007/s12035-016-9841-2.

[94] X. Liu and S. Harada. "RNA Isolation from Mammalian Samples". In: *Current Protocols in Molecular Biology* 103.1 (2013), pp. 4.16.1–4.16.16. DOI: 10.1002/0471142727.mb0416s103.

[95] Z. Liu, H. Chang, Y. Hou, Y. Wang, Z. Zhou, M. Wang, Z. Huang, and B. Yu. "Lentivirusmediated microRNA26a overexpression in bone mesenchymal stem cells facilitates bone regeneration in bone defects of calvaria in mice". In: *Mol Med Rep* 18.6 (2018), pp. 5317–5326. DOI: 10.3892/mmr.2018.9596.

[96] H. Lv, L. Zhang, F. Yang, Z. Zhao, Q. Yao, L. Zhang, and P. Tang. "Comparison of microstructural and mechanical properties of trabeculae in femoral head from osteoporosis patients with and without cartilage lesions: a case-control study". In: *BMC Musculoskelet Disord* 16 (2015), p. 72. DOI: 10.1186/s12891-015-0530-5.

[97] K. W. Lyles et al. "Zoledronic Acid and Clinical Fractures and Mortality after Hip Fracture". In: *New England Journal of Medicine* 357.18 (2007), pp. 1799–1809. DOI: 10.1056/NEJMoa074941.

[98] S. Majumdar, J. Lin, T. Link, J. Millard, P. Augat, X. Ouyang, D. Newitt, R. Gould, M. Kothari, and H. Genant. "Fractal analysis of radiographs: assessment of trabecular bone structure and prediction of elastic modulus and strength". In: *Med Phys* 26.7 (1999), pp. 1330–40. DOI: 10.1118/1.598628.

[99] S. Majumdar, R. S. Weinstein, and R. R. Prasad. "Application of fractal geometry techniques to the study of trabecular bone". In: *Med Phys* 20.6 (1993), pp. 1611–9. DOI: 10.1118/1.596948.

[100] R. E. Makitie, M. Hackl, R. Niinimaki, S. Kakko, J. Grillari, and O. Makitie. "Altered MicroRNA Profile in Osteoporosis Caused by Impaired WNT Signaling". In: *J Clin Endocrinol Metab* 103.5 (2018), pp. 1985–1996. DOI: 10.1210/jc.2017-02585.

[101] G. S. Mandair and M. D. Morris. "Contributions of Raman spectroscopy to the understanding of bone strength". In: *Bonekey Rep* 4 (2015), p. 620. DOI: 10.1038/bonekey.2014.115.

[102] J. C. Mandell, B. Khurana, and S. E. Smith. "Stress fractures of the foot and ankle, part 1: biomechanics of bone and principles of imaging and treatment". In: *Skeletal Radiol* 46.8 (2017), pp. 1021–1029. DOI: 10.1007/s00256-017-2640-7.

[103] D. Maniglio and W. Bonani. "Method for manufacturing porous scaffolds for biomedical uses and scaffolds thereof". Pat. WO 2016/046715 A1.

[104] D. Maniglio, W. Bonani, G. Bortoluzzi, E. Servoli, A. Motta, and C. Migliaresi. "Electrodeposition of Silk Fibroin on Metal Substrates". In: *Journal of Bioactive and Compatible Polymers* 25.5 (2010), pp. 441–454. DOI: 10.1177/0883911510374384.

[105] D. Maniglio, W. Bonani, C. Migliaresi, and A. Motta. "Silk fibroin porous scaffolds by N2O foaming". In: *J Biomater Sci Polym Ed* 29.5 (2018), pp. 491–506. DOI: 10.1080/09205063.2018.1423811.

[106] M. Martens, R. Van Audekercke, P. Delport, P. De Meester, and J. C. Mulier. "The mechanical characteristics of cancellous bone at the upper femoral region". In: *J Biomech* 16.12 (1983), pp. 971–83. DOI: 10.1016/0021-9290(83)90098-2.

[107] M. G. Martinez, A. J Bullock, S. MacNeil, and I. U Rehman. "Characterisation of structural changes in collagen with Raman spectroscopy". In: *Applied Spectroscopy Reviews* 54.6 (2019), pp. 509–542. DOI: 10.1080/05704928.2018.1506799.

[108] J. Marzi, E. M. Brauchle, K. Schenke-Layland, and M. W. Rolle. "Non-invasive functional molecular phenotyping of human smooth muscle cells utilized in cardiovascular tissue engineering". In: *Acta Biomater* 89 (2019), pp. 193–205. DOI: 10.1016/j.actbio.2019.03.026.

[109] MATLAB. *version 9.5.0.1033004 (R2018b) update 2*. Natick, Massachusetts: The MathWorks Inc., 2018.

[110] P. Matousek and N. Stone. "Recent advances in the development of Raman spectroscopy for deep non-invasive medical diagnosis". In: *J Biophotonics* 6.1 (2013), pp. 7–19. DOI: 10.1002/jbio.201200141.

[111] L. M. McNamara. "Perspective on post-menopausal osteoporosis: establishing an interdisciplinary understanding of the sequence of events from the molecular level to whole bone fractures". In: *J R Soc Interface* 7.44 (2010), pp. 353–72. DOI: 10.1098/rsif.2009.0282.

[112] B. Meder et al. "Influence of the confounding factors age and sex on microRNA profiles from peripheral blood". In: *Clin Chem* 60.9 (2014), pp. 1200–8. DOI: 10.1373/clinchem.2014.224238.

[113] B. D. Metscher. "MicroCT for comparative morphology: simple staining methods allow high-contrast 3D imaging of diverse non-mineralized animal tissues". In: *BMC Physiol* 9 (2009), p. 11. DOI: 10.1186/1472-6793-9-11.

[114] M. J. Mirzaali, J. J. Schwiedrzik, S. Thaiwichai, J. P. Best, J. Michler, P. K. Zysset, and U. Wolfram. "Mechanical properties of cortical bone and their relationships with age, gender, composition and microindentation properties in the elderly". In: *Bone* 93 (2016), pp. 196–211. DOI: 10.1016/j.bone.2015.11.018.

[115] M. Müller et al. “Myoanatomy of the velvet worm leg revealed by laboratory-based nanofocus X-ray source tomography”. In: *Proc Natl Acad Sci U S A* 114.47 (2017), pp. 12378–12383. DOI: 10.1073/pnas.1710742114.

[116] A. Mohammadkhah, L. M. Marquardt, S. E. Sakiyama-Elbert, D. E. Day, and A. B. Harkins. “Fabrication and characterization of poly-(epsilon)-caprolactone and bioactive glass composites for tissue engineering applications”. In: *Mater Sci Eng C Mater Biol Appl* 49 (2015), pp. 632–639. DOI: 10.1016/j.msec.2015.01.060.

[117] M. M. Moisenovich, A. Y. Arkhipova, A. A. Orlova, M. S. Drutskaya, S. V. Volkova, S. E. Zacharov, II Agapov, and M. P. Kirpichnikov. “Composite Scaffolds Containing Silk Fibroin, Gelatin, and Hydroxyapatite for Bone Tissue Regeneration and 3D Cell Culturing”. In: *Acta Naturae* 6.1 (2014), pp. 96–101. DOI: 10.32607/20758251-2014-6-1-96-101.

[118] M. D. Morris and G. S. Mandair. “Raman assessment of bone quality”. In: *Clin Orthop Relat Res* 469.8 (2011), pp. 2160–9. DOI: 10.1007/s11999-010-1692-y.

[119] M. D. Morris, P. Matousek, M. Towrie, A. W. Parker, A. E. Goodship, and E. R. Draper. “Kerr-gated time-resolved Raman spectroscopy of equine cortical bone tissue”. In: *J Biomed Opt* 10.1 (2005), p. 14014. DOI: 10.1117/1.1827605.

[120] A. Motta, D. Maniglio, C. Migliaresi, H. J. Kim, X. Wan, X. Hu, and D. L. Kaplan. “Silk fibroin processing and thrombogenic responses”. In: *J Biomater Sci Polym Ed* 20.13 (2009), pp. 1875–97. DOI: 10.1163/156856208x399936.

[121] W. Murphy, J. Black, and G. Hastings. *Handbook of biomaterial properties*. Springer, 2016.

[122] A. Narayanan, N. Srinaath, M. Rohini, and N. Selvamurugan. “Regulation of Runx2 by MicroRNAs in osteoblast differentiation”. In: *Life Sci* (2019), p. 116676. DOI: 10.1016/j.lfs.2019.116676.

[123] R. Nazarov, H. J. Jin, and D. L. Kaplan. “Porous 3-D scaffolds from regenerated silk fibroin”. In: *Biomacromolecules* 5.3 (2004), pp. 718–26. DOI: 10.1021/bm034327e.

[124] M. C. Nevitt et al. “Risk Factors for a First-Incident Radiographic Vertebral Fracture in Women $\geq$ 65 Years of Age: The Study of Osteoporotic Fractures”. In: *Journal of Bone and Mineral Research* 20.1 (2005), pp. 131–140. DOI: 10.1359/jbmr.041003.

[125] N. D. Nguyen, J. A. Eisman, J. R. Center, and T. V. Nguyen. “Risk Factors for Fracture in Nonosteoporotic Men and Women”. In: *The Journal of Clinical Endocrinology & Metabolism* 92.3 (2007), pp. 955–962. DOI: 10.1210/jc.2006-1476.

[126] Centre for Clinical Practice at Nice. “National Institute for Health and Care Excellence: Clinical Guidelines”. In: *Falls: Assessment and Prevention of Falls in Older People*. London: National Institute for Health and Care Excellence, 2013.

[127] J. S. Nyman, A. J. Makowski, C. A. Patil, T. P. Masui, E. C. O’Quinn, X. Bi, S. A. Guelcher, D. P. Nicollela, and A. Mahadevan-Jansen. “Measuring differences in compositional properties of bone tissue by confocal Raman spectroscopy”. In: *Calcif Tissue Int* 89.2 (2011), pp. 111–22. DOI: 10.1007/s00223-011-9497-x.

[128] S. H. Oh, T. H. Kim, G. I. Im, and J. H. Lee. “Investigation of pore size effect on chondrogenic differentiation of adipose stem cells using a pore size gradient scaffold”. In: *Biomacromolecules* 11.8 (2010), pp. 1948–55. DOI: 10.1021/bm100199m.

[129] C. Olejnik, G. Falgayrac, A. During, M. H. Vieillard, J. M. Maes, B. Cortet, and G. Penel. "Molecular alterations of bone quality in sequesters of bisphosphonates-related osteonecrosis of the jaws". In: *Osteoporos Int* 25.2 (2014), pp. 747–56. DOI: 10.1007/s00198-013-2514-3.

[130] Diagnosis NIH Consensus Development Panel on Osteoporosis Prevention and Therapy. "Osteoporosis Prevention, Diagnosis, and Therapy". In: *JAMA* 285.6 (2001), pp. 785–795. DOI: 10.1001/jama.285.6.785.

[131] N. nath Panda, A. Biswas, K. Pramanik, and S. Jonnalagadda. "Enhanced osteogenic potential of human mesenchymal stem cells on electrospun nanofibrous scaffolds prepared from eri-tasar silk fibroin". In: *J Biomed Mater Res B Appl Biomater* 103.5 (2015), pp. 971–82. DOI: 10.1002/jbm.b.33272.

[132] S. Panzer, M. R. Mc Coy, W. Hitzl, D. Piombino-Mascali, R. Jankauskas, A. R. Zink, and P. Augat. "Checklist and Scoring System for the Assessment of Soft Tissue Preservation in CT Examinations of Human Mummies". In: *PLoS One* 10.8 (2015), e0133364. DOI: 10.1371/journal.pone.0133364.

[133] Y. R. Park, H. W. Ju, J. M. Lee, D. K. Kim, O. J. Lee, B. M. Moon, H. J. Park, J. Y. Jeong, Y. K. Yeon, and C. H. Park. "Three-dimensional electrospun silk-fibroin nanofiber for skin tissue engineering". In: *Int J Biol Macromol* 93.Pt B (2016), pp. 1567–1574. DOI: 10.1016/j.ijbiomac.2016.07.047.

[134] I. H. Parkinson and N. L. Fazzalari. "Characterisation of trabecular bone structure". In: *Skeletal aging and osteoporosis*. Springer, 2013, pp. 31–51.

[135] E. Pauwels, D. Van Loo, P. Cornillie, L. Brabant, and L. Van Hoorebeke. "An exploratory study of contrast agents for soft tissue visualization by means of high resolution X-ray computed tomography imaging". In: *J Microsc* 250.1 (2013), pp. 21–31. DOI: 10.1111/jmi.12013.

[136] H. Perinpanayagam, R. Zaharias, C. Stanford, R. Brand, J. Keller, and G. Schneider. "Early cell adhesion events differ between osteoporotic and non-osteoporotic osteoblasts". In: *J Orthop Res* 19.6 (2001), pp. 993–1000. DOI: 10.1016/s0736-0266(01)00045-6.

[137] R. S. Pillai. "MicroRNA function: multiple mechanisms for a tiny RNA?" In: *Rna* 11.12 (2005), pp. 1753–61. DOI: 10.1261/rna.2248605.

[138] S. MF Pluijm, B. Koes, C. de Laet, N. M. Van Schoor, N. O. Kuchuk, F. Rivadeneira, J. P. Mackenbach, P. Lips, H. A. Pols, and E. W. Steyerberg. "A Simple Risk Score for the Assessment of Absolute Fracture Risk in General Practice Based on Two Longitudinal Studies". In: *Journal of Bone and Mineral Research* 24.5 (2009), pp. 768–774. DOI: 10.1359/jbmr.081244.

[139] P. S. P. Poh, D. W. Hutmacher, B. M. Holzapfel, A. K. Solanki, M. M. Stevens, and M. A. Woodruff. "In vitro and in vivo bone formation potential of surface calcium phosphate-coated polycaprolactone and polycaprolactone/bioactive glass composite scaffolds". In: *Acta Biomater* 30 (2016), pp. 319–333. DOI: 10.1016/j.actbio.2015.11.012.

[140] J. Porthouse, Y.F. Birks, D.J. Torgerson, S. Cockayne, S. Puffer, and I. Watt. "Risk factors for fracture in a UK population: a prospective cohort study". In: *QJM: An International Journal of Medicine* 97.9 (2004), pp. 569–574. DOI: 10.1093/qjmed/hch097.

[141] B. Malafaya PP, A. J. Pedro, A. Peterbauer, C. Gabriel, H. Redl, and R. L. Reis. "Chitosan particles agglomerated scaffolds for cartilage and osteochondral tissue engineering approaches with adipose tissue derived stem cells". In: *J Mater Sci Mater Med* 16.12 (2005), pp. 1077–85. DOI: 10.1007/s10856-005-4709-4.

[142] M. Pudlas, S. Koch, C. Bolwien, S. Thude, N. Jenne, T. Hirth, H. Walles, and K. Schenke-Layland. "Raman spectroscopy: a noninvasive analysis tool for the discrimination of human skin cells". In: *Tissue Engineering Part C: Methods* 17.10 (2011), pp. 1027–1040. DOI: 10.1089/ten.tec.2011.0082.

[143] V. Rabenda, D. Nicolet, C. Beaudart, O. Bruyère, and J. Y. Reginster. "Relationship between use of antidepressants and risk of fractures: a meta-analysis". In: *Osteoporosis International* 24.1 (2013), pp. 121–137. DOI: 10.1007/s00198-012-2015-9.

[144] T. D. Rachner, S. Khosla, and L. C. Hofbauer. "Osteoporosis: now and the future". In: *Lancet* 377.9773 (2011), pp. 1276–87. DOI: 10.1016/s0140-6736(10)62349-5.

[145] M. Rödel, K. Baumann, J. Groll, and U. Gbureck. "Simultaneous structuring and mineralization of silk fibroin scaffolds". In: *J Tissue Eng* 9 (2018), p. 2041731418788509. DOI: 10.1177/2041731418788509.

[146] J. Y. Rho, M. C. Hobatho, and R. B. Ashman. "Relations of mechanical properties to density and CT numbers in human bone". In: *Med Eng Phys* 17.5 (1995), pp. 347–55. DOI: 10.1016/1350-4533(95)97314-F.

[147] D. N. Rockwood, R. C. Preda, T. Yücel, X. Wang, M. L. Lovett, and D. L. Kaplan. "Materials fabrication from Bombyx mori silk fibroin". In: *Nature Protocols* 6 (2011), p. 1612. DOI: 10.1038/nprot.2011.379.

[148] A. Rubinacci, D. Tresoldi, E. Scalco, I. Villa, F. Adorni, G. L. Moro, G. F. Fraschini, and G. Rizzo. "Comparative high-resolution pQCT analysis of femoral neck indicates different bone mass distribution in osteoporosis and osteoarthritis". In: *Osteoporos Int* 23.7 (2012), pp. 1967–75. DOI: 10.1007/s00198-011-1795-7.

[149] N. Sawatjui, T. Damrongrungruang, W. Leeanansaksiri, P. Jearanaikoon, S. Hongeng, and T. Limpaiboon. "Silk fibroin/gelatin-chondroitin sulfate-hyaluronic acid effectively enhances in vitro chondrogenesis of bone marrow mesenchymal stem cells". In: *Mater Sci Eng C Mater Biol Appl* 52 (2015), pp. 90–6. DOI: 10.1016/j.msec.2015.03.043.

[150] M. B. Schaffler and D. B. Burr. "Stiffness of compact bone: effects of porosity and density". In: *J Biomech* 21.1 (1988), pp. 13–6. DOI: 10.1016/0021-9290(88)90186-8.

[151] K. van Schaik, R. Eisenberg, J. Bekvalac, A. Glazer, and F. Ruhli. "Evaluation of lesion burden in a bone-by-bone comparison of osteological and radiological methods of analysis". In: *Int J Paleopathol* 24 (2019), pp. 171–174. DOI: 10.1016/j.ijpp.2018.11.002.

[152] A. M. Schott, D. Hans, F. Duboeuf, P. Dargent-Molina, T. Hajri, G. Bréart, and P. J. Meunier. "Quantitative ultrasound parameters as well as bone mineral density are better predictors of trochanteric than cervical hip fractures in elderly women. Results from the EPIDOS study". In: *Bone* 37.6 (2005), pp. 858–863. DOI: 10.1016/j.bone.2005.06.024.

[153] P. Schwarz, N. R. Jorgensen, L. Mosekilde, and P. Vestergaard. "The evidence for efficacy of osteoporosis treatment in men with primary osteoporosis: a systematic review and meta-analysis of antiresorptive and anabolic treatment in men". In: *J Osteoporos* 2011 (2011), p. 259818. DOI: 10.4061/2011/259818.

[154] C. Seeliger, E. R. Balmayor, and M. van Griensven. "miRNAs Related to Skeletal Diseases". In: *Stem Cells Dev* 25.17 (2016), pp. 1261–81. DOI: 10.1089/scd.2016.0133.

[155] C. Seeliger, K. Karpinski, A. T. Haug, H. Vester, A. Schmitt, J. S. Bauer, and M. van Griensven. "Five freely circulating miRNAs and bone tissue miRNAs are associated with osteoporotic fractures". In: *J Bone Miner Res* 29.8 (2014), pp. 1718–28. DOI: 10.1002/jbmr.2175.

[156] E. Servoli, D. Maniglio, A. Motta, R. Predazzer, and C. Migliaresi. "Surface properties of silk fibroin films and their interaction with fibroblasts". In: *Macromol Biosci* 5.12 (2005), pp. 1175–83. DOI: 10.1002/mabi.200500137.

[157] W. Shi et al. "Structurally and Functionally Optimized Silk-Fibroin-Gelatin Scaffold Using 3D Printing to Repair Cartilage Injury In Vitro and In Vivo". In: *Adv Mater* 29.29 (2017). DOI: 10.1002/adma.201701089.

[158] M. J Silva. *Skeletal Aging and Osteoporosis*. Springer, 2013.

[159] M. Hasan Sohel. "Extracellular/circulating microRNAs: release mechanisms, functions and challenges". In: *Achievements in the Life Sciences* 10.2 (2016), pp. 175–186. DOI: 10.1016/j.als.2016.11.007.

[160] M. Solmi, N. Veronese, C. U. Correll, A. Favaro, P. Santonastaso, L. Caregaro, D. Vancampfort, C. Luchini, M. De Hert, and B. Stubbs. "Bone mineral density, osteoporosis, and fractures among people with eating disorders: a systematic review and meta-analysis". In: *Acta Psychiatrica Scandinavica* 133.5 (2016), pp. 341–351. DOI: 10.1111/acps.12556.

[161] E. Silva J. Martins de Souza, J. Utsch, M. A. Kimm, S. Allner, M. F. Epple, K. Achterhold, and F. Pfeiffer. "Dual-energy micro-CT for quantifying the time-course and staining characteristics of ex-vivo animal organs treated with iodine- and gadolinium-based contrast agents". In: *Sci Rep* 7.1 (2017), p. 17387. DOI: 10.1038/s41598-017-17064-z.

[162] T. P. van Staa, T. P. van Staa, T. P. van Staa, H. G. M. Leufkens, and C. Cooper. "Does a Fracture at One Site Predict Later Fractures at Other Sites? A British Cohort Study". In: *Osteoporosis International* 13.8 (2002), pp. 624–629. DOI: 10.1007/s001980200084.

[163] K. L. Stone, D. G. Seeley, L. Lui, J. A. Cauley, K. Ensrud, W. S. Browner, M. C. Nevitt, and S. R. Cummings. "BMD at Multiple Sites and Risk of Fracture of Multiple Types: Long-Term Results From the Study of Osteoporotic Fractures". In: *Journal of Bone and Mineral Research* 18.11 (2003), pp. 1947–1954. DOI: 10.1359/jbmr.2003.18.11.1947.

[164] B. Stubbs, F. Gaughran, A. J. Mitchell, M. De Hert, R. Farmer, A. Soundy, S. Rosenbaum, and D. Vancampfort. "Schizophrenia and the risk of fractures: a systematic review and comparative meta-analysis". In: *General Hospital Psychiatry* 37.2 (2015), pp. 126–133. DOI: 10.1016/j.genhosppsych.2015.01.004.

[165] L. W. Sun, C. Wang, F. Pu, Y. Li de, H. J. Niu, and Y. B. Fan. "Comparative study on measured variables and sensitivity to bone microstructural changes induced by weightlessness between in vivo and ex vivo micro-CT scans". In: *Calcif Tissue Int* 88.1 (2011), pp. 48–53. DOI: 10.1007/s00223-010-9422-8.

[166] S. S. Sun, H. L. Ma, C. L. Liu, C. H. Huang, C. K. Cheng, and H. W. Wei. "Difference in femoral head and neck material properties between osteoarthritis and osteoporosis". In: *Clin Biomech (Bristol, Avon)* 23 Suppl 1 (2008), pp. 39–47. DOI: 10.1016/j.clinbiomech.2007.11.018.

[167] B. C. Taylor, P. J. Schreiner, K. L. Stone, H. A. Fink, S. R. Cummings, M. C. Nevitt, P. J. Bowman, and K. E. Ensrud. "Long-Term Prediction of Incident Hip Fracture Risk in Elderly White Women: Study of Osteoporotic Fractures". In: *Journal of the American Geriatrics Society* 52.9 (2004), pp. 1479–1486. DOI: 10.1111/j.1532-5415.2004.52410.x.

[168] K. M. Torsney, A. J. Noyce, K. M. Doherty, J. P. Bestwick, R. Dobson, and A. J. Lees. "Bone health in Parkinson's disease: a systematic review and meta-analysis". In: *Journal of Neurology, Neurosurgery & Psychiatry* 85.10 (2014), pp. 1159–1166. DOI: 10.1136/jnnp-2013-307307.

[169] A. S. Turner. "Animal models of osteoporosis–necessity and limitations". In: *Eur Cell Mater* 1 (2001), pp. 66–81.

[170] C. H. Turner and D. B. Burr. "Basic biomechanical measurements of bone: a tutorial". In: *Bone* 14.4 (1993), pp. 595–608.

[171] R. T. Turner, A. Maran, S. Lotinun, T. Hefferan, G. L. Evans, M. Zhang, and J. D. Sibonga. "Animal models for osteoporosis". In: *Rev Endocr Metab Disord* 2.1 (2001), pp. 117–27.

[172] D. Ulrich, B. Van Rietbergen, A. Laib, and P. Ruegsegger. "The ability of three-dimensional structural indices to reflect mechanical aspects of trabecular bone". In: *Bone* 25.1 (1999), pp. 55–60.

[173] M. A Valencia-Sanchez, J. Liu, G. J. Hannon, and R. Parker. "Control of translation and mRNA degradation by miRNAs and siRNAs". In: *Genes and development* 20.5 (2006), pp. 515–524.

[174] A. Varkey, E. Venugopal, P. Sugumaran, G. Janarthanan, M. M. Pillai, S. Rajendran, and A. Bhattacharyya. "Impact of silk fibroin-based scaffold structures on human osteoblast MG63 cell attachment and proliferation". In: *Int J Nanomedicine* 10 Suppl 1 (2015), pp. 43–51. DOI: 10.2147/ijn.s82209.

[175] J. R. Vetsch, R. Muller, and S. Hofmann. "The influence of curvature on three-dimensional mineralized matrix formation under static and perfused conditions: an in vitro bioreactor model". In: *J R Soc Interface* 13.123 (2016). DOI: 10.1098/rsif.2016.0425.

[176] P. Wang, F. Perche, D. Logeart-Avramoglou, and C. Pichon. "RNA-based Therapy for Osteogenesis". In: *Int J Pharm* (2019), p. 118594. DOI: 10.1016/j.ijpharm.2019.118594.

[177] Z. Wang et al. "Electrospun silk fibroin/poly(lactide-co-epsilon-caprolactone) nanofibrous scaffolds for bone regeneration". In: *Int J Nanomedicine* 11 (2016), pp. 1483–500. DOI: 10.2147/ijn.s97445.

[178] WHO Scientific Group on Prevention and Management of Osteoporosis and World Health Organization. *Prevention and management of osteoporosis: report of a WHO scientific group*. World Health Organization, 2003.

[179] D. R. Williams, H. C. Watt, and A. J. Lees. "Predictors of falls and fractures in bradykinetic rigid syndromes: a retrospective study". In: *Journal of Neurology, Neurosurgery & Psychiatry* 77.4 (2006), pp. 468–473. DOI: 10.1136/jnnp.2005.074070.

[180] A. J. Wirth, R. Muller, and G. H. van Lenthe. "Computational analyses of small endosseous implants in osteoporotic bone". In: *Eur Cell Mater* 20 (2010), pp. 58–71. DOI: DOI:10.22203/eCM.v020a06.

[181] World Health Organization. *Guidelines for preclinical evaluation and clinical trials in osteoporosis*. World Health Organization, 1998.

[182] Q. Wu, A. F. Bencaz, J. G. Hentz, and M. D. Crowell. "Selective serotonin reuptake inhibitor treatment and risk of fractures: a meta-analysis of cohort and case–control studies". In: *Osteoporosis International* 23.1 (2012), pp. 365–375. DOI: 10.1007/s00198-011-1778-8.

[183] L. Y. Yang, M. Yaseen, X. B. Zhao, P. Coffey, F. Pan, Y. M. Wang, H. Xu, J. Webster, and J. R. Lu. "Gelatin modified ultrathin silk fibroin films for enhanced proliferation of cells". In: *Biomedical Materials* 10.2 (2015). DOI: Artn02500310.1088/1748-6041/10/2/025003.

[184] D. Yao, H. Liu, and Y. Fan. "Silk scaffolds for musculoskeletal tissue engineering". In: *Exp Biol Med (Maywood)* 241.3 (2016), pp. 238–45. DOI: 10.1177/1535370215606994.

[185] Z. C. Yuan, H. Mo, J. Guan, J. L. He, and Z. J. Wu. "Risk of hip fracture following stroke, a meta-analysis of 13 cohort studies". In: *Osteoporosis International* 27.9 (2016), pp. 2673–2679. DOI: 10.1007/s00198-016-3603-x.